Light Sources in Semiconductor Photonic Materials

LIGHT SOURCES IN SEMICONDUCTOR PHOTONIC MATERIALS

LICHT-BRONNEN IN FOTONISCHE HALFGELEIDER MATERIALEN

(met een samenvatting in het Nederlands)

PROEFSCHRIFT

ter verkrijging van de graad van doctor aan de Universiteit Utrecht op gezag van de rector magnificus, prof. dr. W. H. Gispen, ingevolge het besluit van het College voor Promoties in het openbaar te verdedigen op woensdag 7 juni 2006 des middags te 14.30 uur

door

ARIE FLORIS VAN DRIEL

geboren op 28 februari 1978, te Werkendam

Universiteit Utrecht

Promotores: Prof. dr. D. Vanmaekelbergh
Prof. dr. J. J. Kelly

Debye Instituut
Universiteit Utrecht

Prof. dr. W. L. Vos

MESA$^+$ Instituut
Universiteit Twente

FOM Instituut voor Atoom- en Molecuulfysica (AMOLF)
Amsterdam

This research has been financially supported by the Council of Chemical Sciences (CW) of the Netherlands Organisation for Scientific Research (NWO) and was done in the group Condensed Matter and Interfaces (CMI) at Utrecht University. Part of the research was done in the group Complex Photonic Systems (COPS) at the MESA$^+$ Institute at the University of Twente.

CIP-GEGEVENS KONINKLIJKE BIBLIOTHEEK, DEN HAAG

van Driel, Arie Floris

Lichtbronnen in fotonische halfgeleider materialen
(Onderzoek aan lichtbronnen in fotonische halfgeleider materialen) /
Arie Floris van Driel. - Utrecht: Universiteit Utrecht,
Faculteit Bètawetenschappen, Departement Scheikunde, Debye Instituut.
Proefschrift Universiteit Utrecht. Met samenvatting in het Nederlands.
ISBN-10: 90-393-4250-4 ISBN-13: 978-90-393-4250-3

Contents

Chapter 1

Introduction

"So scientific explanation is not (pure) science but an application of science. It is a use of science to satisfy certain of our desires; and these desires are specific in a specific context, but they are always desires for descriptive information....And while it is true that we seek for explanation, the value of this search for science is that the search for explanation is *ipso facto* a search for empirically adequate, empirically strong theories."

Bas C. van Fraassen, *The Scientific Image*, 1980 [1]

1.1 Introduction

Spontaneous emission of light or luminescence is a fundamental process that plays an essential role in many phenomena in nature and forms the basis of many applications. The term luminescence describes the conversion of energy into visible light. Luminescence plays an essential role in everyday appliances such as fluorescent tubes, television screens, plasma display panels, lasers and light emitting diodes [2]. Control over the emission of light is therefore extremely important. For example, if spontaneous emission would be completely suppressed, laser action could be generated without a threshold [3, 4]. Solar cells form an important alternative to replace fossil fuels. More control over the transport and emission of light should enhance the efficiency of solar cells [5, 6]. An increase of the energy efficiency of fluorescent tubes can be achieved with quantum-cutting [7]. In quantum-cutting materials one photon with a high energy is absorbed and two photons with lower energy are emitted. The wide variety of applications and the fundamental scientific interest are the main reasons for the search for control over the emission of light.

Bulk semiconductors, semiconductor quantum-wells, organic dye molecules, transition-metal ions and rare-earth ions are used as luminescent sources. Semiconductor nanocrystals, also called quantum dots, form a relatively new and exciting class of luminescent materials. The optical properties of nanocrystals are determined by the crystals' size; this is called the 'quantum size effect'. For example, small nanocrystals emit light with a shorter wavelength than larger crystals. Emission from nanocrystals can be generated after optical or electrical excitation of an electron-hole pair and it is called spontaneous emission when the electron-hole pair recombines radiatively without being triggered by external radiation. The rate of radiative recombination is determined by both the internal electronic structure of the nanocrystal and by its environment, i.e., the density of electromagnetic modes (DOS) of the field. It has been predicted theoretically [4] that a 'photonic' material environment can control the rate of radiative recombination of an embedded light source via modification of the DOS. In this thesis experiments concerning the control of spontaneous emission from nanocrystals by photonic materials are described.

In a photonic material the refractive index varies on a length-scale com-

parable to the wavelength of light [8]. Macroporous photonic materials consist of a high refractive index phase containing air-filled pores with a diameter larger than 50 nm [9]. As a consequence of the spatial variation of the refractive index, the propagation of visible or near-infrared light is modified with respect to that in homogeneous dielectric materials. Two different forms of propagation can be distinguished: light propagation can be diffusive in random porous materials and, alternatively, Bragg diffraction can occur in a so-called photonic crystal. A main research goal is the achievement of a complete photonic bandgap: a range of frequencies in which no electromagnetic modes exist and all propagation directions are forbidden. At the frequencies of the photonic bandgap, spontaneous emission of light is completely inhibited [3, 4]. In random porous materials the propagation direction of light is randomised and the waves undergo a random walk. When certain specific material requirements are fulfilled, both random and crystalline materials could localise light [10]. Localisation of light and the fabrication of a material with a complete photonic bandgap are huge scientific challenges. For this reason photonic materials are being extensively studied.

In this thesis experiments on light emission in crystalline and random macroporous photonic materials are reported. In the first part of the Introduction spontaneous emission and its relation to photonic crystals will be discussed. The second part is devoted to random porous photonic materials. In the last part an outline of this thesis will be presented.

1.2 Spontaneous emission: Fermi's 'golden rule'

When light sources, such as atoms, molecules or nanocrystals, are in the excited state, they can undergo a transition to the ground state leading to the emission of light. In this case one speaks of spontaneous emission [11, 12]. Spontaneous emission occurs independently of external radiation; the transition is caused by interaction between the light source and the vacuum field. This occurs in all appliances in which light is involved, except for lasers. In contrast, laser light is generated when emission is stimulated by radiation; this is called 'stimulated emission'. Control of the rate of spontaneous emission is an important research goal and for this reason photonic

materials are being extensively studied.

Spontaneous emission can be described by Fermi's golden rule. An extensive derivation of Fermi's golden rule for spontaneous emission can be found in Refs. [11, 12]. The rate of emission depends on two factors: an 'atomic part', which describes the internal structure of the light source and a 'field part', which describes the density of electromagnetic modes of the environment. The atomic part describes the strength of a transition between two states in terms of transition moments. In the case of a dipole-allowed transition between the initial and final states ψ_i and ψ_f, the transition dipole moment μ_{if}[1], with units Cm, is given by

$$\mu_{if} = -e \int_V \psi_i \mathbf{r} \psi_f^* dV \tag{1.2}$$

where $\mathbf{r}$ is the dipole moment operator, V the volume and e the electron charge. It is assumed here that the the levels corresponding to ψ_i and ψ_f are very sharply defined in energy; hence, the transition is assumed to be sharp. However, real transitions have a finite width which can be described by a lineshape function [11]:

$$\int g(\omega) d\omega = 1 \tag{1.3}$$

where $g(\omega)$ is the homogeneous lineshape of the transition and ω the frequency of emission.

The second factor which determines the rate of spontaneous emission is the field part. It is this part which allows one to control the rate of spontaneous emission via the density of electromagnetic modes. The density of the electromagnetic modes of the field can be obtained by counting the number of wave vectors in reciprocal space at a particular frequency, using the dispersion relation of light. For each wave vector there are two polarisation modes, i.e., two directions of the E-vector. For one polarisation in a

[1]The oscillator strength is frequently used to express the strength of an optical transition and is defined as follows [11]:

$$f = \frac{2m\omega_{if}}{3\hbar e^2} |\mu_{if}|^2 \tag{1.1}$$

where m is the electron mass, $\hbar$ Planck's constant, ω_{if} the frequency of the transition and μ_{if} the transition dipole moment. In a classical damped oscillator model f=1 [11]. In real situations, f can be very small. The oscillator strength is directly proportional to the absorption strength.

homogeneous dielectric the density of electromagnetic states $\rho(V,\omega)$, with units $m^{-3}s$, is given by

$$\rho(V,\omega) = \frac{\omega^2 n^3}{2\pi^2 c^3} \tag{1.4}$$

where n is the refractive index and c the speed of light. To determine the rate of spontaneous emission, the overlap between the density of electromagnetic modes and the lineshape function must be calculated:

$$\Gamma_{sp,ED} = \frac{4\pi}{3\hbar^2}|\mu_{if}|^2|\mathbf{E}|^2 \int_0^\infty \rho(\omega)g(\omega)d\omega \tag{1.5}$$

where $\Gamma_{sp,ED}$ is the rate of the electric dipole allowed transition, $\rho(\omega)$ is the number of electromagnetic modes per unit frequency ($= \frac{\omega^2 n^3 V}{2\pi^2 c^3}$) and $|\mathbf{E}|^2$ is the squared amplitude of the electric field and is directly related to electric energy density of the field[2]. It is assumed here that the dipoles are randomly oriented. When the transition is sharp, i.e., $g(\omega)$ is a Dirac delta function $\delta(\omega - \omega_{if})$, with ω_{if} the frequency of the transition, eq. 1.5 becomes:

$$\Gamma_{sp,ED} = \frac{4\pi}{3\hbar^2}|\mu_{if}|^2|\mathbf{E}|^2 \int \rho(\omega)\delta(\omega - \omega_{if})d\omega \tag{1.8}$$

$$= \frac{4\pi}{3\hbar^2}|\mu_{if}|^2|\mathbf{E}|^2\rho(\omega_{if}) \tag{1.9}$$

After substitution of eqs. 1.4 and 1.7 the rate becomes:

$$\Gamma_{sp,ED}(\omega) = \frac{\omega_{if}^3 n|\mu_{if}|^2}{6\pi\varepsilon_0\hbar c^3} \tag{1.10}$$

The wave function of a two-level emitter in the presence of a perturbing field is given by $\Psi = c_i(t)\psi_i + c_f(t)\psi_f$. The rate ($\Gamma_{sp}$ in eq. 1.5) is equal to

[2]The total energy density $\rho_E(V,\omega)$ of the field at a frequency ω is given by

$$\rho_E(V,\omega) = \frac{\hbar\omega N(\omega)}{V} \tag{1.6}$$

where $N(\omega)$ is the number of photons of frequency ω within a volume V. $\rho_E(V,\omega)$ and $|\mathbf{E}|^2$ are related: $\rho_E(V,\omega) = 2\varepsilon\varepsilon_0|\mathbf{E}|^2$, where ε is the dielectric constant and ϵ_0 the permittivity of free space. In the ground state of the field each mode contains $\frac{1}{2}\hbar\omega$ of energy and therefore:

$$|\mathbf{E}|^2 = \frac{\rho_E(V,\omega)}{4\varepsilon\varepsilon_0} = \frac{\hbar\omega}{4\varepsilon\varepsilon_0 V}. \tag{1.7}$$

the rate of decrease of coefficient c_f:

$$c_f(t) = c_f(0)\exp(-\Gamma_{sp}t) \tag{1.11}$$

and the probability of finding a two-level system in the excited state is equal to the square of the coefficient c_f

$$c_f^2(t) = c_f^2(0)\exp(-2\Gamma_{sp}t) = c_f^2(0)\exp(-\Gamma_{rad}t) \tag{1.12}$$

Therefore, the radiative decay rate, which can be determined experimentally, is given by:

$$\Gamma_{rad,ED}(\omega) = 2\Gamma_{sp,ED} = \frac{\omega^3 n|\mu_{if}|^2}{3\pi\varepsilon_0\hbar c^3} \tag{1.13}$$

It should be noted that corrections due to the local field and degeneracy of the levels are not taken into account here. Eq. 1.13 is equal to the Einstein A coefficient [12] and is valid all homogeneous dielectrics, including free space.

1.3 Photonic crystals

In free space the DOS scales with ω^2 (eq. 1.4). In a photonic crystal the DOS is modified with respect to that of free space; the states are redistributed and these materials can therefore modify the rate of spontaneous emission. Due to Bragg diffraction, certain electromagnetic modes are excluded and, as a consequence, 'stop gaps' open. When all propagation modes are excluded in a frequency range, a bandgap opens. At the frequencies of the bandgap the DOS is zero. According to eq. 1.5 the rate of spontaneous emission scales with the DOS. Therefore, spontaneous emission at a frequency corresponding to the bandgap is expected to be completely inhibited [3, 4]. Several authors claimed a material with a complete photonic bandgap [13–15]. However, no definite proof of a complete photonic bandgap in these materials was presented. Photonic crystals which strongly interact with light are, however, known. An inverse opal, which combines an face-centered cubic (fcc) structure of air-spheres with a high refractive index material in the voids between the spheres, is an example

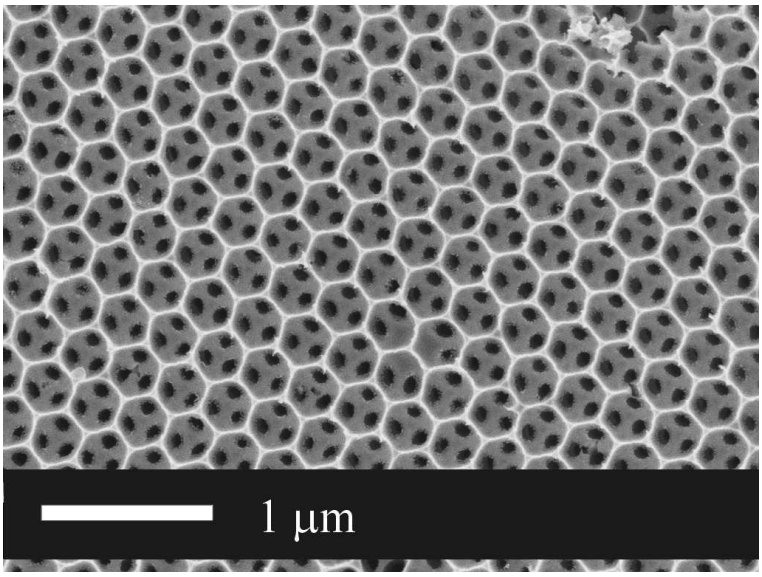

Figure 1.1: *Scanning electron microscopy image of the (111) face of a titania inverse opal photonic crystal with a lattice parameter a=327 ± 7 nm. The black spots are the connections between air-spheres in the layer lying one plane beneath the surface. Image courtesy of L. A. Woldering.*

of such a strongly interacting photonic crystal. In figure 1.1 an electron microscopy image of a (111) face of a titania (TiO_2) inverse opal is shown. In titania inverse opals the DOS is reduced and enhanced in certain frequency ranges, but not completely suppressed. In figure 1.2 the DOS averaged over the unit-cell of a titania inverse opal is plotted as a function of the reduced frequency $\widetilde{\omega} = \omega a/2\pi c = a/\lambda$. The DOS of a homogenous medium with a refractive index n=1.3 is also shown. Clearly, the DOS in the photonic crystal is modified with respect to that in free space. At around $\widetilde{\omega} = 0.7$ the DOS is reduced. The region is called 'pseudo gap' and coincides with the frequency at which first-order Bragg diffraction occurs. At this wavelength no bandgap is expected, irrespective of the refractive index of the backbone material [16–18]. At $\widetilde{\omega} \sim 1.2$ a large increase and a decrease of DOS can be observed. This region corresponds to the second-order stop gap. A complete bandgap is expected in this range if the refractive index of the backbone material is high enough [17–19]. This does not occur for titania inverse opals. In spite of the absence of a complete photonic bandgap we use titania inverse opals in our experiments. Titania inverse opals can be

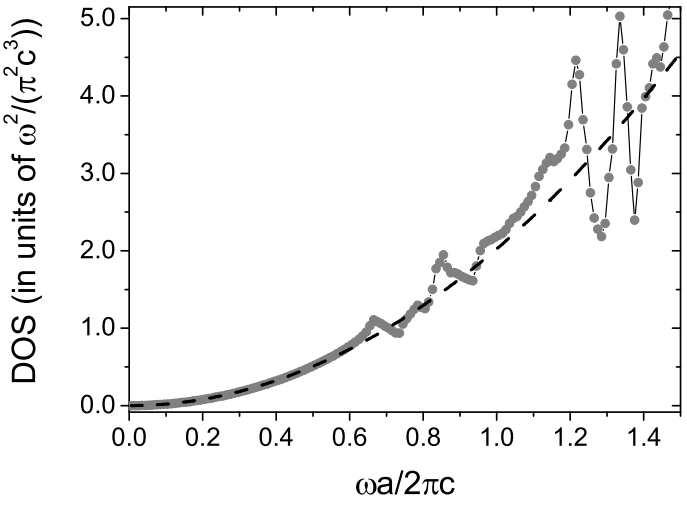

Figure 1.2: *Density of states (DOS, grey dots) for a titania inverse opal photonic crystal versus reduced frequency $\widetilde{\omega} = \omega a/2\pi c = a/\lambda$, where ω is the frequency, c the speed of light, a the lattice parameter of the photonic crystal and λ the wavelength. For the calculation a volume fraction of titania of 11 % and a refractive index of 2.55 were assumed. In the weak photonic range the DOS scales with ω^2. The DOS of a homogenous medium with a refractive index n=1.3 is also shown (dashed curve, eq. 1.4). DOS calculations were performed by A. F. Koenderink [19].*

made with high quality [20], have been thoroughly characterised and have a wide transparency range. As a consequence of the strong modification of the DOS as shown in figure 1.2, a strong effect on the lifetime of embedded light sources is expected.

1.4 Light sources

It is clear that photonic crystals can control the radiative decay rate via the DOS at the location of an embedded emitter, i.e., the field part in eq. 1.5. However, there is no experimental evidence for this. In the ideal experiment a two-level emitter, i.e., the light source, is placed inside the photonic crystal and the rate of spontaneous emission is measured with a time-resolved measurement and referenced with respect to the rate in free space. Continuous-wave measurements with light sources with a low lumines-

cence efficiency have shown a clear modification of the DOS in photonic crystals [21, 22]. Time-resolved measurements on embedded light sources have been performed by several groups [23–30] but no convincing lifetime effect has been reported. In order to observe effects of the photonic crystal environment on the radiative rate, several essential requirements on the light source must be fulfilled. It will be shown below that these requirements are met by semiconductor nanocrystals. Therefore, in many of the experiments described in this thesis nanocrystals are used as light sources.

Excited states can be de-populated via two types of processes: non-radiative and radiative relaxation. The rate of radiative relaxation, i.e., spontaneous emission, is proportional to the DOS (eq. 1.5) and can therefore be modified by a photonic crystal. The rate of non-radiative relaxation usually cannot be controlled by a photonic crystal. In lifetime experiments the total decay rate, the sum of radiative and non-radiative rates $\Gamma_{rad} + \Gamma_{nrad}$, is measured. Therefore, to observe an effect of the photonic crystal environment on the total decay rate of the emitter, the fraction $\frac{\Gamma_{rad}}{\Gamma_{nrad}}$ must be high enough. This is one of the reasons why the observation of lifetime effects with dye molecules has proved troublesome; the quantum yield of these light sources in a semiconductor photonic crystal is reduced due to interaction with the backbone material [31].

Modification of the DOS is expected in that frequency range in which the lattice parameter of the photonic crystal and the wavelength of light are comparable, $a/\lambda \approx 1$ in figure 1.2. Therefore, lifetime effects can only be observed if the emission frequency of the light source coincides with that frequency range. Several dyes, with various emission frequencies and a high quantum efficiency, are commercially available [32]. The emission frequency of nanocrystals can be easily tuned via the size [33, 34]. For example, decreasing the diameter of spherical CdSe nanocrystals from 7 to 2.3 nm shifts the emission wavelength from 650 nm to 460 nm [35, 36]. Besides tuning of the emission frequency, the lattice parameter of the photonic crystal can be tuned to the emission frequency. In studies with embedded light sources, photonic crystals with a small lattice parameter form ideal reference materials; the emission frequency of the light source is in the low frequency limit of the photonic crystal [37]: $\widetilde{\omega} \ll 1$, see figure 1.2. In the low frequency limit the DOS in the photonic crystal is proportional to ω^2, as in

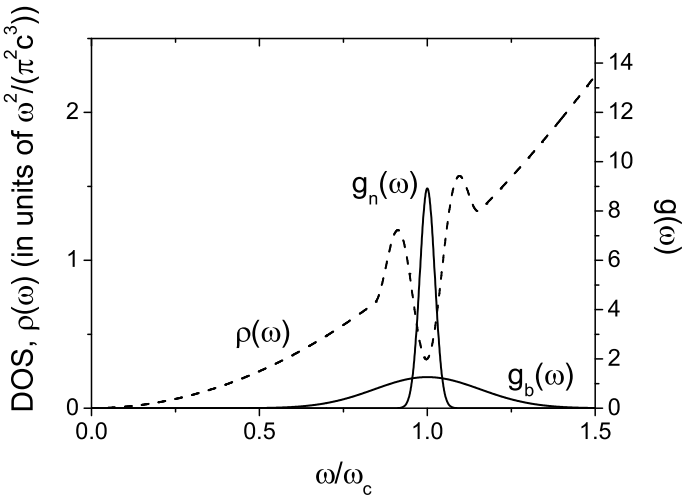

Figure 1.3: *Density of states (DOS, $\rho(\omega)$, dashed curve) and spectra of light sources with narrow ($g_n(\omega)$) and broad ($g_b(\omega)$) homogeneous linewidths versus the frequency ω. The DOS is modified with respect to the DOS of free space around the central frequency ω_c. The radiative decay rate of the light source with the broad linewidth is inhibited by only a factor of 1.02 while the radiative rate of the light source with the narrow linewidth is inhibited by a factor of 2.11.*

homogeneous non-photonic media, and the crystal is chemically identical to the tuned crystal.

According to eq. 1.5 the rate of spontaneous emission is determined by the spectral overlap between the lineshape function of the light source $g(\omega)$ and the density of electromagnetic modes $\rho(\omega)$. The observed lifetime effect is therefore the result of an integration over the emission frequency-range of the light source [38, 39]. In photonic crystals the electromagnetic states are re-distributed with respect to those of a homogeneous dielectric; in small frequency windows the DOS may be modified, but over a broad frequency range the total DOS must be conserved. Therefore, the homogeneous linewidth of the light source must be comparable to or smaller than the frequency window over which the DOS is modified (see figure 1.3).

Dye molecules usually have a broad homogeneous linewidth, much broader than the bandwidth of the pseudo-gap in inverse opals. For this reason, dye molecules are ideal probes to study the spectral re-distribution

of the emission due to the photonic crystal environment [40, 41]. The spectra can be referenced easily because the long-wavelength limit is unaffected by the photonic crystal. However, due to the broad homogenous linewidth the expected effect of photonic crystals on the lifetime of the dye emission is small [38–40] and for this reason dye molecules are not suitable to probe DOS effects via lifetime measurements [31, 40].

Atomic emitters usually have sharp transitions and are thus well-suited to probe DOS modifications in photonic crystals. For example, erbium ions (Er^{3+}) can be implanted in silicon. Er^{3+} ions have an emission peak at around 1540 nm. The emission peak is much narrower than the bandwidth of the photonic bandgap in silicon inverted opals and emission at 1540 nm is not absorbed by silicon. Because of these reasons, Er^{3+} ions are ideal light sources to probe DOS effects in silicon based photonic structures [42].

The low-temperature homogeneous linewidth of nanocrystals is very narrow, FWHM$<$0.15 meV [43, 44]. This is one of the reasons why nanocrystals are called atom-like light sources. For 0.6 nm indium arsenide (InAs) nanocrystals grown by molecular beam epitaxy (MBE) the homogenous linewidth is independent of temperature up to 50 K [43]. The absence of thermal broadening confirms the zero-dimensional δ-function electronic density of states of nm sized nanocrystals. The temperature dependence of the homogeneous emission linewidth was studied by several groups [45–48]. For colloidal CdSe nanocrystals the δ-function electronic density of states is an oversimplified picture. As a consequence of several dephasing mechanisms such as scattering at defects, phonon scattering and carrier-carrier scattering, the homogeneous linewidth and its temperature-dependence are much more complex [46]. A temperature increase of the linewidth is generally observed, but the reported absolute values vary from 32 μeV [48] to 10 meV [45] for CdSe at 10 K. However, from Refs. [49–51] it is clear that the linewidth at room temperature is considerably smaller than the linewidth of the ensemble; $\sim$ 50 meV for single nanocrystals and $\sim$ 150 meV for the ensemble. The linewidth is therefore small enough to observe modification of the DOS in photonic crystals.

The three above-mentioned requirements, i.e., a high quantum efficiency, a tunable emission frequency and a small homogeneous linewidth, are fulfilled by semiconductor nanocrystals. For these reasons nanocrystals are

ideal light sources to probe DOS effects in photonic materials.

1.5 Optical properties of nanocrystal suspensions

Nanocrystalline semiconductor colloids, also called quantum dots, belong to a state of matter that is intermediate between molecules and solids. Their size-dependent physical and chemical properties are currently being investigated in various fields of science. CdSe and CdTe nanocrystal suspensions with a high photoluminescence quantum efficiency in the visible range of the spectrum can be prepared via wet-chemical routes [52]. The synthesis is based on the pyrolysis of organometallic reagents after injection into a hot coordinating solvent. Optical properties of nanocrystals with dimensions smaller than the Bohr-radius of the exciton, which is defined as the average distance between the electron and hole [53], differ strongly from those of bulk crystals. The Bohr radius is 4.9 nm for CdSe [53] and 7.5 nm for CdTe [54]. In figure 1.4 (a) absorption and emission spectra of a colloidal CdSe suspension, with an average particle diameter of 4.5 nm and a photoluminescence quantum efficiency of 50%, are shown.

When the crystals' size is smaller than the exciton Bohr radius, the exciton becomes confined into a smaller volume. Due to confinement, nanocrystals possess discrete electron and hole energy levels [33, 55, 56], and the energy of the exciton increases. This is schematically shown in figure 1.4 (b). The separation between the filled and unfilled levels (ΔE_{nc}) increases with respect to the value for a bulk crystal of the same material (ΔE_{bulk}) and is determined by the nanocrystals' size: in smaller nanocrystals the separation is larger. Furthermore, decreasing the size of the crystal induces a gradual change from continuous bands in the bulk crystal to discrete electron and hole levels in the nanocrystal. The gradual change starts at the band edges, as schematically shown in figure 1.4 (b). The increase of the separation between the filled and unfilled levels can clearly be observed in figure 1.4 (a): the absorption and emission energies are blue-shifted with respect to the bulk. In spite of the discrete electron and hole levels in the nanocrystals, the absorption and emission spectra are broad. This is related to the size dispersion of the nanocrystal suspension. A suspension of nanocrystals contains a collection of differently sized particles, distributed

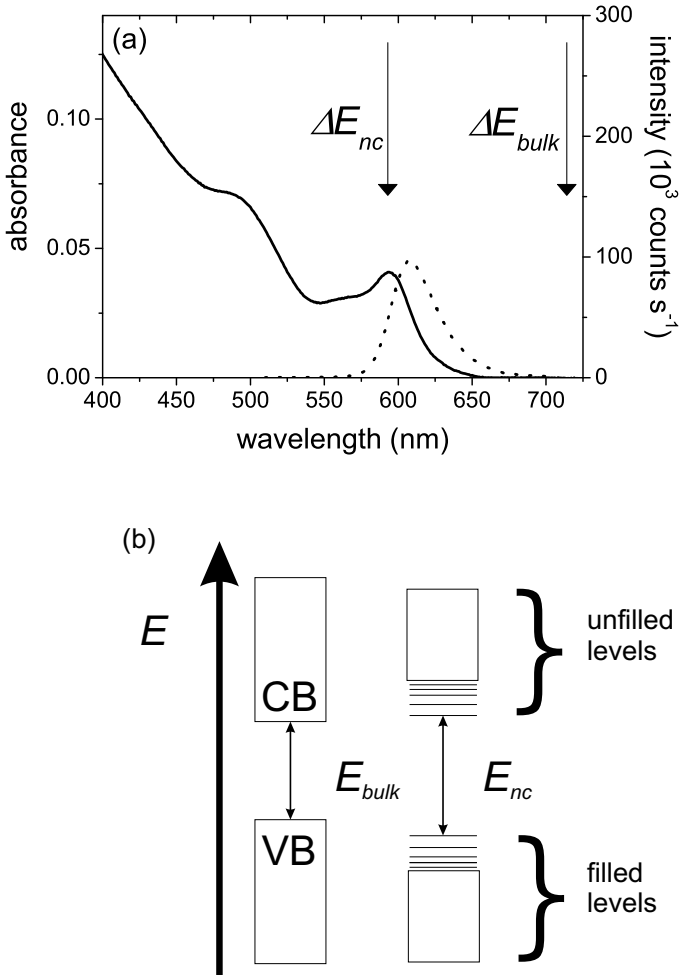

Figure 1.4: *(a) Absorption (solid line, left axis) and emission (dotted line, right axis) spectra of CdSe nanocrystals in chloroform. The nanocrystals have an average size of 4.5 nm and a photoluminescence quantum efficiency of* 50%*. In the absorption spectrum several transitions can be distinguished. Emission only occurs from the lowest-energy exciton. (b) Schematic band structure of a bulk semiconductor crystal (left) and a nanocrystal (right). In the bulk crystal the conduction band (CB) and the valence band (VB) are separated by the bandgap* ΔE_{bulk}*. In the nanocrystal there are discrete energy levels at the band edges, and the filled and unfilled levels are separated by* ΔE_{nc} *which is larger than* ΔE_{bulk}*.*

around a certain average size. Each individual nanocrystal absorbs and emits light in a narrow frequency window, leading to broad spectra for the suspension [49, 51]. Despite the size dispersion of the suspension, several transitions in the absorption spectrum can be distinguished. The position and the strength of the transitions have been studied as a function of particle size and assigned using a system of quantum numbers which take into account the complex valence band structure [57].

Since its publication in 1993 the organometallic synthesis route [52] has been adapted for many types of semiconductor nanocrystals (for an overview, see Ref. [58]). After years of modification and improvement CdSe and CdTe suspensions can be prepared with a high photoluminescence efficiency ($\leq$80 %), a high degree of monodispersity ($\geq$ 5%) and with a good control of the size and shape of the nanocrystals. An important step forward in improvement of the optical properties was made by capping the nanocrystals, besides the organic coating, with an inorganic semiconductor with a larger bandgap [35]. Capping with an inorganic semiconductor prevents interaction of the photo-excited charge carriers with the surface of the nanocrystals and thereby improves the photoluminescence quantum yield and the stability towards photo-oxidation. Because of these reasons, inorganically capped nanocrystals are used as light sources in various fields such as biological labelling [59] and photonics [60, 61], and as buildings blocks for solar cells, light-harvesting materials [62] and light emitting diodes [63].

1.6 Random photonic materials

Besides crystalline photonic materials with a photonic bandgap and defects there is a second class of materials in which localisation of light can occur: under certain conditions very strong scattering in random porous materials can completely stop wave-propagation. This phenomenon is called Anderson localisation, after P. W. Anderson who introduced the concept in the context of electron propagation in disordered metals [64]. Anderson localisation is a wave phenomenon and can therefore also occur with light waves.

In random porous materials which scatter light without absorption and

in which interference plays a minor role, transmission can be described in analogy with Ohm's law for electron transport. Due to multiple scattering in these materials light propagation becomes diffusive, i.e., the wave undergoes a random walk. The diffusion constant D is given by [65]

$$D = \frac{1}{3} v_e \ell \tag{1.14}$$

where v_e is the energy velocity and ℓ the transport mean free path, or the distance over which the propagation direction of the light is randomised.

When interference plays an important role one speaks of weak localisation. In this case there is a finite probability that the wave returns to its source via a so-called 'time reversed path' [65]. The difference in length between time-reversed paths is zero. As a consequence, constructive interference occurs and this increases the intensity at the source of the wave. Weak localisation results in a reduction of the diffusion constant in eq. 1.14. The observation of enhanced backscattering in reflection measurements, in addition to a diffuse background, reveals the existence of interference effects or weak localisation [66, 67]. One speaks of strong or Anderson localisation when diffusive transport completely breaks down due to interference [65]. In this case the wave returns to its source, which means that $\ell = 0$, and the intensity decays exponentially with distance.

Sound evidence for Anderson localisation in three-dimensional random porous materials has not yet been reported. Difficulties in meeting the material requirements are the main reason for this. Localisation of near infrared light in powders of gallium arsenide (GaAs) was described in 1997 [68]. However, absorption due to surface states was a complicating factor leading to an ambiguous interpretation of the results; absorption of light and Anderson localisation can easily be confused since both phenomena have a similar experimental signature [69, 70].

Very strong multiple scattering of visible light has been reported for porous gallium phosphide (GaP) [71]. Anodic etching of n-type GaP in sulfuric acid (H_2SO_4) solution gives random porous networks [72]. Figure 1.5 shows a scanning electron microscopy image of such a random network. The average pore diameter is $\sim$ 50 nm. Optimisation of the etching process has yielded the strongest random scattering medium for visible light known to date [71]; a transport mean free path as small as 0.17 μm was

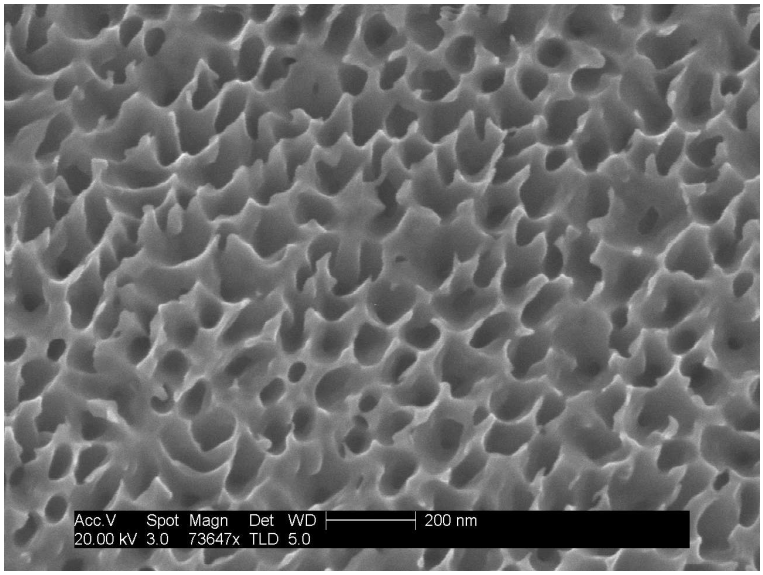

Figure 1.5: *Scanning electron microscopy image of a random porous GaP network. Single-crystalline GaP, with a dopant density of 10-20$\times 10^{17}$ cm^{-3} was etched at a potential of 7 V in aqueous 0.5 mol/l H_2SO_4 solution. The average diameter of the pores is $\sim$ 50 nm.*

reported. Evidence for the onset of Anderson localisation of light was observed in this system [73].

Besides the strong light scattering power of porous GaP, porosifaction leads to other interesting material properties. Porous photo-anodes have an extraordinarily high quantum efficiency: almost all the supra-bandgap photons incident on the interface are converted to electron-hole pairs [74]. The pores in porous GaP are not completely randomly oriented. Anisotropy in the direction of the pores leads to anisotropic diffusion of light [75]. The electron transport in porous GaP permeated with electrolyte solution has been studied by analysis of the photocurrent response upon small-amplitude modulation of the light intensity. It was found that the transport is characterised by a single transit time that depends on the thickness of the porous layer [76].

In the course of the research presented in this thesis an interesting aspect of macroporous GaP was discovered. During porous etching electroluminescence is generated at the pore tips. It will be shown that this light emission gives information about both the mechanism of etching and that it

can be used to study the photonic properties of the semiconductor system.

1.7 Outline of the thesis

In this thesis experimental results on the optical properties of light sources in ordered and random macroporous photonic materials are described. The first part of the thesis (Chapters 2-5) concerns the optical properties of semiconductor nanocrystals in suspensions and in photonic crystals. The main goal of this research was to determine the influence of a photonic crystal on the radiative decay rate of embedded nanocrystals (Chapter 5). In the second part (Chapters 6 & 7) experiments with light sources in random porous GaP are reported.

- The first step on the road to studying spontaneous emission in photonic crystals is the preparation of the light source, i.e., the semiconductor nanocrystals. In Chapter 2 synthesis and characterisation of CdTe nanocrystals and CdSe nanocrystals capped with ZnSe are reported. These materials were prepared by wet-chemical synthesis. To study the nucleation and growth of the nanocrystals, samples were taken at regular times during synthesis. The samples were dispersed in solution and the optical characteristics, i.e., absorption and emission, were measured.

- Chapter 3 describes photoluminescence lifetime measurements. A mathematical analysis is presented of single-, stretched- and multi-exponential models. The relation between the concentration of excited emitters and the luminescence decay curve is derived, and the proper normalisation and the average decay times for the models are deduced. This is the first report on the statistical analysis of multi-exponential decay models. The analysis of the various exponential decay models enabled us to extract key information on nanocrystal physics from our luminescence decay curves.

- In Chapter 4 the dependence of the radiative decay rate of suspended CdSe and CdTe nanocrystals on the emission frequency is considered; experimental results are compared to quantum mechanical theory. The nearly single-exponential photoluminescence decay curves were

analysed with the models presented in Chapter 3. Surprisingly, experimental results show that the decay rate increases with frequency, even in a supra-linear way with frequency. Comparison with theory shows that this increase can be explained by thermal population of various hole levels located close to the top of the valence band.

- In Chapter 5 experiments with titania inverse opal photonic crystals, which were doped with ZnSe-capped CdSe nanocrystals, are reported. It is shown that both the spectral distribution and the time-dependent response are controlled by the photonic crystal host. At a fixed emission frequency, the radiative rate varies by at least a factor three with varying lattice parameter of the photonic crystal, in agreement with the theoretical photonic density of states. A variation of a factor-of-six in the width of the decay rate distribution was observed and identified with the spatial variation of the local density of optical modes probed by the nanocrystals at various positions in the unit-cell. These measurements are the first experimental demonstration of the use of photonic crystals to control the radiative lifetime of emitters.

- Chapters 6 & 7 describe experiments with light sources in random porous GaP. Single-crystalline GaP can be made porous by electrochemical etching. In Chapter 6 it is shown that during porous etching electroluminescence is generated. The emission spectra, which include a supra-band gap contribution, are markedly different from the spectra observed under optical excitation or minority carrier injection. The spectral characteristics of the luminescence suggest that both thermalised and hot charge carriers, generated by impact ionisation, are involved in light emission.

- In the experiments reported in Chapter 7 the electroluminescence is used as an internal light source to measure the wavelength-dependent transmission of light through growing porous layers. We show that the intensity of supra-bandgap light decays single-exponentially with porous layer thickness, as a result of light absorption in the porous layer. The intensity of sub-bandgap light decays with the inverse of the porous layer thickness, as a result of diffusion of light.

The transport mean free path is deduced for the complete wavelength range.

References

[1] B. C. van Fraassen, *The Scientific Image* (Oxford Univesity Press Inc., New York, 1980).

[2] T. Justel, H. Nikol, and C. Ronda, *New developments in the field of luminescent materials for lighting and displays*, Angewandte Chemie-International Edition **37**, 3085 (1998).

[3] V. P. Bykov, *Spontaneous emission from a medium with a band spectrum*, Soviet Journal of Quantum Electronics **4**, 861 (1975).

[4] E. Yablonovitch, *Inhibited spontaneous emission in solid-state physics and electronics*, Physical Review Letters **58**, 2059 (1987).

[5] B. O'Regan and M. Grätzel, *A low-cost, high-efficiency solar-cell based on dye-sensitized colloidal TiO_2 films*, Nature **353**, 737 (1991).

[6] S. Nishimura, N. Abrams, B. A. Lewis, L. I. Halaoui, T. E. Mallouk, K. D. Benkstein, J. van de Lagemaat, and A. J. Frank, *Standing wave enhancement of red absorbance and photocurrent in dye-sensitized titanium dioxide photoelectrodes coupled to photonic crystals*, Journal of the American Chemical Society **125**, 6306 (2003).

[7] R. T. Wegh, H. Donker, K. D. Oskam, and A. Meijerink, *Visible quantum cutting in $LiGdF_4 : Eu^{3+}$ through downconversion*, Science **283**, 663 (1999).

[8] C. M. Soukoulis, *Photonic Bandgap Materials* (Kluwer, Dordrecht, 1996).

[9] T. J. Barton, L. M. Bull, W. G. Klemperer, D. A. Loy, B. McEnaney, M. Misono, P. A. Monson, G. Pez, G. W. Scherer, J. C. Vartuli, and O. M. Yaghi, *Tailored porous materials*, Chemistry of Materials **11**, 2633 (1999).

[10] S. John, *Strong localization of photons in certain disordered dielectric superlattices*, Physical Review Letters **58**, 2486 (1987).

[11] B. Henderson and G. Imbusch, *Optical Spectroscopy of Inorganic Solids* (Clarendon Press, Oxford, UK, 1989).

[12] R. Loudon, *The Quantum Theory of Light*, 3rd ed. (Oxford University Press Inc., New York, 2001).

[13] S. Noda, K. Tomoda, N. Yamamoto, and A. Chutinan, *Full three-dimensional photonic bandgap crystals at near-infrared wavelengths*, Science **289**, 604 (2000).

[14] A. Blanco, E. Chomski, S. Grabtchak, M. Ibisate, S. John, S. W. Leonard, C. Lopez, F. Meseguer, H. Miguez, J. P. Mondia, G. A. Ozin, O. Toader, and H. M. van Driel, *Large-scale synthesis of a silicon photonic crystal with a complete three-dimensional bandgap near 1.5 micrometres*, Nature **405**, 437 (2000).

[15] Y. A. Vlasov, X. Z. Bo, J. C. Sturm, and D. J. Norris, *On-chip natural assembly of silicon photonic bandgap crystals*, Nature **414**, 289 (2001).

[16] K. M. Ho, C. T. Chan, and C. M. Soukoulis, *Existence of a photonic gap in periodic dielectric structures*, Physical Review Letters **65**, 3152 (1990).

[17] H. S. Sozuer, J. W. Haus, and R. Inguva, *Photonic bands - Convergence problems with the plane-wave method*, Physical Review B **45**, 13962 (1992).

[18] K. Busch and S. John, *Photonic band gap formation in certain self-organizing systems*, Physical Review E **58**, 3896 (1998).

[19] A. F. Koenderink, *Emission and Transport of Light in Photonic Crystals* (Ph.D. thesis, University of Amsterdam, Amsterdam, 2003).

[20] J. E. G. J. Wijnhoven, L. Bechger, and W. L. Vos, *Fabrication and characterization of large macroporous photonic crystals in titania*, Chemistry of Materials **13**, 4486 (2001).

[21] A. F. Koenderink, L. Bechger, H. P. Schriemer, A. Lagendijk, and W. L. Vos, *Broadband fivefold reduction of vacuum fluctuations probed by dyes in photonic crystals*, Physical Review Letters **88**, 143903 (2002).

[22] S. P. Ogawa, M. Imada, S. Yoshimoto, M. Okano, and S. Noda, *Control of light emission by 3D photonic crystals*, Science **305**, 227 (2004).

[23] J. Martorell and N. M. Lawandy, *Observation of inhibited spontaneous emission in a periodic dielectric structure*, Physical Review Letters **65**, 1877 (1990).

[24] B. Y. Tong, P. K. John, Y. T. Zhu, Y. S. Liu, S. K. Wong, and W. R. Ware, *Fluorescence-lifetime measurements in monodispersed suspensions of polystyrene particles*, Journal of the Optical Society of America B-Optical Physics **10**, 356 (1993).

[25] E. P. Petrov, V. N. Bogomolov, I. I. Kalosha, and S. V. Gaponenko, *Spontaneous emission of organic molecules embedded in a photonic crystal*, Physical Review Letters **81**, 77 (1998).

[26] M. Megens, H. P. Schriemer, A. Lagendijk, and W. L. Vos, *Comment on "Spontaneous emission of organic molecules embedded in a photonic crystal"*, Physical Review Letters **83**, 5401 (1999).

[27] E. P. Petrov, V. N. Bogomolov, I. I. Kalosha, and S. V. Gaponenko, *Comment on "Spontaneous emission of organic molecules embedded in a photonic crystal" - Reply*, Physical Review Letters **83**, 5402 (1999).

[28] Z. Y. Li and Z. Q. Zhang, *Weak photonic band gap effect on the fluorescence lifetime in three-dimensional colloidal photonic crystals*, Physical Review B **6312**, 125106 (2001).

[29] J. Y. Zhang, X. Y. Wang, M. Xiao, and Y. H. Ye, *Modified spontaneous emission of CdTe quantum dots inside a photonic crystal*, Optics Letters **28**, 1430 (2003).

[30] V. G. Solovyev, S. G. Romanov, C. M. S. Torres, M. Muller, R. Zentel, N. Gaponik, A. Eychmuller, and A. L. Rogach, *Modification of the spontaneous emission of CdTe nanocrystals in TiO_2 inverted opals*, Journal of Applied Physics **94**, 1205 (2003).

[31] L. Bechger, *Synthesis and Fluorescence of Opal & Air-Sphere Photonic Crystals* (Ph.D. thesis, University of Twente, Enschede, 2003).

[32] U. Brackmann, *Laser Dyes*, 3rd ed. (Lambda Physik AG, Goettingen, Germany, 2000).

[33] A. L. Efros, M. Rosen, M. Kuno, M. Nirmal, D. J. Norris, and M. G. Bawendi, *Band-edge exciton in quantum dots of semiconductors with a degenerate valence band: Dark and bright exciton states*, Physical Review B **54**, 4843 (1996).

[34] C. B. Murray, C. R. Kagan, and M. G. Bawendi, *Synthesis and characterization of monodisperse nanocrystals and close-packed nanocrystal assemblies*, Annual Review of Materials Science **30**, 545 (2000).

[35] B. O. Dabbousi, J. Rodriguez-Viejo, F. V. Mikulec, J. R. Heine, H. Mattoussi, R. Ober, K. F. Jensen, and M. G. Bawendi, *(CdSe)ZnS core-shell quantum dots: Synthesis and characterization of a size series of highly luminescent nanocrystallites*, Journal of Physical Chemistry B **101**, 9463 (1997).

[36] D. V. Talapin, A. L. Rogach, A. Kornowski, M. Haase, and H. Weller, *Highly luminescent monodisperse CdSe and CdSe/ZnS nanocrystals synthesized in a hexadecylamine-trioctylphosphine oxide- trioctylphospine mixture*, Nano Letters **1**, 207 (2001).

[37] A. F. Koenderink, L. Bechger, A. Lagendijk, and W. L. Vos, *An experimental study of strongly modified emission in inverse opal photonic crystals*, Physica Status Solidi A **197**, 648 (2003).

[38] S. V. Gaponenko, V. N. Bogomolov, E. P. Petrov, A. M. Kapitonov, D. A. Yarotsky, I. Kalosha, A. A. Eychmueller, A. L. Rogach, J. McGilp, U. Woggon, and F. Gindele, *Spontaneous emission of dye molecules, semiconductor nanocrystals, and rare-earth ions in opal-based photonic crystals*, Journal of Lightwave Technology **17**, 2128 (1999).

[39] N. Danz, J. Heber, and A. Brauer, *Fluorescence lifetimes of molecular dye ensembles near interfaces*, Physical Review A **66**, 063809 (2002).

[40] M. Megens, J. E. G. J. Wijnhoven, A. Lagendijk, and W. L. Vos, *Fluorescence lifetimes and linewidths of dye in photonic crystals*, Physical Review A **59**, 4727 (1999).

[41] H. P. Schriemer, H. M. van Driel, A. F. Koenderink, and W. L. Vos, *Modified spontaneous emission spectra of laser dye in inverse opal photonic crystals*, Physical Review A **A63**, 011801 (2001).

[42] J. Kalkman, E. de Bres, A. Polman, Y. Jun, D. J. Norris, D. C. 't Hart, J. P. Hoogenboom, and A. van Blaaderen, *Selective excitation of erbium in silicon-infiltrated silica colloidal photonic crystals*, Journal of Applied Physics **95**, 2297 (2004).

[43] M. Grundmann, J. Christen, N. N. Ledentsov, J. Bohrer, D. Bimberg, S. S. Ruvimov, P. Werner, U. Richter, U. Gosele, J. Heydenreich, V. M. Ustinov, A. Y. Egorov, A. E. Zhukov, P. S. Kopev, and Z. I. Alferov, *Ultranarrow luminescence lines from single quantum dots*, Physical Review Letters **74**, 4043 (1995).

[44] S. A. Empedocles, D. J. Norris, and M. G. Bawendi, *Photoluminescence spectroscopy of single CdSe nanocrystallite quantum dots*, Physical Review Letters **77**, 3873 (1996).

[45] U. Woggon, S. Gaponenko, W. Langbein, A. Uhrig, and C. Klingshirn, *Homogeneous linewidth of confined electron-hole-pair states in II-VI-quantum dots*, Physical Review B **47**, 3684 (1993).

[46] K. Takemoto, B. R. Hyun, and Y. Masumoto, *Heterodyne-detected accumulated photon echo in CdSe quantum dots*, Solid State Communications **114**, 521 (2000).

[47] M. Shim and P. Guyot-Sionnest, *Intraband hole burning of colloidal quantum dots*, Physical Review B **64**, 245342 (2001).

[48] P. Palinginis and H. L. Wang, *High-resolution spectral hole burning in CdSe/ZnS core/shell nanocrystals*, Applied Physics Letters **78**, 1541 (2001).

[49] W. G. J. H. M. van Sark, P. L. T. M. Frederix, A. A. Bol, H. C. Gerritsen, and A. Meijerink, *Blueing, bleaching, and blinking of single CdSe/ZnS quantum dots*, ChemPhysChem **3**, 871 (2002).

[50] G. Schlegel, J. Bohnenberger, I. Potapova, and A. Mews, *Fluorescence decay time of single semiconductor nanocrystals*, Physical Review Letters **88**, 137401 (2002).

[51] F. Koberling, U. Kolb, G. Philipp, I. Potapova, T. Basche, and A. Mews, *Fluorescence anisotropy and crystal structure of individual semiconductor nanocrystals*, Journal of Physical Chemistry B **107**, 7463 (2003).

[52] C. B. Murray, D. J. Norris, and M. G. Bawendi, *Synthesis and characterization of nearly monodisperse CdE (E = S, Se, Te) semiconductor nanocrystallites*, Journal of the American Chemical Society **115**, 8706 (1993).

[53] S. V. Gaponenko, *Optical Properties of Semiconductor Nanocrystals* (Cambridge University Press, Cambridge, UK, 1998).

[54] A. D. Yoffe, *Low-dimensional systems: Quantum-size effects and electronic properties of semiconductor microcrystallites (zero-dimensional systems) and some quasi-2-dimensional systems*, Advances in Physics **42**, 173 (1993).

[55] A. L. Efros and A. L. Efros, *Interband light absorption in a semiconductor sphere*, Fizika i Tekhnika Poluprovodnikov (Sankt-Peterburg) **16**, 1209 (1982).

[56] L. E. Brus, *Electron-electron and electron-hole interactions in small semiconductor crystallites: the size dependence of the lowest excited electronic state*, Journal of Chemical Physics **80**, 4403 (1984).

[57] D. J. Norris and M. G. Bawendi, *Measurement and assignment of the size-dependent optical spectrum in CdSe quantum dots*, Physical Review B **53**, 16338 (1996).

[58] C. de Mello Donegá, P. Liljeroth, and D. Vanmaekelbergh, *Physico-chemical evaluation of the hot-injection method, a synthesis route for monodisprese nanocrystals*, Small **1**, 1152 (2005).

[59] M. Bruchez, M. Moronne, P. Gin, S. Weiss, and A. P. Alivisatos, *Semiconductor nanocrystals as fluorescent biological labels*, Science **281**, 2013 (1998).

[60] M. Fujita, S. Takahashi, Y. Tanaka, T. Asano, and S. Noda, *Simultaneous inhibition and redistribution of spontaneous light emission in photonic crystals*, Science **308**, 1296 (2005).

[61] A. Kress, F. Hofbauer, N. Reinelt, M. Kaniber, H. J. Krenner, R. Meyer, G. Bohm, and J. J. Finley, *Manipulation of the spontaneous emission dynamics of quantum dots in two-dimensional photonic crystals*, Physical Review B **71**, 241304 (2005).

[62] S. A. Crooker, J. A. Hollingsworth, S. Tretiak, and V. I. Klimov, *Spectrally resolved dynamics of energy transfer in quantum-dot assemblies: Towards engineered energy flows in artificial materials*, Physical Review Letters **89**, 186802 (2002).

[63] S. Coe, W. K. Woo, M. G. Bawendi, and V. Bulovic, *Electroluminescence from single monolayers of nanocrystals in molecular organic devices*, Nature **420**, 800 (2002).

[64] P. W. Anderson, *Absence of diffusion in certain random lattices*, Physical Review **109**, 1492 (1958).

[65] J. Gómez Rivas, *Light in Strongly Scattering Semiconductors* (Ph.D. thesis, University of Amsterdam, Amsterdam, 2002).

[66] M. P. van Albada and A. Lagendijk, *Observation of weak localization of light in a random medium*, Physical Review Letters **55**, 2692 (1985).

[67] P. E. Wolf and G. Maret, *Weak localization and coherent backscattering of photons in disordered media*, Physical Review Letters **55**, 2696 (1985).

[68] D. S. Wiersma, P. Bartolini, A. Lagendijk, and R. Righini, *Localization of light in a disordered medium*, Nature **390**, 671 (1997).

[69] F. Scheffold, R. Lenke, R. Tweer, and G. Maret, *Localization or classical diffusion of light?*, Nature **398**, 206 (1999).

[70] D. S. Wiersma, J. G. Rivas, P. Bartolini, A. Lagendijk, and R. Righini, *Localization or classical diffusion of light? Reply*, Nature **398**, 207 (1999).

[71] F. J. P. Schuurmans, D. Vanmaekelbergh, J. van de Lagemaat, and A. Lagendijk, *Strongly photonic macroporous gallium phosphide networks*, Science **284**, 141 (1999).

[72] B. H. Erné, D. Vanmaekelbergh, and J. J. Kelly, *Morphology and strongly enhanced photoresponse of GaP electrodes made porous by anodic etching*, Journal of the Electrochemical Society **143**, 305 (1996).

[73] F. J. P. Schuurmans, M. Megens, D. Vanmaekelbergh, and A. Lagendijk, *Light scattering near the localization transition in macroporous GaP networks*, Physical Review Letters **83**, 2183 (1999).

[74] B. H. Erné, D. Vanmaekelbergh, and J. J. Kelly, *Porous etching - a means to enhance the photoresponse of indirect semiconductors*, Advanced Materials **7**, 739 (1995).

[75] P. M. Johnson, B. P. J. Bret, J. Gómez Rivas, J. J. Kelly, and A. Lagendijk, *Anisotropic diffusion of light in a strongly scattering material*, Physical Review Letters **89**, 243901 (2002).

[76] A. L. Roest, P. E. de Jongh, and D. Vanmaekelbergh, *Nondispersive trap-limited electron transport in macroporous GaP*, Physical Review B **62**, 16926 (2000).

Chapter 2

Synthesis and characterisation of highly luminescent semiconductor nanocrystals

abstract

CdTe nanocrystals and CdSe nanocrystals capped with ZnSe (core-shell structures) were synthesised. CdTe was made by slow heating of Cd- and Te-precursors in a coordinating solvent and CdSe was made by injection of the precursors into a hot coordinating solvent. The CdTe nanocrystals were re-capped with hexanethiol and the CdSe nanocrystals were covered with a ZnSe shell. This led to an improvement of the optical properties; the photoluminescence quantum efficiency increased and the luminescence decay became nearly single-exponential. These properties make our nanocrystals an ideal model system to study the size-dependent rate of radiative exciton recombination.

2.1 Introduction

Nanocrystalline semiconductor colloids, also called quantum dots, belong to a state of matter that is intermediate between molecules and solids. Their size-dependent physical and chemical properties, i.e. 'quantum size effects', are currently investigated in various fields of science. Some experimental evidence for the existence of quantum size effects was published before 1980 [1–3]. However, a fast development of the research on colloidal nanocrystals started in 1982 [4–8]. An important step forward was made in 1993, when Murray, Norris and Bawendi [9] published a very powerful wet-chemical synthesis route to prepare high-quality monodisperse CdS, CdTe and CdSe nanocrystals. The synthesis is based on the pyrolysis of organometallic reagents by injection into a hot coordinating solvent. Since then, this synthesis route has been adapted for many types of semiconductor nanocrystals (for an overview, see Ref. [10]). Modification and improvement of this method [11–16] resulted in synthesis products with a high photoluminescence efficiency ($\leq$80 %), a high monodispersity ($\geq$ 5%) and a good control over the size and shape.

In this Chapter the synthesis of CdTe and ZnSe-capped CdSe nanocrystals will be described. The synthesis routes and materials were chosen on basis of the reported high photoluminescence quantum efficiency of these nanocrystals in the near infrared and visible range of the spectrum [12, 13]. Therefore, these nanocrystals are promising candidates as probes in photonic studies. Experiments reported in this Chapter describe the nucleation and growth of the nanocrystals in further detail with respect to the original reports on the same synthesis procedures [12, 13]. For the synthesis of CdTe nanocrystals a method similar to the one described by Talapin et al. [12] was used. CdTe nanocrystals were prepared by slow heating of a mixture containing Cd- and Te- precursors and a coordinating solvent. After synthesis, the nanocrystals were re-capped with hexanethiol to improve the optical properties. Thiol-functionalised molecules easily replace the amine capping of the raw product [17]. In this way the surface chemistry can be changed and CdTe nanocrystals can even be transferred to a completely polar solvent such as water. The synthesis of ZnSe-capped CdSe nanocrystals will be described in the last part of this Chapter. For the synthesis of CdSe nanocrystals a method described by Talapin et al. [13] and de Mello

Donegá et al. [16] was applied. In contrast to the method described above for the CdTe synthesis, CdSe nanocrystals were prepared by injection of Cd- and Se-precursors into a hot coordinating solvent. The most important modifications with respect to the synthesis route as reported by Murray et al. [9] concern the reaction volume and temperature, the use of a dehydrating agent and a large Se/Cd ratio, as developed by de Mello Donegá et al. [16]. After preparation of the CdSe nanocrystals a ZnSe shell was grown on the surface [18]. ZnSe is an ideal passivating material for CdSe since it has a larger bandgap (2.72 eV where CdSe has a bandgap of 1.76 eV) and a small lattice mismatch of 6.3% [19].

2.2 Experimental

2.2.1 CdTe nanocrystal synthesis

The synthesis of CdTe nanocrystals was performed in an argon-purged glovebox with an oxygen and water content less than 2 ppm. In a three-necked flask 10 g of dry dodecylamine (DDA) and 7 mL of trioctylphosphine (TOP) were heated to 50°C. To the solution of DDA and TOP were added 0.22 g (1.5×10^{-3} mol) dimethyl cadmium ($Cd(Me)_2$) in 7 mL of TOP and 0.16 g (1.3×10^{-3} mol) Te powder. A Cd/Te ratio of about 1.25 was used in all the syntheses performed. The reaction mixture was slowly heated ($\sim$1.5°C/min) until the final temperature was reached. At about 135°C the reaction mixture turned from grey to green when the tellurium starts to dissolve and the TOP-Te complex is formed [12]. This was set as t = 0 min. The TOP-Te complex can form even at room temperature; the temperature at which dissolution of Te was observed is not determined by thermodynamics. The applied temperature-ramp plays a critical role in this process. Syntheses were performed with final temperatures of 145°C, 165°C and 180°C. To follow the particle growth in time for these temperatures, small aliquots of about 0.5 mL were taken at regular intervals during the growth of the quantum dots and dispersed in toluene. Excess of Cd and Te was not removed during storage.

The capping of the raw product of the synthesis (DDA) was subsequently replaced by a thiol-capping. To this end 150 μl of the raw product was dispersed in 5 ml chloroform. To this suspension of nanocrystals in

chloroform 200 μl of hexanethiol in chloroform (1 mol/l) was added. After addition of hexanethiol, suspensions were used in optical measurements, without further processing.

2.2.2 ZnSe[CdSe] nanocrystal synthesis

The synthesis was performed in an argon-purged glovebox with an oxygen and water content less than 2 ppm. The coordinating solvent consisted of 15 g hexadecylamine (HDA) and 15 g trioctylphosphine oxide (TOPO). To the coordinating solvent 2 ml of anhydrous triethylorthoformate (TEOF) was added and the solution was heated and stirred. After heating for 30 min at 220°C the solution temperature was increased to 330°C. During the final heating step the colour of the coordinating solvent turned from colourless to 'goldish'. Meanwhile, a solution was prepared containing 0.28 g (2.0×10^{-3} mol) $Cd(Me)_2$, 0.8 g (1.0×10^{-2} mol) Se and 10 ml TOP. The heating mantle was removed and at 300°C the solution with Cd- and Se- precursors in TOP was quickly injected into the coordinating solvent. The temperature of the mixture was allowed to drop to 170°C, after which the heater was replaced. The temperature was then increased and left for approximately 2 hours at 240 °C. After annealing at 240 °C, a solution of 0.8 g Se, 0.28 g $Cd(Me)_2$ in 10 ml TOP was added drop-wise (10 ml/hour). At the end, half of the mixture was removed. To grow a ZnSe shell around the CdSe nanocrystals, a method based on Ref. [18] was applied. To the remaining half of the mixture a solution containing 1.5 g zinc stearate ($Zn(C_{18}H_{35}O_2)_2$) and 10 ml toluene was added drop-wise (10 ml/hour) at 190°C.

2.2.3 Characterisation

Absorption spectra were recorded with a Perkin-Elmer Lambda 16 UV/VIS spectrometer. The optical density at the first absorption peak of the nanocrystal suspensions taken during synthesis was smaller than 0.05. This means that the suspensions are sufficiently dilute that energy-transfer between the nanocrystals can be excluded. For luminescence measurements samples were excited at 400 nm. Spectra were recorded with a Princeton Instruments CCD camera (liquid-nitrogen cooled, 1024 $\times$ 256 pixels) in combination with an Acton Pro monochromator (150 lines/mm, blazed

at 500 nm). The photoluminescence quantum efficiency was determined by comparison of the luminescence spectrum with the luminescence spectrum of Rhodamine 101 (Rhodamine 640) [20] which has a photoluminescence quantum efficiency of 100% [21]. No correction for reabsorption was made since the samples were sufficiently diluted. In diluted samples the effect of reabsorption is too small to have substantial influence on the measured quantum efficiency. The accuracy of the determination of the quantum efficiency was estimated to be $\pm$10%.

Luminescence decay curves were obtained by binning the arrival times of the single photons excited with a Pico Quant picosecond laser (λ_{ex}=406 nm) and detected with a fast Hamamatsu photomultiplier tube. A monochromator with a focal length 0.1 m and a grating with 1350 lines/mm blazed at 500 nm was placed before the detector. The spectral resolution of the monochromator was $<$10 nm. Pulse height analysis was done with a Time Harp 100 computer card. The repetition rate of the laser was 2.5 MHz. Table Curve 2D version 5.0 was used to model decay curves. The decay curves were modelled directly, over the full time range of 400 ns.

2.3 Results and discussion

2.3.1 CdTe nanocrystals

At a temperature of 135 °C the colour of the reaction mixture turns from grey to green. From this moment (t= 0 min) samples were taken from the mixture and dispersed in 3 mL of toluene. Figure 2.1 shows the absorption spectra, which were normalised with respect to the first absorption maximum, and figure 2.2 shows the corresponding emission spectra of samples of CdTe nanocrystals taken at different time intervals for a reaction temperature of 165°C. In the spectra of the samples taken after 0 min and 3.5 min no absorption maximum was observed and these spectra could therefore not be normalised. For this reason these spectra were multiplied with an arbitrary constant value to fit with the other spectra. In the initial stage (t=0 min and t=6.5 min) the emission of the suspensions is mainly due to defects; the emission spectrum is red-shifted with respect exciton-related emission of the larger nanocrystals and is very broad. No clear absorption peak was observed in those samples. At the end of the synthesis (t=300

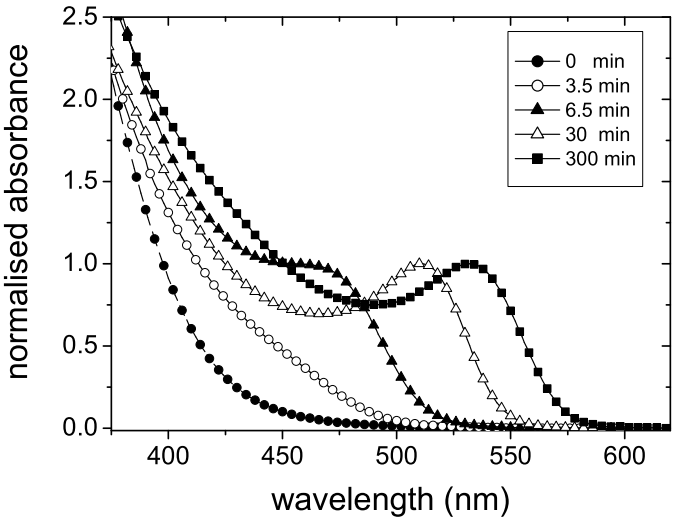

Figure 2.1: *Absorption spectra of samples from aliquots taken during CdTe synthesis. The final temperature of the synthesis was 165°C and the samples were dispersed in toluene. The samples were taken at 0 min (filled dots), 3.5 min (open dots), 6.5 min (filled triangles), 30 min (open triangles) and 300 min (filled squares).*

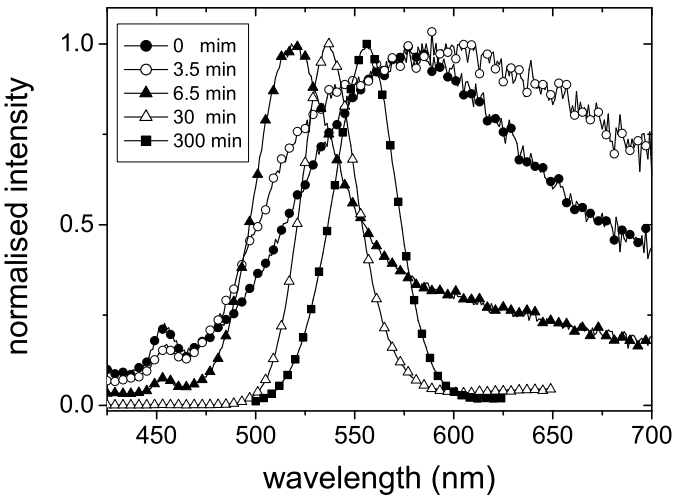

Figure 2.2: *Emission spectra of samples from aliquots taken during CdTe synthesis. The final temperature of the synthesis was 165°C and the samples were dispersed in toluene. The samples were taken at 0 min (filled dots), 3.5 min (open dots), 6.5 min (filled triangles), 30 min (open triangles) and 300 min (filled squares). The suspensions were excited at 400 nm.*

min) the nanocrystals have an excitonic emission with a full width at half maximum (FWHM) of approximately 35 nm (150 meV), indicating that relatively monodisperse particles were obtained. Hardly any defect-related emission was observed in the emission spectra of fresh samples.

To study the influence of the reaction temperature on the final particle size, one synthesis at a higher temperature of 180°C and one at a lower temperature of 145°C were performed. Figure 2.3 shows the maxima of the first absorption peak and the position of the exciton-related emission peak of the samples in toluene taken from the solution at various times for three temperatures (145°C, 165°C and 180°C). In all cases, the maximum of the first absorption peak shifts strongly in the first 30 minutes. The shift shows the increase of the particle-size since larger particles absorb at longer wavelengths. After 30 minutes a smaller change is observed, reflecting a slower growth towards a nearly constant particle size. The final size of the CdTe nanocrystals is determined by the reaction temperature: at higher temperatures larger particles are obtained. This result is similar to what

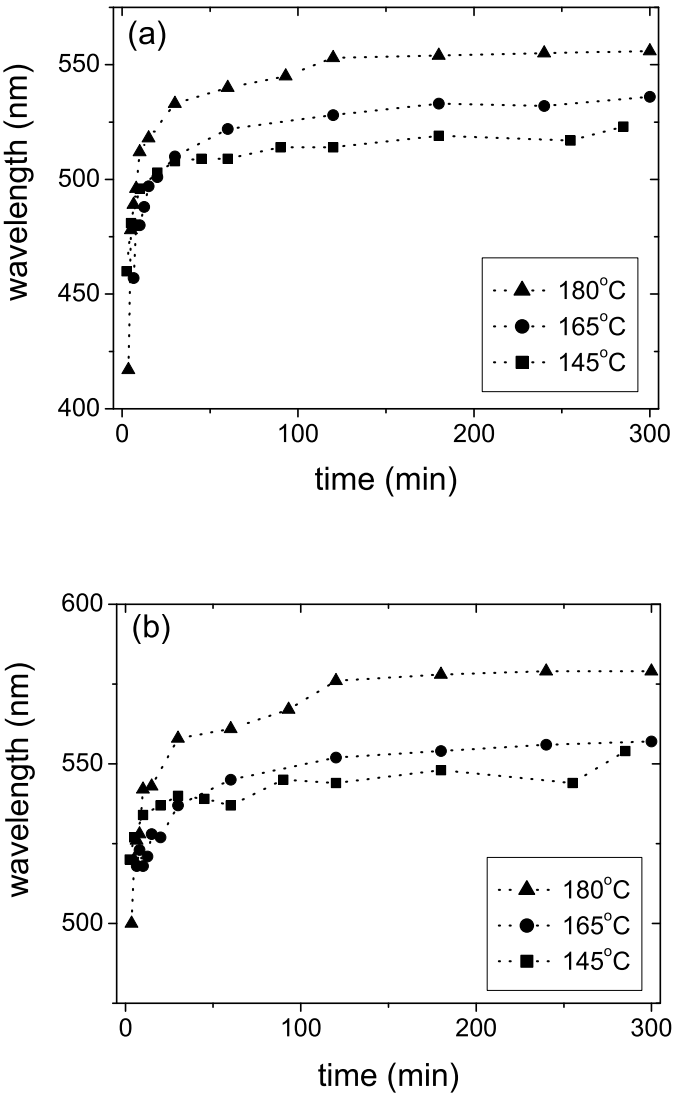

Figure 2.3: *Maximum of the first absorption peak (a) and exciton-related emission peak (b) of CdTe nanocrystals diluted in toluene. The syntheses were performed at 145°C, 165°C and 180°C.*

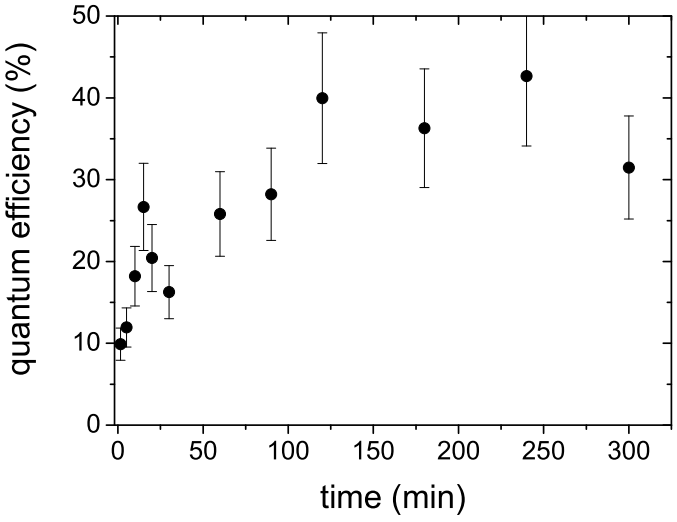

Figure 2.4: *Photoluminescence quantum efficiency of samples taken during CdTe synthesis. The final temperature of the synthesis was 165°C and the samples were dispersed in toluene. The first sample was taken at t=0 min and the last after 300 min.*

has been observed for CdSe quantum dots [16, 22].

The formation of larger particles at higher growth temperature can be understood in terms of thermodynamic equilibrium between the formed nanocrystals and the monomer precursors [10], as proposed by Debye to describe the formation and growth of micelles [23]. When the final temperature is reached (t≈30 min), the monomer precursors are in equilibrium with the nanocrystals and no new nuclei are formed during annealing. Nanocrystal growth from monomer precursors is an endothermic reaction [10]. Increasing the temperature will shift the equilibrium, i.e., the nanocrystals will grow. Thus, at higher temperature, larger nanocrystals are formed. This can be observed in figure 2.3: at higher temperature the absorption and emission maximum are at longer wavelength. The number of nuclei is determined during the initial stage and the choice of ligands is crucial [24–28]. We observed that the temperature ramp and stirring play a critical role in this process. For several syntheses with a lower temperature ramp unstable nanocrystal suspensions were obtained.

After the initial 30 minutes the particle size levels off. During further heating, i.e., annealing, the size did not change but the quantum efficiency improved, as shown in figure 2.4. At the end of the synthesis the nanocrystal suspension had a photoluminescence efficiency of typically 40 %. The luminescence decay curve of the suspension was far from single-exponential and the typical $\frac{1}{e}$-time was 10 ns. The quality of the suspension is improved by applying a post-preparative capping exchange. At the end of the synthesis the CdTe nanocrystals are capped with DDA. The DDA can be easily exchanged with hexanethiol-molecules, which improves the luminescence properties. This leads to an improvement of the quantum efficiency up to 75 %. Furthermore, the luminescence decay curve was much more single-exponential and the decay-time increased to $\sim$25 ns. The high quantum efficiency and a single-exponential luminescence decay curve make these hexanethiol-stablised CdTe nanocrystals ideal probes in photonic studies, as will be shown in Chapter 4.

2.3.2 ZnSe[CdSe] nanocrystals

Figures 2.5 and 2.6 show the absorption and emission spectra of CdSe and ZnSe-capped CdSe from samples taken at various times during the synthesis. In the initial 20 minutes of the synthesis the emission maximum shifts from 530 nm to 580 nm. Only emission related to exciton recombination was observed. The emission between 450 and 480 nm of the sample taken after one minute is probably fluorescence of the reaction solvent [16]. In the spectra of the other samples, which have a much higher quantum efficiency, emission in this spectral range was not observed.

In the synthesis route for CdSe nanocrystals, nucleation and further growth are separated in time. The injection of the Cd- and Se-precursors determines the concentration of the nanocrystal nuclei. During annealing and (drop-wise) addition of new precursor molecules, no new nuclei are formed. Growth of the nanocrystals is believed to occur due to a shift of the thermodynamic equilibrium between the monomers and the already formed nanocrystals [10], as described above for the growth of CdTe nanocrystals. Prolonged heating of the mixture did not result in further particle growth or focussing of the size. The importance of an annealing period during the synthesis in which the nanocrystal size remains constant was

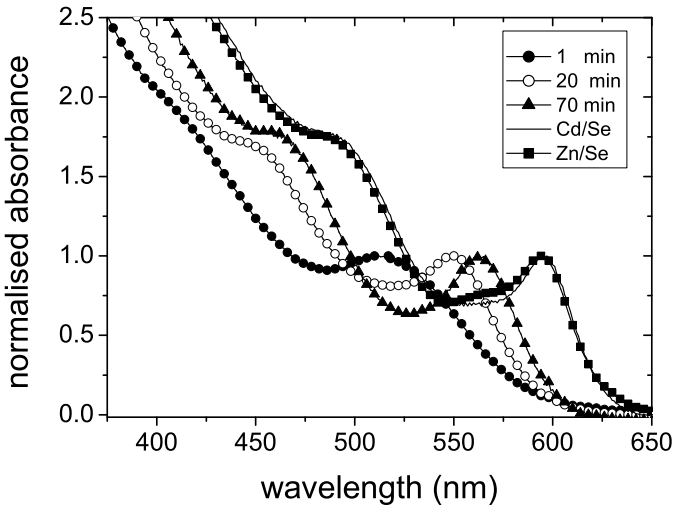

Figure 2.5: *Absorption spectra of samples from aliquots diluted in chloroform taken during ZnSe[CdSe] synthesis. The samples were taken at 1 min (filled dots), 20 min (open dots) and 70 min (filled triangles) after injection, after extra addition of Cd- and Se-precursors and after addition of Zn- and Se-precursors (filled squares).*

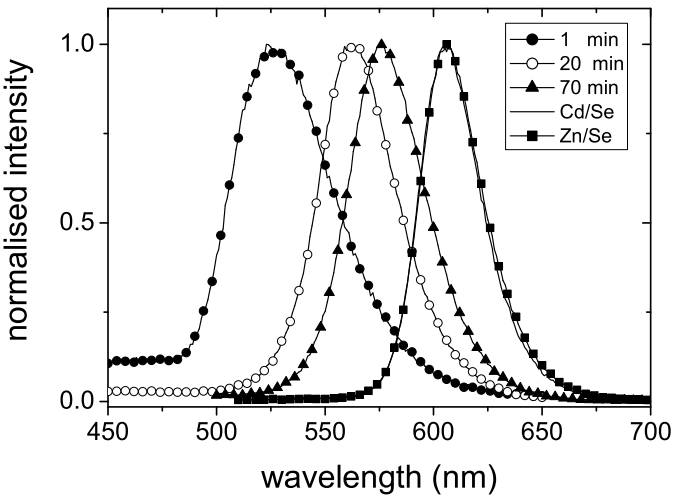

Figure 2.6: *Emission spectra of samples from aliquots diluted in chloroform taken during ZnSe[CdSe] synthesis. The samples were taken at 1 min (filled dots), 20 min (open dots) and 70 min (filled triangles) after injection, after extra addition of Cd- and Se-precursors and after addition of Zn- and Se-precursors (filled squares).*

pointed out by de Mello Donegá et al. [16]. It was shown that further heating at 240°C improves the optical properties of the nanocrystals considerably as a result of surface reconstruction. At the end of the synthesis the FWHM of the emission spectrum was 111 meV, indicating that relatively monodisperse particles were obtained (5% rms [22]). Larger particles can easily be made by increasing the reaction temperature, as described above for CdTe synthesis. A disadvantage of increasing of the temperature is that it reduces the quantum efficiency; it was shown that a high annealing temperature (<240°C) leads to degradation of the nanocrystals due to surface roughening [16]. Therefore, the size was increased by slow addition of Cd- and Se-precursor at 240°C. As a result of the addition, both the absorption and emission spectrum shifted to the red. This means that the extra addition resulted in an increase of the particle size. The final addition of the Zn- and Se-precursor did not result in a shift of the absorption or emission spectrum.

Figure 2.7 shows how the photoluminescence quantum efficiency of the various samples develops during the synthesis. The same trend as in fig-

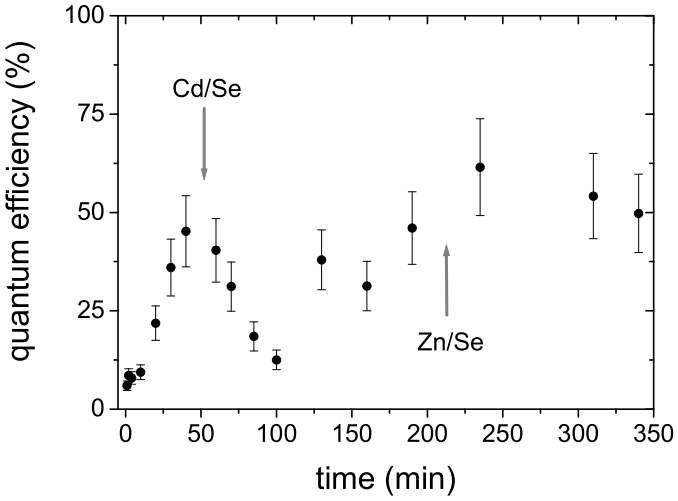

Figure 2.7: *Photoluminescence quantum efficiency of samples taken during ZnSe[CdSe] synthesis. The samples were taken after injection, during extra addition of Cd- and Se-precursor and during addition of Zn- and Se-precursor. Extra Cd- and Se-precursors were added after 50 minutes (left arrow) and Zn- and Se-precursors were added after 220 minutes (right arrow).*

ure 2.7 was also observed in a separate experiment. In the initial stage (t< 25 min) the quantum efficiency is lower than 25 %. Further heating leads to surface reorganisation and an improvement of the quantum efficiency to 45 %. Extra addition of Cd- and Se-precursor at t= 50 min resulted in a drop in the quantum efficiency to 14 % due to roughening of the surface. Annealing at 240°C led to recovery of the quantum efficiency to 45%. The addition of the Zn- and Se-precursor did not result in a decrease of the quantum efficiency, but instead to an increase to 50%. This observation demonstrates the passivating role of the ZnSe layer. The extra addition also leads to surface roughening. However, surface roughening only decreases the quantum yield if this results in bandgap states. ZnSe has a large bandgap and apparently does not create bandgap states and therefore is a good passivating material for CdSe. Passivation of the CdSe nanocrystals with ZnSe also leads to a better stability towards photobleaching.

2.4 Conclusion and outlook

Colloidal suspensions of CdTe and ZnSe-capped CdSe nanocrystals were synthesised. The suspensions have a quantum efficiency of typically 50% and show nearly single-exponential decay of the exciton luminescence as will be shown in Chapter 4. These properties make our nanocrystals an ideal model system to study the size-dependent rate of radiative exciton recombination. CdTe nanocrystals are extremely sensitive to oxygen and water which makes them difficult to handle in ambient condition. CdSe nanocrystals can easily be capped with an inorganic layer as ZnSe. ZnSe has a wider bandgap than CdSe and therefore these particles are much more stable towards photobleaching. This make these nanocrystals ideal probes in optical systems such as those described in Chapter 5.

References

[1] G. Jaeckel, *Some modern absorption glasses*, Zeitschrift fuer Technische Physik **7**, 301 (1926).

[2] C. R. Berry, *Structure and optical absorption of silver iodide microcrystals*, Physical Review **161**, 848 (1967).

[3] R. Dingle, W. Wiegmann, and C. H. Henry, *Quantum states of confined carriers in very thin aluminum gallium arsenide (AlxGa1-xAs)-gallium arsenide-aluminum gallium arsenide(AlxGa1-xAs) heterostructures*, Physical Review Letters **33**, 827 (1974).

[4] R. Rossetti and L. Brus, *Electron-hole recombination emission as a probe of surface chemistry in aqueous cadmium sulfide colloids*, Journal of Physical Chemistry **86**, 4470 (1982).

[5] A. L. Efros and A. L. Efros, *Interband light absorption in a semiconductor sphere*, Fizika i Tekhnika Poluprovodnikov (Sankt-Peterburg) **16**, 1209 (1982).

[6] A. Henglein, *Photodegradation and fluorescence of colloidal cadmium sulfide in aqueous solution*, Berichte der Bunsen-Gesellschaft **86**, 301 (1982).

[7] A. I. Ekimov and A. A. Onushchenko, *Exciton spectroscopy study of the formation of copper halide microcrystals in glasses*, Fizika i Khimiya Stekla **8**, 635 (1982).

[8] A. I. Ekimov and A. A. Onushchenko, *Quantum size effect in optical spectra of semiconductor microcrystals*, Fizika i Tekhnika Poluprovodnikov (Sankt-Peterburg) **16**, 1215 (1982).

[9] C. B. Murray, D. J. Norris, and M. G. Bawendi, *Synthesis and characterization of nearly monodisperse CdE (E = S, Se, Te) semiconductor nanocrystallites*, Journal of the American Chemical Society **115**, 8706 (1993).

[10] C. de Mello Donegá, P. Liljeroth, and D. Vanmaekelbergh, *Physico-chemical evaluation of the hot-injection method, a synthesis route for monodisprese nanocrystals*, Small **1**, 1152 (2005).

[11] B. O. Dabbousi, J. Rodriguez-Viejo, F. V. Mikulec, J. R. Heine, H. Mattoussi, R. Ober, K. F. Jensen, and M. G. Bawendi, *(CdSe)ZnS core-shell quantum dots: Synthesis and characterization of a size series of highly luminescent nanocrystallites*, Journal of Physical Chemistry B **101**, 9463 (1997).

[12] D. V. Talapin, S. Haubold, A. L. Rogach, A. Kornowski, M. Haase, and H. Weller, *A novel organometallic synthesis of highly luminescent CdTe nanocrystals*, Journal of Physical Chemistry B **105**, 2260 (2001).

[13] D. V. Talapin, A. L. Rogach, A. Kornowski, M. Haase, and H. Weller, *Highly luminescent monodisperse CdSe and CdSe/ZnS nanocrystals synthesized in a hexadecylamine-trioctylphosphine oxide- trioctylphospine mixture*, Nano Letters **1**, 207 (2001).

[14] Z. A. Peng and X. G. Peng, *Formation of high-quality CdTe, CdSe, and CdS nanocrystals using CdO as precursor*, Journal of the American Chemical Society **123**, 183 (2001).

[15] Z. A. Peng and X. G. Peng, *Nearly monodisperse and shape-controlled CdSe nanocrystals via alternative routes: Nucleation and growth*, Journal of the American Chemical Society **124**, 3343 (2002).

[16] C. de Mello Donegá, S. G. Hickey, S. F. Wuister, D. Vanmaekelbergh, and A. Meijerink, *Single-step synthesis to control the photoluminescence quantum yield and size dispersion of CdSe nanocrystals*, Journal of Physical Chemistry B **107**, 489 (2003).

[17] S. F. Wuister, I. Swart, F. van Driel, S. G. Hickey, and C. de Mello Donegá, *Highly luminescent water-soluble CdTe quantum dots*, Nano Letters **3**, 503 (2003).

[18] P. Reiss, J. Bleuse, and A. Pron, *Highly luminescent CdSe/ZnSe core/shell nanocrystals of low size dispersion*, Nano Letters **2**, 781 (2002).

[19] M. Aven and S. J. Prener, *Physics and Chemistry of II-IV Compounds*, international ed. (North Holland, Amsterdam, The Netherlands, 1967).

[20] S. Fery-Forgues and D. Lavabre, *Are fluorescence quantum yields so tricky to measure? A demonstration using familiar stationery products*, Journal of Chemical Education **76**, 1260 (1999).

[21] T. Karstens and K. Kobs, *Rhodamine B and Rhodamine 101 as reference substances for fluorescence quantum yield measurements*, Journal of Physical Chemistry **84**, 1871 (1980).

[22] S. L. Cumberland, K. M. Hanif, A. Javier, G. A. Khitrov, G. F. Strouse, S. M. Woessner, and C. S. Yun, *Inorganic clusters as single-source precursors for preparation of CdSe, ZnSe, and CdSe/ZnS nanomaterials*, Chemistry of Materials **14**, 1576 (2002).

[23] P. Debye, *Light scattering in soap solutions*, Journal of Colloid Science **3**, 407 (1948).

[24] M. L. Steigerwald, A. P. Alivisatos, J. M. Gibson, T. D. Harris, R. Kortan, A. J. Muller, A. M. Thayer, T. M. Duncan, D. C. Douglass, and L. E. Brus, *Surface derivatization and isolation of semiconductor cluster molecules*, Journal of the American Chemical Society **110**, 3046 (1988).

[25] M. G. Bawendi, A. R. Kortan, M. L. Steigerwald, and L. E. Brus, *X-ray structural characterization of larger CdSe semiconductor clusters*, Journal of Chemical Physics **91**, 7282 (1989).

[26] A. R. Kortan, R. Hull, R. L. Opila, M. G. Bawendi, M. L. Steigerwald, P. J. Carroll, and L. E. Brus, *Nucleation and growth of CdSe on ZnS quantum crystallite seeds, and vice versa, in inverse micelle media*, Journal of the American Chemical Society **112**, 1327 (1990).

[27] N. Herron, Y. Wang, and H. Eckert, *Synthesis and characterization of surface-capped, size-quantized CdS clusters - Chemical control of cluster size*, Journal of the American Chemical Society **112**, 1322 (1990).

[28] C. R. Bullen and P. Mulvaney, *Nucleation and growth kinetics of CdSe nanocrystals in octadecene*, Nano Letters **4**, 2303 (2004).

Chapter 3

Statistical analysis and modelling of time-resolved luminescence from colloidal nanocrystals: interpretation of exponential decays

abstract

The dynamics of optically excited states in emitters are widely studied by recording and modelling luminescence decay curves. Time-resolved spontaneous emission from semiconductor nanocrystals has been measured and modelled with single-, stretched- and multi-exponential functions. A mathematical analysis of the models is presented, and the relation between the concentration of excited emitters and the luminescence decay curve is derived. The proper normalisation and the average decay times for the models are deduced, and a physical interpretation of the decay rate distribution functions for stretched- and multi-exponential models is given. The analysis of the various exponential decay models enabled us to obtain key information on nanocrystal physics from our luminescence decay curves.

3.1 Introduction

Understanding the decay dynamics of excited states in emitters is of key importance for understanding many physical, chemical and biological processes. For example, in Förster resonance energy transfer the influence of acceptor molecules on the decay dynamics of donor molecules is studied to quantify molecular dynamics in biophysics [1]. Atoms [2, 3], dye molecules [4, 5] and nanocrystalline quantum dots [6, 7] are used as light sources in a wide variety of systems. Several groups have studied the influence of the local density of optical modes (LDOS) on the radiative decay rate of atoms and dye molecules in front of a mirror [2–5]. According to Fermi's 'golden rule' the radiative decay rate scales with the LDOS at the location of the emitter. Light sources with a high photoluminescence quantum yield can be used to probe the LDOS. Such lifetime experiments have been widely performed in many different kinds of photonic materials, including metallic films [8, 9], two [10, 11]-, and three-dimensional photonic crystals (Chapter 5).

In photoluminescence lifetime measurements the decay of the number of excited emitters is probed by recording a photoluminescence decay curve. In the case of weak coupling[1], the photoluminescence decay curve (of a two-level system) is single-exponential. Alternative to photoluminescence lifetime measurements, the number of excited emitters can be probed directly by transient absorption measurements [13–15] and non-radiative decay can be recorded with various photothermal techniques [16] (see figure 3.1). Time-correlated-single-photon-counting is generally used to obtain photoluminescence decay curves. The decay curve is built from a histogram which shows the distribution of arrival times of single photons after many excitation-detection cycles. The histogram is modelled with a decay-function from which the decay time of the process is deduced. In the simplest case, when the system is characterised by a single decay rate, the decay curve is described by a single-exponential function. However, in many cases the decay is much more complex [6, 17, 18]. It is a general problem to model these complex multi-exponential decay processes: often the choice of the model is not justified a priori and only accepted on basis of the

[1] In the case of weak exciton-photon coupling the rate of spontaneous emission can be modified by the environment. In the strong coupling case new eigenstates are formed [12].

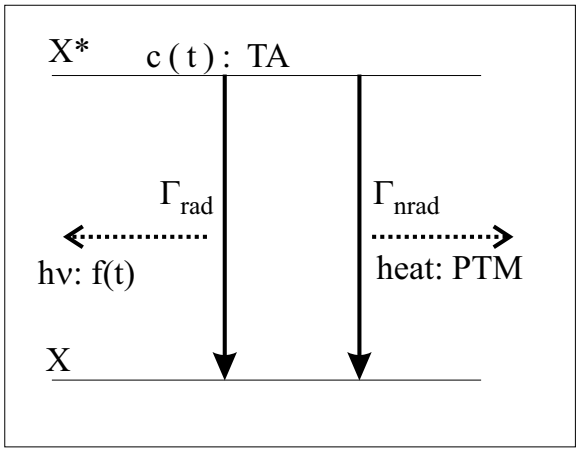

Figure 3.1: *Schematic of the relation between decay of an excited state ($X^* \rightarrow X$) and various experimentally observable parameters. In transient absorption (TA) the time-dependent absorption of the excited state ($c(t)$) is recorded. In photothermal measurements (PTM) the released heat after photoexciation is detected and emission of light is recorded in luminescence decay measurements ($f(t)$).*

fit-quality. Double- and triple-exponential functions or models with a particular distribution of single-exponentials are used [13, 19–22]. Sometimes double- and triple-exponential models can be anticipated [1]. However, in many cases no particular multi-exponential model can be anticipated on the basis of physical knowledge of the studied system.

Besides these multi-exponential models, the stretched-exponential model (Kohlrausch function [23]) is frequently applied. The stretched-exponential function has been applied almost universally to model diffusion processes [24], dielectric relaxation [25], capacitor discharge [26], optical Kerr effect experiments [27] and luminescence decay [28–30]. The physical origin of the apparent stretched-exponential decay in many processes is a source of intense debate [31–33].

In spite of the rich variety of examples where stretched- and multi-exponential models are applied, there is no profound analysis of the models available in the literature. In this Chapter we present a statistical analysis of single-, stretched-, and multi-exponential models and use the analysis to model decay curves from ensembles of CdSe nanocrystals in suspensions and in photonic crystals. First, it is shown how the decay of the fraction of excited emitters is related to the luminescence decay curve. In

contrast to what is stated in many reports, the fraction of excited emitters and the intensity in a luminescence decay measurement are in general not proportional. This observation has important implications in the case of non-single-exponential decay. The proper normalisation and the average lifetime for single-, stretched-, and multi-exponential models are deduced. It will be shown that the recovery of the distribution of decay rates is more complex than generally assumed and the radiative decay weighted distribution of the total decay rates is introduced.

3.2 General remarks

A luminescence decay curve is the probability density of emission and is modelled with a so-called probability density function ($g(t)$) [34]. The decay of the fraction ($\frac{c(t^{'})}{c(0)}$) is described with a reliability function or cumulative distribution function [34]. Here $c(0)$ is the concentration of excited emitters at $t' = 0$ and $c(t^{'})$ is the concentration at time t'. The fraction of excited emitters and the luminescence decay curve, i.e., the reliability function and the probability density function [34], are related as follows:

$$\int_0^{t^{'}} g(t)dt = 1 - \frac{c(t^{'})}{c(0)} \tag{3.1}$$

In many reports the distinction between the reliability function and the probability density function is not made: the intensity of the luminescence decay curve $g(t)$ is taken to be directly proportional to the fraction of excited emitters $\frac{c(t^{'})}{c(0)}$. The fact that the proportionality is not general has important consequences for the interpretation of multi-exponential decay models.

3.2.1 Single exponential decay

It is well known that in the case of first-order chemical kinetics the rate of decrease of the concentration is constant in time:

$$\frac{d\,c(t^{'})}{dt^{'}} = -\Gamma c(t^{'}) \tag{3.2}$$

where $c(t^{'})$ is the concentration of the reactant as a function of time t' and Γ the rate constant of the reaction. As a consequence, the concentration c decreases single-exponentially in time:

$$\frac{c(t^{'})}{c(0)} = \exp(-\Gamma t^{'}) \tag{3.3}$$

The fraction of excited emitters in an ensemble can be described with the same terminology. After excitation the fraction decays with a single characteristic decay time $\tau = \Gamma^{-1}$, called the lifetime. In the simplest case the decay curve is single-exponential, which means that the decay of the excited state is characterised by a single rate constant Γ. Figure 3.2 shows a luminescence decay curve of a dilute suspension of CdSe nanocrystals in chloroform recorded at a wavelength of λ = 650 $\pm 5nm$ (see Chapter 4), with the number of counts on the ordinate and the time on the abscissa. Clearly, the data agree well with single-exponential decay model. This means that all individual nanocrystals that emit light at this particular wavelength do so with the same rate. In Chapter 4 it will be shown that the rate of emission strongly depends on the emission frequency and that it is in agreement with the rate deduced via Fermi's golden rule.

For emitters with a photoluminescence quantum efficiency less than 100 $\%$, the excited state is de-populated by both radiative and non-radiative processes. Γ_{rad} is the radiative decay rate, Γ_{nrad} is the nonradiative decay rate and Γ_{tot} is the total decay rate (Γ_{tot} = Γ_{rad} + Γ_{nrad}). The mathematical expression for the luminescence decay curve can be obtained by inserting eq. 3.3 into eq. 3.1, where Γ is identified with Γ_{tot}, resulting in:

$$g(t) = \Gamma_{rad} \exp(-\Gamma_{tot} t) + \Gamma_{nrad} \exp(-\Gamma_{tot} t) \tag{3.4}$$

In a luminescence decay measurement the recorded signal is proportional to the first term of $g(t)$ only, and will be called $f(t)$:

$$f(t) = \alpha \Gamma_{rad} \exp(-\Gamma_{tot} t) \tag{3.5}$$

and therefore a single-exponential luminescence decay process is modelled with eq. 3.5. The pre-exponential factor α is usually set as adjustable parameter, and is related to several experimental parameters, i.e., the num-

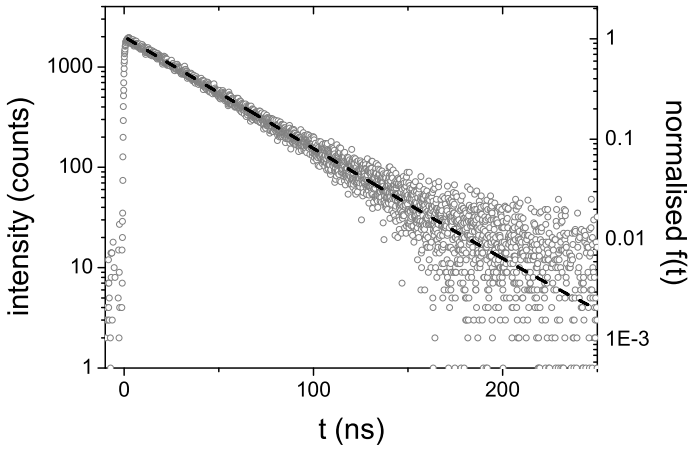

Figure 3.2: *Luminescence decay curve of emission from a dilute suspension of CdSe nanocrystals (grey open dots, left axis). Data were collected at the red side of the emission maximum of the suspension, at* λ *= 650* $\pm 5nm$*. Single-exponential modelling (black dashed curve, right axis) yields a decay time of 39.0* $\pm 2.8ns$ *and a* χ_r^2 *of 1.12. The average photon arrival time* $< t >$*, calculated with eq. 3.7, was 39.1* ns*.*

ber of excitation-emission cycles in the experiment, the photon-collection efficiency and the concentration of the emitter. In the following α will be omitted from our analysis. Comparison of eqs. 3.5 and 3.3 shows that in the case of purely single-exponential decay neglect of the distinction between the reliability function (eq. 3.3) and the probability density function (eq. 3.5) has no important consequences, since both the fraction and the decay curve are single-exponential, and the pre-exponential α factor is usually set as adjustable parameter. Eq. 3.5 is modelled to the data in figure 3.2, with a pre-exponential factor and Γ_{tot} as adjustable parameters. Clearly, our data are well described by a single-exponential decay, as indicated by the quality-of-fit χ_r^2 of 1.12, close to the ideal value of 1.

Eq. 3.5 is a probability density function which means that the probability of emission in a certain time-interval can be deduced by integration. The total probability for emission at all times between $t = 0$ and $t \to \infty$ is given by

$$\int_0^\infty f(t)dt = \int_0^\infty \Gamma_{rad} \exp(-\Gamma_{tot} t)dt = \frac{\Gamma_{rad}}{\Gamma_{tot}} \tag{3.6}$$

which is equal to the luminescence quantum efficiency. The luminescence quantum efficiency is defined as the probability of emission after excitation. The correct recovery of this result in eq. 3.6 shows that eq. 3.5 is properly normalised. The average arrival time of the emitted photon or the average decay time can be calculated by taking the first order moment of eq. 3.5:

$$< t >= \tau_{av} = \frac{\int_0^\infty f(t)tdt}{\int_0^\infty f(t)dt} = \frac{1}{\Gamma_{tot}} \tag{3.7}$$

which shows that the average decay rate is equal to the inverse of the total decay rate and is thus determined by both radiative and non-radiative decay processes.

Only in the case of single-exponential decay is $< t >$ equal to $\frac{1}{\Gamma_{tot}}$. The average arrival time $< t >$ can be calculated with a spreadsheet program and no modelling is required. However, this average time can only be calculated when the complete decay curve is recorded, i.e., when the tail of the decay curve reaches the noise-level. The average arrival time for the data in figure 3.2 was $< t >= 39.1$ ns, very close to the value of 39.0 $\pm 2.8ns$ deduced from single-exponential modelling, which further confirms the single-exponential character of the decay curve.

3.2.2 Stretched exponential decay

In contrast to the example shown in figure 3.2, there are many cases in which decay curves cannot be modelled with a single-exponential function. This usually means the decay is characterised by a distribution of rates instead of a single rate[2]. Figure 3.4 shows a strongly non-single-exponential decay curve of spontaneous emission from CdSe nanocrystals in an inverse opal photonic crystal (see Chapter 5). It is a general problem to describe these relaxation processes which do not follow a simple single-exponential decay. Models with many adjustable parameters will fit the experimental data but lack a physical basis. When only a few adjustable parameters are used it is frequently difficult to find an adequate model. To strike a balance between the number of adjustable parameters and the quality of the

[2]In the case of van Hove singularities the luminescence decay curve of a single emitter can be non-single-exponential.

modelling a stretched exponential decay model [23] is widely applied:

$$\frac{c(t^{'})}{c(0)} = \exp(-\Gamma_{str}t^{'})^{\beta} \tag{3.8}$$

where β is the stretch parameter, which varies between 0 and 1, and Γ_{str} the total decay rate in the case of stretched exponential decay. The stretch parameter β expresses the underlying distribution of rates: a small β means that the distribution of rates is broad and β close to 1 implies a narrow distribution. The recovery of the distribution of rates in the case of stretched exponential decay is mathematically complicated [20, 25, 31, 32].

The luminescence decay curve corresponding to a stretched exponential decay of the fraction $\frac{c(t^{'})}{c(0)}$ can be deduced using eq. 3.8 and eq. 3.1, and results in:

$$g(t) = \frac{\beta}{t}(\Gamma_{str}t)^{\beta}\exp(-\Gamma_{str}t)^{\beta} \tag{3.9}$$

The normalisation of eq. 3.9 can be deduced by integration for all times between $t = 0$ and $t \to \infty$, which yields 1. This result means that eq. 3.9 is correctly normalised *only* for emitters with a quantum yield of 1 ($\Gamma_{rad} = \Gamma_{tot}$). It is not clear how normalisation should be accounted for in other cases, i.e., quantum yield $< 100\%$. To the best of our knowledge, this problem has been overlooked in the literature.

In contrast to the previous case of single-exponential decay, the reliability function and the probability density function of a stretched exponential do *not* have the same form; the probability density function contains a time-dependent pre-factor. Therefore, application of eq. 3.1 has important consequences. As an illustration, in figure 3.3 a stretched exponential decay function (eq. 3.8) and the corresponding luminescence decay curve (eq. 3.9) are plotted for the example Γ_{str}=1 and β=0.5. It is clear that both curves are quite different. For a β-value of 0.5 the average decay time of the reliability function (eq. 3.8) and the probability density function (eq. 3.9) differ by more than a factor of ten and thus it is important to take into consideration whether eq. 3.8 or eq. 3.9 is used to describe the experimental photoluminescence decay curve. In many reports [28–30, 33, 35, 36], the stretched exponential function that describes the fraction of excited emitters is used to model the luminescence decay curve. We argue that using a stretched exponential for the fraction $\frac{c(t^{'})}{c(0)}$ implies that the proper proba-

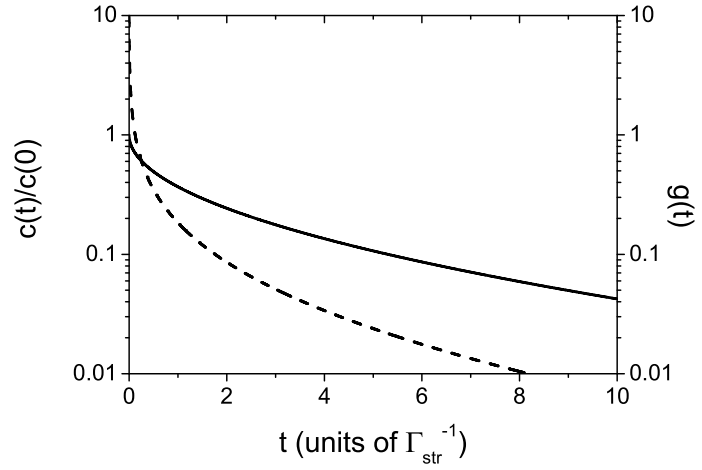

Figure 3.3: *Plot of stretched exponential decay of the fraction $\frac{c(t)}{c(0)}$ (eq. 3.8, black curve, left axis) and the corresponding luminescence decay curve $g(t)$ (eq. 3.9, black dashed curve, right axis). We have taken Γ_{str}=1 and β=0.5. The curves that describe the fraction of excited emitters and the corresponding luminescence decay curve are quite different.*

bility density function, i.e., eq. 3.9, must be used to model a luminescence decay curve. In figure 3.4(a) modelling with eq. 3.9, with Γ_{str} and β as adjustable parameters, is shown. The β-value was 0.42 and Γ_{str} was 96.2 μs^{-1} ($\frac{1}{\Gamma_{str}} = 10.4\ ns$). Modelling with stretched exponential is obviously more satisfactory than single-exponential, but fails at long times as reflected by the high χ^2_r-value of 60.7.

The main advantage of modelling with a stretched-exponential function is that the average decay time $< t >$ can readily be calculated. In parallel with eq. 3.7, the average decay time can be deduced [25]:

$$< t >= \tau_{av} = \frac{\int_0^\infty g(t)tdt}{\int_0^\infty g(t)dt} = \frac{1}{\Gamma_{str}\beta} Gamma[\frac{1}{\beta}] \tag{3.10}$$

where $Gamma$ is the $Gamma$-function. For the single-exponential limit of $\beta \rightarrow 1$ eq. 3.10 reduces to eq. 3.7. Eq. 3.10 yielded an average decay time of 31.1 ns for the data in figure 3.4.

In the case of the stretched exponential model the distribution of the

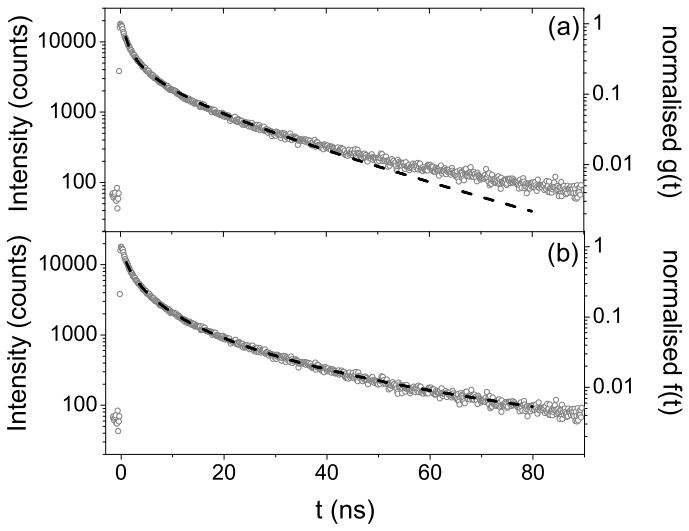

Figure 3.4: *Luminescence decay curve of emission from CdSe nanocrystals in titania inverse opal (dots, left axis). The lattice parameter of the titania inverse opal was 340 nm and the emission wavelength λ=595 nm. (a) Stretched-exponential modelling (black dashed curve, right axis) yields Γ_{str}=96.2 μs^{-1} ($\frac{1}{\Gamma_{str}}$=10.4 ns), an average decay time $< t >$ of 31.1 ns, and a β-value of 0.42. This model does not fit the data ($\chi_r^2 = 60.7$). (b) Modelling with a log-normal distribution of rates (eq. 3.21 and 3.22, black dashed curve, right axis) is plotted. The χ_r^2 is 1.17, Γ_{mf} is 91.7 μs^{-1} ($\frac{1}{\Gamma_{mf}} = 10.9\ ns$) and the width of the distribution $\Delta\Gamma$ is 0.57 ns^{-1}.*

rates is unknown and is generally deduced by solving the following equation [19, 28, 35–37]:

$$\frac{\beta}{t}(\Gamma t)^{\beta}\exp(-\Gamma t)^{\beta} = \int_0^{\infty}\sigma(\Gamma)\exp(-\Gamma t)d\Gamma \tag{3.11}$$

where $\sigma(\Gamma)$ is the distribution function. To deduce $\sigma(\Gamma)$ an inverse Laplace transform is applied. For $\beta \neq 0.5$ and $\beta \neq 1$ there is no analytical solution of eq. 3.11 and for this reason it is difficult to deduce the distribution function [20, 25, 32]. This difficulty can be circumvented by modelling directly with a known distribution function, as will be shown below. It is generally assumed that $\sigma(\Gamma)$ derived in this way expresses the distribution of the total decay rate. However, we show below that this is not the case and we will give a complete physical interpretation of $\sigma(\Gamma)$.

3.2.3 Decay rate distributions

In the case of multi-exponential decay, the photoluminescence decay curve is modelled by a sum of single-exponentials. The decay curve has the following form:

$$f(t) = \frac{1}{c(0)} \sum_{i=1}^{n} c_i \Gamma_{rad,i} \exp(-\Gamma_{tot,i} t) \tag{3.12}$$

where n is the number of different emitters or the number of different environments, c_i is the fraction of emitters that has a radiative decay rate $\Gamma_{rad,i}$ and $c(0)$ is the concentration of excited emitters at $t = 0$, i.e., the sum of all fractions. Sums of two or three exponentials are frequently applied [1]. When the different fractions (or environments) are continuously distributed in a particular way a distribution function ($\rho(\Gamma)$) may be used. Such a function describes the distribution density (or concentration) of the emitters over the emission decay rates at time $t = 0$. For example, the fraction of emitters with a total decay rate between $\Gamma_{tot,1}$ and $\Gamma_{tot,2}$ is

$$\frac{c(\Gamma_{tot,1}, \Gamma_{tot,2})}{c(0)} = \frac{1}{c(0)} \sum_{\Gamma_{tot,1}}^{\Gamma_{tot,2}} c(\Gamma_{tot,i}) = \int_{\Gamma_{tot,1}}^{\Gamma_{tot,2}} \rho(\Gamma_{tot}) d\Gamma_{tot} \tag{3.13}$$

where $\rho(\Gamma_{tot})$ expresses the distribution of the various components over the rates and Γ_{tot} is the total decay rate. The distribution function is normalised, i.e., the sum of all fractions is 1:

$$\int_0^\infty \rho(\Gamma_{tot}) d\Gamma_{tot} = 1 \tag{3.14}$$

Taking a distribution function into account, the decay curve has the following mathematical form:

$$f(t) = \sum_{i=1}^{n} \Delta\Gamma_{tot} \rho(\Gamma_{tot,i}) \Gamma_{rad,i} \exp(-\Gamma_{tot,i} t) \tag{3.15}$$

where $\rho(\Gamma_{tot,i})$ is the distribution function with units s and $\Delta\Gamma_{tot}$ the bandwidth. The bandwidth is the separation between the various components of the sum. In eq. 3.15 each component in the sum is correctly normalised since each component is multiplied by its radiative decay rate $\Gamma_{rad,i}$. For

very small values of $\Delta\Gamma_{tot}$, eq. 3.15 can be written as an integral:

$$f(t) = \int_0^\infty \rho(\Gamma_{tot})\Gamma_{rad}(\Gamma_{tot}) \exp(-\Gamma_{tot}t) d\Gamma_{tot} \tag{3.16}$$

where $\rho(\Gamma_{tot})$ is the distribution of Γ_{tot}, and $\Gamma_{rad}(\Gamma_{tot})$ is Γ_{rad} corresponding to a particular value of Γ_{tot}. The average decay time is, similar to eq. 3.7, now defined as follows:

$$< t >= \int_0^\infty \rho(\Gamma_{tot}) \frac{1}{\Gamma_{tot}} \, d\Gamma_{tot} \tag{3.17}$$

In the case of single-exponential decay the distribution function is strongly peaked around a central Γ_{tot}-value, i.e., the distribution function is a Dirac delta function. Inserting a Dirac delta function into eq. 3.16 recovers eq. 3.5:

$$\begin{aligned} f(t) &= \int_0^\infty \delta(\Gamma_{tot} - \Gamma_{tot'})\Gamma_{rad} \exp(-\Gamma_{tot}t) d\Gamma_{tot} \\ &= \Gamma_{rad} \exp(-\Gamma_{tot'}t) \end{aligned} \tag{3.18}$$

and inserting the delta function into eq. 3.17, yields eq. 3.7. This confirms that the generalisation to eqs. 3.16 and 3.17 is correct since it yields the correctly normalised single-exponential functions.

In eq. 3.16 it is assumed that for each Γ_{tot} there is one Γ_{rad}: the function $\Gamma_{rad}(\Gamma_{tot})$ relates each Γ_{tot} to exactly one Γ_{rad}. In general both Γ_{tot} and Γ_{rad} vary independently and as a consequence eq. 3.16 is rewritten to

$$f(t) = \int_0^\infty d\Gamma_{tot} \exp(-\Gamma_{tot}t)\rho(\Gamma_{tot}) \int_0^{\Gamma_{tot}} d\Gamma_{rad}\rho_{\Gamma_{tot}}(\Gamma_{rad})\Gamma_{rad} \tag{3.19}$$

where $\rho_{\Gamma_{tot}}(\Gamma_{rad})$ is the normalised distribution of Γ_{rad} at constant Γ_{tot}. For each Γ_{tot} the integration is performed over all radiative rates; a distribution of Γ_{rad} is taken into account for each Γ_{tot}. Such a situation appears, for example, in a photonic crystal. In photonic crystals the local density of optical states (LDOS) varies with the location in the crystal [38]. Therefore, a distribution of emitters can, at a certain frequency and with a certain Γ_{tot}, emit light with a distribution of radiative rates.

Eq. 3.19 is the most general expression of a luminescence decay curve; from this function every decay curve with a particular distribution of rates

can be recovered. For this reason it is instructive to compare eq. 3.19 with other models. Eq. 3.18 shows that the single exponential model is recovered for a delta-shape distribution function. Below we will compare eq. 3.19 with other models.

Modelling directly with a distribution of decay rates, instead of modelling with a Laplace transform as in the case of a stretched exponential, is widely applied [19, 21, 22, 33, 37]. An advantage of modelling directly with a decay rate distribution is that the distribution function is known and therefore direct physical information is available. This way of modelling is a big advantage over modelling with a stretched exponential function, where it is complicated to get the distribution of decay rates from the β-value. In all cases a function of the following form is used:

$$f(t) = \int_0^\infty \sigma(\Gamma) \exp(-\Gamma t) d\Gamma \tag{3.20}$$

Note that this equation differs from eq. 3.19: in eq. 3.20 the various components are not separately normalised as in eq. 3.19. Distribution functions that can be used for $\sigma(\Gamma)$ are normal and sum of normal distributions, Lorentzian, sum of Lorentzians and log-normal distribution functions. Modelling is now performed with an infinite series of single-exponentials which are expressed with only a few free parameters. In some cases it can be anticipated that a continuous distribution is justified on the basis of physical arguments. The form of the distribution usually cannot be predicted and a decision is made on basis of quality-of-fit. A good fit only indicates a certain distribution, but does not prove that it is unique. In figure 3.4(b) the luminescence decay curve is modelled with eq. 3.20, with a log-normal distribution of the rate Γ:

$$\sigma(\Gamma) = A \exp\left[-(\frac{\ln\Gamma - \ln\Gamma_{mf}}{\gamma})^2\right] \tag{3.21}$$

where A is the normalisation constant, Γ_{mf} is the most frequent rate constant. A log-normal distribution fuction is plotted in figure 3.5. γ is related to the width of the distribution:

$$\Delta\Gamma = 2\Gamma_{mf} \sinh(\gamma) \tag{3.22}$$

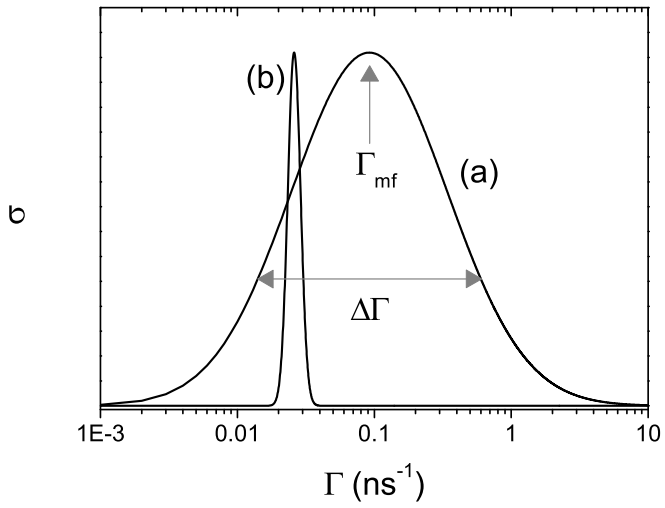

Figure 3.5: *Log-normal distribution of* Γ*. This distribution was modelled to the data of figure 3.4 (curve a) and figure 3.2 (curve b), with* Γ_{mf} *and* $\Delta\Gamma$ *as adjustable parameters. For (a)* Γ_{mf} *is 91.7* μs^{-1} *(*$\frac{1}{\Gamma_{mf}} = 10.9\ ns$*) and the width of the distribution* $\Delta\Gamma$ *was 0.57* ns^{-1} *and for (b)* Γ_{mf} *was 25.8* μs^{-1} *(*$\frac{1}{\Gamma_{mf}} = 38.8\ ns$*) and the width of the distribution* $\Delta\Gamma$ *was 0.079* ns^{-1}*.*

where $\Delta\Gamma$ is equal to the width of the distribution at $\frac{1}{e}$, as indicated in figure 3.5. The most frequent rate constant and γ were adjustable parameters, only one extra adjustable parameter compared to a single-exponential model. Clearly, this model (eq. 3.20 and 3.21) describes our multi-exponential experimental data extremely well. The χ_r^2 was 1.17, Γ_{mf} was 91.7 μs^{-1} ($\frac{1}{\Gamma_{mf}} = 10.9\ ns$) and the width of the distribution $\Delta\Gamma$ was 0.57 ns^{-1}. The $\frac{1}{\Gamma_{mf}}$-value of 10.9 ns is close to the $\frac{1}{\Gamma_{str}}$-value of 10.4 ns. Both values were obtained by modelling two different functions to the same data. Where modelling with a log-normal distribution of decay rates yields direct and clear physical parameters, i.e., the shape and width of the decay rate distribution, stretched exponential modelling only results in a stretch-parameter which lacks a clear and direct physical interpretation. The log-normal function is plotted in figure 3.5 (curve a). The broad distribution of rates demonstrates the strongly non-single-exponential character of the decay curve. In Chapter 5 it will be shown that this broad distribution is related to the

spatial variation of the LDOS in inverse-opal photonic crystals. The same log-normal model was fitted to the data of figure 3.2 and yielded a Γ_{mf} of 25.8 μs^{-1} ($\frac{1}{\Gamma_{mf}} = 38.8\ ns$), which is close to the lifetime deduced from the single-exponential modelling of 39.0 $\pm 2.8 ns$. The width of the distribution $\Delta\Gamma$ was 0.079 ns^{-1}. The distribution is plotted in figure 3.5 (curve b) and is narrow, which reveals the single-exponential character of the decay curve.

It is widely assumed that $\sigma(\Gamma)$ is equal to the distribution of total rates [19, 21, 22, 35, 36]. Comparison with eq. 3.19 shows that this is not true. $\sigma(\Gamma)$ contains information about both the radiative and non-radiative rate:

$$\sigma(\Gamma) = \rho(\Gamma_{tot}) \int_0^{\Gamma_{tot}} \rho(\Gamma_{rad}) \Gamma_{rad} d\Gamma_{rad} \tag{3.23}$$

and therefore we will call $\sigma(\Gamma)$ the radiative decay weighted distribution over the decay rate. Only in cases where the non-radiative rate is distributed and the radiative rate is constant [39], i.e., $\rho(\Gamma_{rad})$ is a delta-function, $\sigma(\Gamma)$ directly gives the relative distribution of Γ_{tot}. Thus, in order to find the distribution of the total decay rates from the luminescence decay curve, additional knowledge of the relation between Γ_{tot} and Γ_{rad} is required.

3.3 Conclusion

In this Chapter an analysis of single-, stretched- and multi-exponential models is presented which are used to describe luminescence decay curves. Proper normalisation is deduced for single- and multi-exponential models and the average decay time is deduced for all three models. Mathematical expressions are given, relating the fraction of excited emitters to the luminescence decay curve. It is shown that in the case of the stretched-exponential model the decay of the fraction and the luminescence decay curve are strongly dissimilar. Furthermore, the analysis revealed that the stretched exponential model lacks clear statistical interpretation. On the other hand, models which have a particular distribution of decay rates yield direct physical information. Our luminescence decay curves were modelled with a log-normal distribution of decay rates. The radiative decay weighted distribution of the decay rate was introduced, which is the

distribution that is deduced from luminescence decay curves. The analysis of the various exponential decay models enabled us to extract key information from our luminescence decay curves, as applied in Chapters 4 and 5.

References

[1] J. R. Lakowicz, *Principles of Fluorescence Spectroscopy*, 2nd ed. (Kluwer Academic/Plenum Publishers, New York, 1999).

[2] K. H. Drexhage, *Influence of a dielectric interface on fluorescence decay time*, Journal of Luminescence **1,2**, 693 (1970).

[3] R. M. Amos and W. L. Barnes, *Modification of the spontaneous emission rate of Eu3+ ions close to a thin metal mirror*, Physical Review B **55**, 7249 (1997).

[4] N. Danz, J. Heber, and A. Brauer, *Fluorescence lifetimes of molecular dye ensembles near interfaces*, Physical Review A **66**, 063809 (2002).

[5] S. Astilean and W. L. Barnes, *Quantum efficiency and the photonic control of molecular fluorescence in the solid state*, Applied Physics B-Lasers and Optics **75**, 591 (2002).

[6] S. A. Crooker, J. A. Hollingsworth, S. Tretiak, and V. I. Klimov, *Spectrally resolved dynamics of energy transfer in quantum-dot assemblies: Towards engineered energy flows in artificial materials*, Physical Review Letters **89**, 186802 (2002).

[7] I. L. Medintz, H. T. Uyeda, E. R. Goldman, and H. Mattoussi, *Quantum dot bioconjugates for imaging, labelling and sensing*, Nature Materials **4**, 435 (2005).

[8] J. S. Biteen, D. Pacifici, N. S. Lewis, and H. A. Atwater, *Enhanced radiative emission rate and quantum efficiency in coupled silicon nanocrystal-nanostructured gold emitters*, Nano Letters **5**, 1768 (2005).

[9] J. H. Song, T. Atay, S. F. Shi, H. Urabe, and A. V. Nurmikko, *Large enhancement of fluorescence efficiency from CdSe/ZnS quantum dots induced by resonant coupling to spatially controlled surface plasmons*, Nano Letters **5**, 1557 (2005).

[10] M. Fujita, S. Takahashi, Y. Tanaka, T. Asano, and S. Noda, *Simultaneous inhibition and redistribution of spontaneous light emission in photonic crystals*, Science **308**, 1296 (2005).

[11] A. Kress, F. Hofbauer, N. Reinelt, M. Kaniber, H. J. Krenner, R. Meyer, G. Bohm, and J. J. Finley, *Manipulation of the spontaneous emission dynamics of quantum dots in two-dimensional photonic crystals*, Physical Review B **71**, 241304 (2005).

[12] R. Loudon, *The Quantum Theory of Light*, 3rd ed. (Oxford University Press Inc., Oxford, 2001).

[13] P. Foggi, L. Pettini, I. Santa, R. Righini, and S. Califano, *Transient absorption and vibrational-relaxation dynamics of the lowest excited singlet-state of pyrene in solution*, Journal of Physical Chemistry **99**, 7439 (1995).

[14] V. I. Klimov and D. W. McBranch, *Femtosecond 1P-to-1S electron relaxation in strongly confined semiconductor nanocrystals*, Physical Review Letters **80**, 4028 (1998).

[15] F. V. R. Neuwahl, P. Foggi, and R. G. Brown, *Sub-picosecond and picosecond dynamics in the S-1 state of 2,2 ′-bipyridyl -3,3 ′-diol investigated by UV-visible transient absorption spectroscopy*, Chemical Physics Letters **319**, 157 (2000).

[16] A. Rosencwaig, *Photoacoustics and Photoacoustic Spectroscopy* (John Wiley & Sons, New York, 1980).

[17] S. F. Wuister, A. van Houselt, C. D. M. Donega, D. Vanmaekelbergh, and A. Meijerink, *Temperature antiquenching of the luminescence from capped CdSe quantum dots*, Angewandte Chemie-International Edition **43**, 3029 (2004).

[18] P. Lodahl, A. F. van Driel, I. S. Nikolaev, A. Irman, K. Overgaag, D. Vanmaekelbergh, and W. L. Vos, *Controlling the dynamics of spontaneous emission from quantum dots by photonic crystals*, Nature **430**, 654 (2004).

[19] D. R. James and W. R. Ware, *Recovery of underlying distributions of lifetimes from fluorescence decay data*, Chemical Physics Letters **126**, 7 (1986).

[20] A. Siemiarczuk, B. D. Wagner, and W. R. Ware, *Comparison of the maximum-entropy and exponential series methods for the recovery of distributions of lifetimes from fluorescence lifetime data*, Journal of Physical Chemistry **94**, 1661 (1990).

[21] J. C. Brochon, A. K. Livesey, J. Pouget, and B. Valeur, *Data-analysis in frequency-domain fluorometry by the maximum-entropy method - Recovery of fluorescence lifetime distributions*, Chemical Physics Letters **174**, 517 (1990).

[22] J. Wlodarczyk and B. Kierdaszuk, *Interpretation of fluorescence decays using a power-like model*, Biophysical Journal **85**, 589 (2003).

[23] R. Kohlrausch, *Theorie des elektrischen rückstandes in der leidener flasche*, Annalen der Physik (Poggendorff) **91**, 179 (1854).

[24] L. A. Deschenes and D. A. Vanden Bout, *Single-molecule studies of heterogeneous dynamics in polymer melts near the class transition*, Science **292**, 255 (2001).

[25] C. P. Lindsey and G. D. Patterson, *Detailed comparison of the Williams-Watts and Cole-Davidson functions*, Journal of Chemical Physics **73**, 3348 (1980).

[26] R. Kohlrausch, *Theorie des elektrischen rückstandes in der leidener flasche*, Annalen der Physik (Poggendorff) **91**, 56 (1854).

[27] R. Torre, P. Bartolini, and R. Righini, *Structural relaxation in supercooled water by time-resolved spectroscopy*, Nature **428**, 296 (2004).

[28] G. Schlegel, J. Bohnenberger, I. Potapova, and A. Mews, *Fluorescence decay time of single semiconductor nanocrystals*, Physical Review Letters **88**, 137401 (2002).

[29] R. Chen, *Apparent stretched-exponential luminescence decay in crystalline solids*, Journal of Luminescence **102**, 510 (2003).

[30] B. R. Fisher, H. J. Eisler, N. E. Stott, and M. G. Bawendi, *Emission intensity dependence and single-exponential behavior in single colloidal quantum dot fluorescence lifetimes*, Journal of Physical Chemistry B **108**, 143 (2004).

[31] D. L. Huber, *Statistical model for stretched exponential relaxation in macroscopic sytems*, Physical Review B **31**, 6070 (1985).

[32] F. Alvarez, A. Alegria, and J. Colmenero, *Relationship between the time-domain Kohlrausch-Williams-Watts and frequency-domain Havriliak-Negami relaxation functions*, Physical Review B **44**, 7306 (1991).

[33] M. Lee, J. Kim, J. Tang, and R. M. Hochstrasser, *Fluorescence quenching and lifetime distributions of single molecules on glass surfaces*, Chemical Physics Letters **359**, 412 (2002).

[34] E. R. Dougherty, *Probability and Statistics for the Engineering, Computing and Physical Sciences* (Prentice-Hall International Inc., Englewood, New Jersey, 1990).

[35] K. C. Benny Lee, J. Siegel, S. E. D. Webb, S. Leveque-Fort, M. J. Cole, R. Jones, K. Dowling, M. J. Lever, and P. M. W. French, *Application of the stretched exponential function to fluorescence lifetime imaging*, Biophysical Journal **81**, 1265 (2001).

[36] M. N. Berberan-Santos, E. N. Bodunov, and B. Valeur, *Mathematical functions for the analysis of luminescence decays with underlying distributions 1. Kohlrausch decay function (stretched exponential)*, Chemical Physics **315**, 171 (2005).

[37] D. R. James, Y.-S. Liu, P. De Mayo, and W. R. Ware, *Distribution of fluorescence lifetimes. Consequences for the photophysics of molecules adsorbed on surfaces.*, Chemical Physics Letters **120**, 460 (1985).

[38] R. Sprik, B. A. van Tiggelen, and A. Lagendijk, *Optical emission in periodic dielectrics*, Europhysics Letters **35**, 265 (1996).

[39] P. Vergeer, T. J. H. Vlugt, M. H. F. Kox, M. I. den Hertog, J. P. J. M. van der Eerden, and A. Meijerink, *Quantum cutting by cooperative energy transfer in* $Yb_xY_{1-x}PO_4$*:*Tb^{3+}, Physical Review B **71**, 014119 (2005).

Chapter 4

Frequency-dependent rate of spontaneous emission from CdSe and CdTe nanocrystals: influence of dark states

abstract

We have studied the rate of spontaneous emission from colloidal CdSe and CdTe nanocrystals at room temperature. The decay rate, obtained from luminescence decay curves, increases with the emission frequency in a supra-linear way. This dependence is explained by the thermal occupation of dark exciton states at room temperature, giving rise to a strong attenuation of the rate of emission. Three other effects which could explain a similar dependence were carefully excluded, namely Förster energy transfer between the nanocrystals, re-absorption and defect-related luminescence. We present a simple analytical theory which takes into account thermal population over the various exciton states and calculate a size-dependent decay rate. Furthermore, we present tight-binding calculations of the decay rate. Both theoretical approaches, the simple analytical theory and the tight-binding calculations, are in good agreement with experiments.

4.1 Introduction

Due to quantum confinement, nanocrystals possess discrete electron and hole energy levels [1, 2]. As a consequence, optical absorption occurs at discrete energies which are determined by the size and the shape of the nanocrystal host [3]. At low excitation density, light emission is due to decay of the lowest bright exciton state to the ground state. The energy of emission decreases with increasing crystal-size. The possibility of tailoring the exciton emission energy by the nanocrystal size has led to a world-wide interest in light-emitting semiconductor nanocrystals. It is an open question how the size and the emission frequency of a semiconductor nanocrystal control the spontaneous emission decay rate of the exciton. Such a study is currently feasible due to the availability of colloidal nanocrystal suspensions with a high quality (see Chapter 2 and Refs. [4–9]). These suspensions form a unique model system to probe the frequency dependence in Fermi's golden rule; the emission frequency can be tuned via the crystal size without changing the chemistry. A linear increase with frequency of the rate of spontaneous emission is expected for an ideal two-level exciton system ($\Gamma \propto \omega$) [3, 10] or a cubic relation for an ideal two-level atom ($\Gamma \propto \omega^3$) [11]. In contrast, a frequency-independent rate of spontaneous emission for spherical CdSe nanocrystals is observed in experiments by Crooker et al. [12].

Understanding exciton dynamics in nanocrystals is important, not only for purely scientific reasons; semiconductor nanocrystals have a huge potential for application as monochromatic light sources in biological research [13, 14] and in opto-electrical devices [15–17]. The rate of spontaneous emission determines the statistics of the output of a single photon source [15], the light-intensity of incoherent sources consisting of nanocrystal assemblies such as light emitting diodes [16], and the output of coherent sources such as lasers [17]. In addition, the high luminescence efficiency combined with a narrow homogeneous linewidth make nanocrystals ideal probes in photonic studies [15, 18].

Experimental data on the size-dependent strength of the optical transitions are limited. The extinction coefficient has been studied for several nanocrystal suspensions [19–23]. However, the data are not sufficient to show how the strength of the transitions, i.e., the dipolar matrix element,

depends on the size of the nanocrystal. Direct determination of the radiative lifetime from luminescence decay curves has proved troublesome due to the fact that the decay curves are influenced by both non-radiative and radiative recombination. In addition, decay curves are often multi-exponential, which means that not all the nanocrystals have the same decay rate [24] or that the decay rate varies in time [25].

In this Chapter, we report on the frequency-dependent decay rate of excitons in colloidal CdSe and CdTe nanocrystals at room temperature. We observe that the luminescence decay curves are very close to single-exponential. For both CdSe and CdTe nanocrystals, the decay rate increases with the emission frequency in a supra-linear way, in contrast to the linear relation expected for an ideal two-level exciton system or the cubic relation for an ideal two-level atom. From complementary calculations based on a simple analytical theory and on tight-binding theory[1], we conclude that the supra-linear increase is caused by thermal population of various hole states with low transition probability, i.e., dark states, that lie close to the ground state. The comparison between theory and experiment highlights the importance of excitation storage in dark excitonic states.

4.2 Experimental

4.2.1 CdTe nanocrystals

The synthesis of CdTe nanocrystals was performed in an argon-purged glovebox with an oxygen and water content less than 2 ppm. In a three-necked flask 10 g of dry dodecylamine (DDA) and 7 mL of trioctylphosphine (TOP) were heated to 50°C. To the solution of DDA and TOP were added 0.22 g (1.5×10^{-3} mol) dimethyl cadmium ($Cd(Me)_2$) in 7 mL of TOP and 0.16 g (1.3×10^{-3} mol) Te powder. A Cd/Te ratio of about 1.25 was used in all the syntheses performed. The reaction mixture was slowly heated ($\sim$1.5°C/min) until the final temperature was reached. Syntheses were performed with final temperatures of 145°C, 165°C and 180°C. The capping of the raw product of the synthesis (DDA) was subsequently replaced by a thiol-capping. To this end 150 μl of the raw product was dispersed in 5 ml

[1]The tight-binding calculations and the analytical theory were devloped by G. Allan and C. Delerue (IEMN, Département ISEN, Lille, France)

chloroform. To this suspension of nanocrystals in chloroform 200 μl of hexanethiol in chloroform (1 mol/l) was added. After addition of hexanethiol, suspensions were used in optical measurements, without further processing.

4.2.2 ZnSe[CdSe] nanocrystals

The synthesis was performed in an argon-purged glovebox with an oxygen and water content less than 2 ppm. The coordinating solvent consisted of 15 g hexadecylamine (HDA) and 15 g trioctylphosphine oxide (TOPO). To the coordinating solvent 2 ml of anhydrous triethylorthoformate (TEOF) was added and the solution was heated and stirred. After heating for 30 min at 220°C the solution temperature was increased to 330°C. During the final heating step the colour of the coordinating solvent turned from colourless to 'goldish'. Meanwhile, a solution was prepared containing 0.28 g (2.0×10^{-3} mol) $Cd(Me)_2$, 0.8 g (1.0×10^{-2} mol) Se and 10 ml TOP. The heating mantle was removed and at 300°C the solution with Cd- and Se- precursors in TOP was quickly injected into the coordinating solvent. The temperature of the mixture was allowed to drop to 170°C, after which the heater was replaced. The temperature was then increased and left for approximately 2 hours at 240 °C. After annealing at 240 °C, a solution of 0.8 g Se, 0.28 g $Cd(Me)_2$ in 10 ml TOP was added drop-wise (10 ml/hour). At the end, half of the mixture was removed. To grow a ZnSe shell around the CdSe nanocrystals, a method based on Ref. [6] was applied. To the remaining half of the mixture a solution containing 1.5 g zinc stearate ($Zn(C_{18}H_{35}O_2)_2$) and 10 ml toluene was added drop-wise (10 ml/hour) at 190°C.

4.2.3 Characterisation

Absorption spectra were recorded with a Perkin-Elmer Lambda 16 UV/VIS spectrometer. The optical density at the first absorption peak of the characterised nanocrystal suspensions was smaller than 0.05. This means that the suspensions are sufficiently diluted that energy-transfer between the nanocrystals can be excluded. A suspension of nanocrystals contains a collection of differently sized particles, distributed around a certain average size. The photoluminescence of such a suspension is inhomogeneously

broadened [26, 27]. For this reason, the size-dependent decay rate can be probed by measurements at various frequencies in the emission band of the suspension.

Luminescence decay curves were obtained by binning the arrival times of the single photons excited with a Pico Quant picosecond laser (λ_{ex}=406 nm) and detected with a fast Hamamatsu photomultiplier tube. A monochromator with a focal length 0.1 m and a grating with 1350 lines/mm blazed at 500 nm was placed before the detector. The spectral resolution of the monochromator was <10 nm. Pulse height analysis was done with a Time Harp 100 computer card. The repetition rate of the laser was 2.5 MHz.

4.2.4 Data analysis

The decay curves were analysed with three methods. First, the raw data were fitted with a single-exponential model, with the decay rate, the pre-exponential factor and the background as adjustable parameter. Secondly, the average photon arrival time was calculated. For this, eq. 3.7 was converted from an integral form to a discrete form:

$$< t >= \tau_{av} = \frac{\sum_{bins} f(t)t}{\sum_{bins} f(t)} \tag{4.1}$$

where t is the time and $f(t)$ the background corrected luminescence decay curve. The summation was calculated over all time bins, i.e., from the maximum intensity bin to the bin with the noise level, and was performed with a spreadsheet program. Thirdly, the decay time and the β-value were deduced from stretched-exponential modelling

$$f(t) = \frac{\beta}{t}(\Gamma_{str}t)^{\beta}\exp(-\Gamma_{str}t)^{\beta} \tag{4.2}$$

where β is the stretch parameter, which varies between 0 and 1, and Γ_{str} the total decay rate in the case of stretched exponential decay. The stretch parameter β expresses the underlying distribution of rates; a small β-value means that the distribution of rates is broad.

Table Curve 2D version 5.0 was used to model decay curves. The decay curves were modelled directly, over the full time range of 400 ns, with the background as a fit parameter.

4.3 Theory

4.3.1 Analytical theory

The rate of a spontaneous transition from an excited electron-hole state $|j\rangle$ to the ground state $|0\rangle$ can be derived from Fermi's 'golden rule' [3, 11] (eq. 1.13)

$$\Gamma_j = \frac{ne^2F^2}{3\pi\epsilon_0 m^2\hbar c^3}\omega_j|\langle 0|\mathbf{p}|j\rangle|^2 \tag{4.3}$$

where e is the electron charge, n the refractive index of the surrounding medium, ϵ_0 the permittivity of free space, m the electron rest mass, c the speed of light, $\hbar$ Planck's constant divided by 2π, ω_j is the frequency of the emitted light, and $\langle 0|\mathbf{p}|j\rangle$ is the matrix element of the momentum operator $\mathbf{p}$ that is related to the dipolar matrix element by $\langle 0|\mathbf{p}|j\rangle = im\omega_j\langle 0|\mathbf{r}|j\rangle$ [10]. Integration of the transition elements should be performed over the nanocrystal volume V_{nc}. F is the local-field factor, and was calculated using the Maxwell-Garnett effective medium theory [10]. The size-dependence of Γ_j will be determined by the size-dependence of the matrix element $\langle 0|\mathbf{p}|j\rangle$ and emission frequency ω_j. In the case of strong confinement, the electron-hole states near the band-extrema can be written as a product of a Bloch function $\mu(\mathbf{r})$ and an envelope function $\phi(\mathbf{r})$. Then the matrix element in eq. 4.3 becomes

$$\langle 0|\mathbf{p}|j\rangle = \langle \mu_0^*(\mathbf{r})\phi_0^*(\mathbf{r})|\mathbf{p}|\mu_j(\mathbf{r})\phi_j(\mathbf{r})\rangle \tag{4.4}$$

The momentum operator is equal to $-i\hbar\nabla$, where ∇ is the gradient operator, and eq. 4.4 can be rewritten using the product rule for derivation:

$$\langle 0|\mathbf{p}|j\rangle = \langle \mu_0^*(\mathbf{r})\phi_0^*(\mathbf{r})\mu_j(\mathbf{r})|\mathbf{p}|\phi_j(\mathbf{r})\rangle + \langle \mu_0^*(\mathbf{r})\phi_0^*(\mathbf{r})\phi_j(\mathbf{r})|\mathbf{p}|\mu_j(\mathbf{r})\rangle \tag{4.5}$$

The envelope function varies slowly in the unit-cell and the Bloch function varies strongly in the unit-cell. Therefore, integration of $\mu(\mathbf{r})$ and $\phi(\mathbf{r})$ can be separated; the volume average of the slowly varying component $\phi(\mathbf{r})$ can be regarded as a constant and taken before the integration of $\mu(\mathbf{r})$. As a result, eq. 4.5 becomes:

$$\langle 0|\mathbf{p}|j\rangle = \frac{1}{V_{nc}}\langle \mu_0^*(\mathbf{r})|\mu_j(\mathbf{r})\rangle\langle \phi_0^*(\mathbf{r})|\mathbf{p}|\phi_j(\mathbf{r})\rangle + \frac{1}{V_{nc}}\langle \phi_0^*(\mathbf{r})|\phi_j(\mathbf{r})\rangle\langle \mu_0^*(\mathbf{r})|\mathbf{p}|\mu_j(\mathbf{r})\rangle \tag{4.6}$$

where $\frac{1}{V_{nc}}\langle\phi_0^*(\mathbf{r})|\mathbf{p}|\phi_j(\mathbf{r})\rangle$ and $\frac{1}{V_{nc}}\langle\phi_0^*(\mathbf{r})\phi_j(\mathbf{r})\rangle$ are the volume-averages of the slowly varying envelope functions. In the regime of strong confinement the envelope functions in the ground state and in the first excited state are equal, i.e., $\langle\phi_0^*(\mathbf{r})|\phi_j(\mathbf{r})\rangle = 1$ and $\langle\phi_0^*(\mathbf{r})|\mathbf{p}|\phi_j(\mathbf{r})\rangle = 0$. Therefore, in the strong confinement regime the matrix element of the momentum operator for an allowed transition is given by

$$\langle 0|\mathbf{p}|j\rangle = \frac{1}{V_{nc}}\langle\mu_0^*(\mathbf{r})|\mathbf{p}|\mu_j(\mathbf{r})\rangle \tag{4.7}$$

In eq. 4.7 integration is performed over the whole volume of the nanocrystal and the result is divided by the same volume. The matrix element of the momentum operator is thus equal to

$$\langle 0|\mathbf{p}|j\rangle = \frac{1}{nV_0}\langle\mu_0^*(\mathbf{r})|\mathbf{p}|\mu_j(\mathbf{r})\rangle = \frac{1}{V_0}\langle\mu_0^*(\mathbf{r})|\mathbf{p}|\mu_j(\mathbf{r})\rangle_{V_0} \tag{4.8}$$

where n is the number of unit-cells in the nanocrystal and V_0 the volume of the unit-cell. Integration of the last element of eq. 4.8 is performed over the volume of the unit-cell volume V_0. Inter-band transitions are thus largely determined by the Bloch functions in the unit-cell, which are defined by the crystal lattice only [3]. As a consequence, $\langle 0|\mathbf{p}|j\rangle$ does not depend on the size of the nanocrystals or on the emission frequency, and the decay rate of an ideal two-level exciton is expected to be proportional to the emission frequency; $\Gamma_j = constant \cdot \omega_j$. This result has been predicted in several theoretical studies [2, 28–30][2].

A real nanocrystal cannot be regarded as an ideal two-level system. We must consider the complex valence band structure of CdTe and CdSe; it appears that several hole levels are located close to the top of the band [31].

[2] In these studies it is shown that, in the case of strong confinement, the oscillator strength *per unit volume of material* of a nanocrystal suspension is enhanced by a factor proportional to the nanocrystal concentration:

$$\frac{f(suspension)}{f(bulk-crystal)} = \frac{3}{4}\left(\frac{a_B^*}{R}\right)^3 \frac{\omega_{bulk}}{\omega_j} \tag{4.9}$$

where f is the oscillator strength (see eq. 1.1), a_B^* is the Bohr radius of the exciton, and ω_j and ω_{bulk} are the emission frequency of the nanocrystal and the bulk crystal, respectively. Equivalently, the oscillator strength *per nanocrystal* times its emission frequency is independent of nanocrystal size. This conclusion is consistent with our conclusion that the matrix element of momentum is independent of the crystal size.

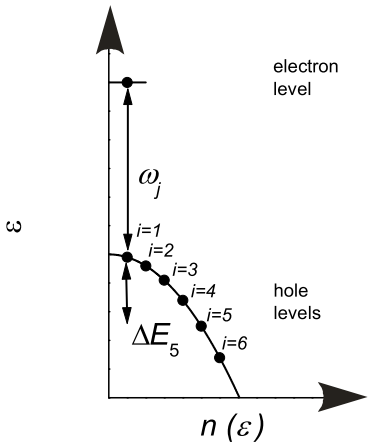

Figure 4.1: *Model for a multi-level exciton, presented as the energy versus the electronic density of states $n(\varepsilon)$. For the electron only one level is involved while for the hole several levels are involved. The density of hole states is approximated by the density of states for a macroscopic crystal (eq. 4.17).ΔE_5 is the energy difference between the states i=1 and i=5.*

This leads to other exciton states close to the lowest energy exciton. These excitons are dark since the excitons' total angular momentum $|F|$ is larger than 1; in emission or absorption $|F|$ is therefore not conserved [3]. We assume that the quantum confinement in the conduction band is strong; the s-p separation is at least 100 meV and therefore only the ground state is populated. We do not take into account the singlet-triplet splitting since its small energy difference does not introduce dispersion of the rate with frequency. Excitons in excited hole states have a much lower probability for spontaneous decay to the ground state (dark states) and will, therefore, reduce the total decay rate. The hole states will be labelled by an index i, with $i = 1$ being the highest hole state. The energy splitting between state 1 and state i is defined by ΔE_i and the probability of occupation of state i is called p_i. Figure 4.1 schematically shows the structure of a multi-level exciton with one electron and several holes states. The radiative decay rate for such complex excitons is given by

$$\Gamma_{\mathrm{rad}} = \sum_{i=1}^{N} p_i \, \Gamma_i \tag{4.10}$$

where N is the total number of hole states and Γ_i the radiative decay rate of state i. The total sum over i of p_i is equal to 1. We assume that the decay

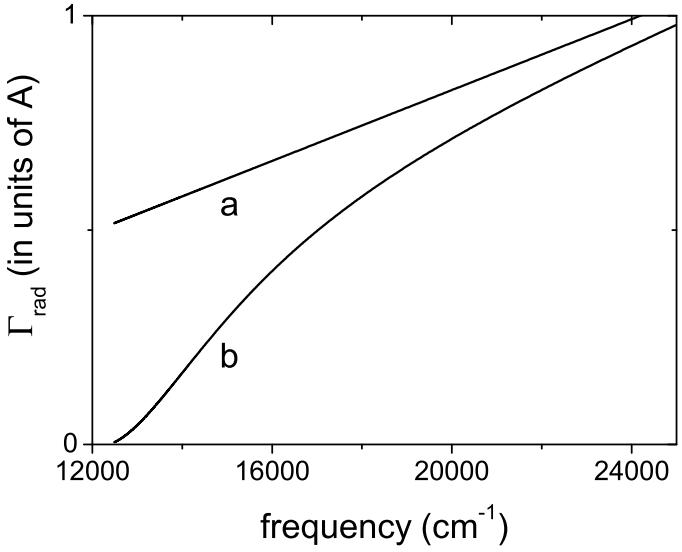

Figure 4.2: *Radiative decay rate for a simple two-level exciton (a) and a multi-level exciton (b) in a spherical CdTe nanocrystal. Line (a) is the radiative decay rate according to eq. 4.15 with $\Delta E_j \gg kT$, i.e., $A \cdot \omega_j$, and crosses the point ($\omega_j = 0, \Gamma_{rad} = 0$), and curve (b) shows the radiative decay rate predicted by eq. 4.20, with T=298.15 K. The y-axis is in units of the adjustable parameter A.*

rate of excited hole states vanishes. Therefore eq. 4.10 will reduce to

$$\Gamma_{\mathrm{rad}} = p_1 \, \Gamma_1 \tag{4.11}$$

Using

$$p_1 = 1 - \sum_{i=2}^{N} p_i \tag{4.12}$$

and the Boltzmann partition function to find the population of the various states:

$$\frac{p_i}{p_1} = \exp(\frac{-\Delta E_i}{kT}) \tag{4.13}$$

results in

$$\frac{1}{p_1} = 1 + \sum_{i=2}^{N} \exp(\frac{-\Delta E_i}{kT}) \tag{4.14}$$

After substitution of eq. 4.14 in eq. 4.11 the following expression for the

decay rate Γ_{rad} is obtained:

$$\Gamma_{\mathrm{rad}} = \Gamma_1 \left[1 + \sum_{j=2}^{N} \exp\left(\frac{-\Delta E_j}{kT} \right) \right]^{-1} \tag{4.15}$$

The sum in eq. 4.15 can be approximated by

$$\sum_{j=2}^{N} \exp\left(\frac{-\Delta E_j}{kT} \right) \approx \int_0^{\infty} n(\varepsilon) \exp(-\varepsilon/kT) d\varepsilon \tag{4.16}$$

where $n(\varepsilon)$ is the electronic density of states of a macroscopic crystal per unit energy per spin orientation [31]

$$n(\varepsilon) = \frac{R^3}{3\pi} \left(\frac{2m^*}{\hbar^2} \right)^{3/2} \sqrt{\varepsilon} \tag{4.17}$$

where R is the nanocrystal radius and m^* the effective hole mass[3]. Combining eq. 4.16, eq. 4.17 and 4.15 we can derive

$$\Gamma_{\mathrm{rad}} = \Gamma_1 \left[1 + \frac{R^3}{6\sqrt{\pi}} \left(\frac{2m^* kT}{\hbar^2} \right)^{\frac{3}{2}} \right]^{-1} \tag{4.19}$$

Since it was shown above that Γ_1 is linearly proportional to the frequency of the emitted light, eq. 4.19 thus becomes

$$\Gamma_{\mathrm{rad}} = A\,\omega_j \left[1 + \frac{R^3}{6\sqrt{\pi}} \left(\frac{2m^* kT}{\hbar^2} \right)^{\frac{3}{2}} \right]^{-1} \tag{4.20}$$

In order to calculate the frequency dependence of the radiative decay rate, the relation between the radius of the nanocrystal R and the emission frequency ω_j should be known. This relation was obtained from tight-binding calculations. With tight-binding calculations the emission frequency was calculated for nanocrystals with various sizes. Results of the tight-binding calculations for spherical CdTe nanocrystals are plotted in figure 4.3. The

[3]The effective mass must take into account the heavy and light hole and is given by

$$m^* = (m_{hh}^{\frac{3}{2}} + m_{lh}^{\frac{3}{2}})^{\frac{2}{3}} \tag{4.18}$$

For zinc blend CdTe and CdSe this results in an effective mass of 0.69 and 2.17, respectively.

results were fitted with a phenomenological expression (dashed curve in figure 4.3[4]) [32] and the equation was inserted into eq. 4.20. The resulting frequency dependency of the radiative decay rate for a simple two-level exciton and for a multi level exciton are plotted in figure 4.2. The y-axis is in units of the parameter A.

The effect of thermal occupation of optically non-active hole states as a function of crystal size is caught by the separation between the different exciton levels ΔE_j in eq. 4.15. For nanocrystals with a larger radius the total number of states is larger and therefore the separation between the states is smaller. As a consequence, thermal population of higher exciton levels is more important in larger nanocrystals. This means that the radiative decay rate of the large crystals is reduced more strongly than the rate of small crystals. In other words, the decrease of the radiative rate is larger at smaller frequency, as can be observed in figure 4.2. Consequently, the decay rate increases supra-linearly with frequency, instead of linearly as for an ideal two-level exciton system.

4.3.2 Tight-binding calculations

At a given temperature, the rate of radiative exciton decay depends on the details of the band structure, determined by the crystal lattice. In the above considerations several approximations are used to obtain eq. 4.20, i.e., infinite lifetimes for higher exciton states, strong confinement of the electron and density of states of a macroscopic crystal for the top of the valence band. The top of the valence band is in reality more complex than assumed in eq. 4.17 [31]. While it is helpful to use these approximations to get physical insight, a more detailed calculation, based on tight-binding or pseudo-potential models, is required to obtain quantitative decay rates. In the tight-binding approximation [10, 31] the wave functions of the nano-

[4]For CdTe:

$$\omega_j = 1.232 \times 10^4 + \frac{1}{2.558 \times 10^{-5} R^2 + 2.369 \times 10^{-5} R + 1.120 \times 10^{-5}} \tag{4.21}$$

and for CdSe

$$\omega_j = 1.452 \times 10^4 + \frac{1}{4.608 \times 10^{-5} R^2 + 1.431 \times 10^{-5} R + 1.644 \times 10^{-5}} \tag{4.22}$$

where ω_j is the frequency (with units cm^{-1}) and R the radius (with units nm).

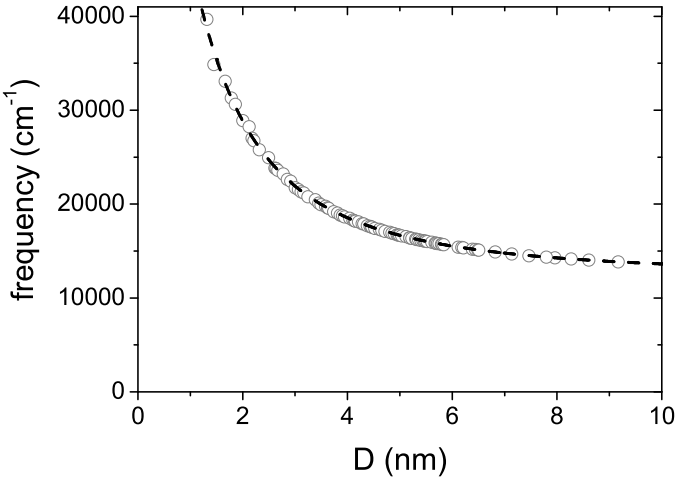

Figure 4.3: *Energy difference between the HOMO and the LUMO for a spherical CdTe nanocrystal (grey dots) as a function of the diameter. A fit with a phenomenological expression (see footnote 4) is also plotted (black dashed curve).*

crystal are constructed from a small number of atomic wave functions. In our case the tight-binding Hamiltonian matrix is written in a $sp^3d^5s^*$ basis including spin-orbit coupling and with interactions restricted to first nearest neighbours [32]. The parameters are obtained by a fit of the experimental effective masses with a reference bulk band structure calculated using the *ab initio* pseudopotential code ABINIT in the local density approximation [33]. These parameters are transferred without change from the bulk case to the nanocrystals and the surfaces are passivated with pseudo-hydrogen atoms [32]. The matrix elements of $\mathbf{p}$ are calculated following Ref. [32], which is used to calculate Γ_{rad} via eq. 4.3. In the calculations all transitions, including higher excitonic states and the singlet-triplet splitting, are taken into account.

The tight-binding results for the energy difference of the highest occupied molecular orbital (HOMO) and the lowest unoccupied molecular orbital (LUMO) for spherical CdTe nanocrystals are shown in figure 4.3. These results are in quantitative agreement with several results reported in Refs. [34–36]. The phenomenological equation which was used to plot eq. 4.20 (see footnote 4) is also plotted.

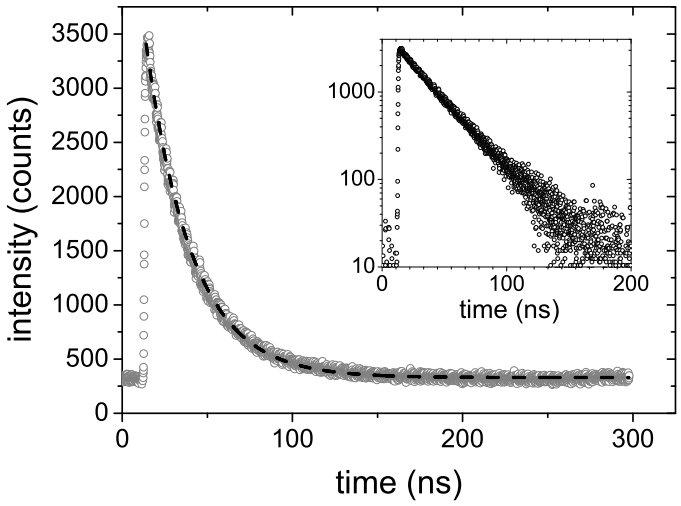

Figure 4.4: *Luminescence decay curve of exciton emission from CdSe nanocrystals with an average diameter of 6 nm at a wavelength of λ =620 nm $\pm$5 nm (open grey dots). Single-exponential fit (black dashed curve), with background as adjustable parameter, yields a rate of 0.037 $\pm$ 0.003 ns^{-1} and a χ_r^2-value of 1.4. A stretched-exponential model yields a rate of 0.036 ns^{-1} and a β-value of 0.99. Inset: the background corrected decay curve in a semilogarithmic plot.*

4.4 Results and discussion

In figure 4.4 an experimental luminescence decay curve for a CdSe suspension is shown. The data are well-described by a single-exponential model, as confirmed by a quality-of-fit χ_r^2 = 1.4, close to the ideal value of 1. A stretched-exponential model resulted in a stretch parameter β = 0.99, very close to the single-exponential limit of β = 1. Clearly, the decay curves are nearly single-exponential, which means that at a particular frequency all nanocrystals emit light with the same rate.

In figures 4.5 (a) and (c), the decay rate is plotted versus the emission frequency for CdTe and CdSe nanocrystals, respectively. Data from two different CdTe and two different CdSe suspensions are plotted in each of the figures. These data unambiguously show for the first time that the rate of excitonic decay increases strongly with increasing frequency. The strong

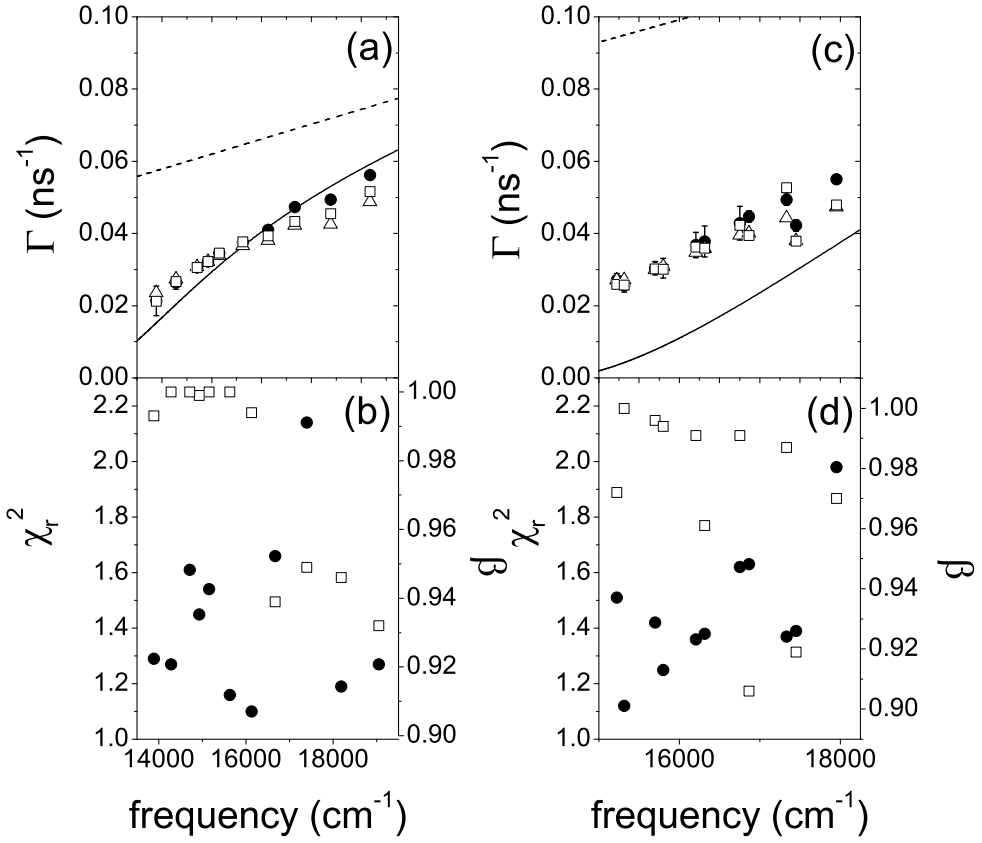

Figure 4.5: *Decay rate of emission from CdTe (a) and CdSe (c) nanocrystals and fit parameters ((b) and (d)). The decay rate is deduced from single-exponential fit (filled black dots), average arrival time (open triangles) and stretched exponential fit (open squares). The χ_r^2-values (filled black dots) and the β-values (open squares) were deduced from single exponential and from stretched exponential fits, respectively. The dashed black lines show the decay rates for a two-level system ($A \cdot \omega_j$, eq. 4.15, $\Delta E_j \gg kT$) and crosses the point ($\omega_j = 0, \Gamma_{rad} = 0$). The solid black curves show the rate according to eq. 4.20 and take dark excitonic states into account. For CdTe (a) A is 4.13$\times 10^{-6}$ cm ns^{-1} and for CdSe (b) A is 6.20$\times 10^{-6}$ cm ns^{-1}.*

increase of the decay rate with frequency confirms the contribution of inhomogeneous broadening to the emission spectrum of the suspension [26, 27].

The decay rate was deduced from three different procedures; the luminescence decay curve was fitted with a single-exponential, a stretched exponential and the average arrival time was calculated. The χ_r^2-values and the β-values were deduced from single exponential and from stretched exponential fits, respectively (figures 4.5(b) and (d)). The χ_r^2-values are low and the β-value in the stretched exponential fit varies between 0.91 and 1.00. Most of the curves have a β-value larger than 0.99. Clearly, the decay curves are nearly single-exponential which means that, at a given frequency, all the individual nanocrystals have the same decay rate.

The exciton decay rate calculated from eq. 4.20, with A as the only adjustable parameter, is presented in figure 4.5 (black solid curves) as a function of the frequency of the emitted light. The relation between R and ω was obtained from tight-binding calculations, plotted in figure 4.3. Clearly, the black solid curves in figure 4.5 show agreement with our measurements in the case of CdSe and excellent agreement in the case of CdTe. Therefore, we conclude that at room temperature thermal occupation of dark excitonic states reduces the rate of spontaneous emission considerably.

We have performed tight-binding calculations of the radiative decay rate for spherical zinc blende CdTe and CdSe nanocrystals with various sizes[5]. The calculated decay rates for CdTe are in quantitative agreement with the experimental results over the accessible frequency range (see grey filled dots in figure 4.6 (a)). In the case of CdSe (figure 4.6 (b)) the tight-binding results show a supra-linear relation between the radiative decay rate and the emission frequency; the increase is stronger than a linear increase from the origin. The deviation from the linear increase from the origin is in agreement with our experimental results. However, the absolute value is 75% too low. To understand the origin of this discrepancy, we have performed calculations using several sets of tight-binding parameters. We find that the absolute values of the emission rates are sensitive to these parameters due to a subtle coupling between close-spaced hole states. A similar discussion on the splitting and ordering of levels in the effective mass approximation can be found in the literature [34, 37, 38]. Importantly,

[5]X-ray diffraction measurements of CdTe and CdSe nanocrystals prepared with the same synthesis-routes are presented in Refs. [4] and [5], respectively.

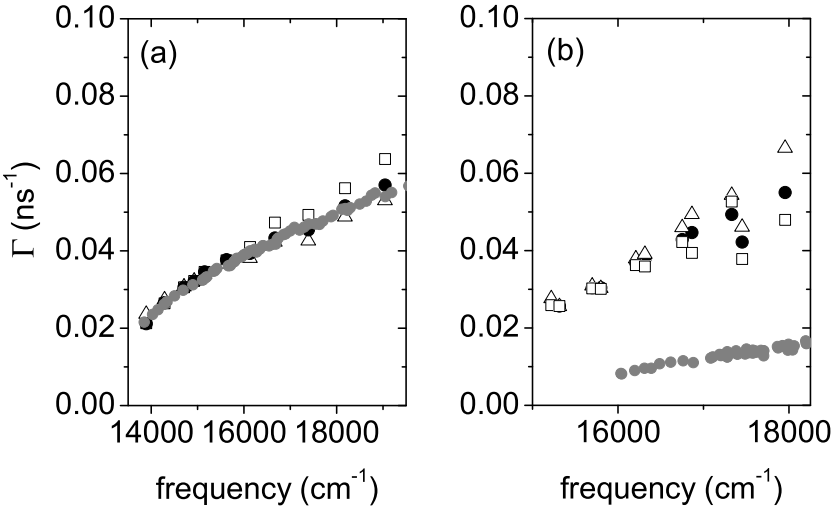

Figure 4.6: *Radiative decay rate from tight-binding calculations (grey dots) for CdTe (a) and CdSe (b). The same experimental data as in figure 4.5 are plotted.*

we find that the supra-linear evolution with frequency remains unaffected for all parameter sets.

In figures 4.5 and 4.6, we have compared the experimentally determined total decay rate, i.e., the sum of radiative and non-radiative decay rates, with the theoretically calculated radiative decay rate and we find good agreement. We argue that the non-radiative decay rate can be neglected, since our decay curves are nearly single-exponential. Decay rates measurements in single nanocrystals [25, 39] show that when a single nanocrystal reveals single-exponential decay, its non-radiative decay rate is negligible. For a large number of CdSe nanocrystals with the same diameter of 6.5 nm and emission frequency $\sim 1.7\times 10^4 \mathrm{cm}^{-1}$, a radiative single-exponential lifetime of 25 ns was observed, in excellent agreement with our results. Therefore, our measured 50% quantum efficiency can be explained in simple terms as follows: half of the nanocrystals have a low emission efficiency, while the other half have an emission efficiency close to one. It is the photons from the latter nanocrystals that mostly contribute to our measured signals.

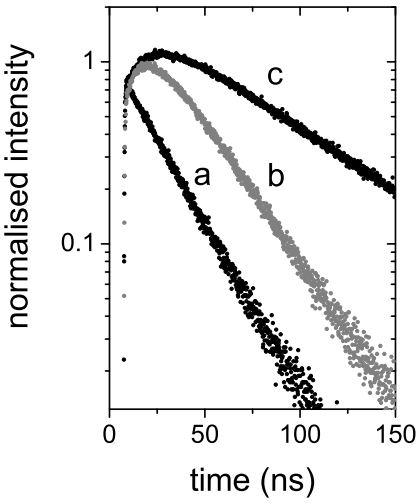

Figure 4.7: *Decay curves recorded on the blue side (a), peak (b) and red side (c) of the emission from a CdTe suspension with a relatively high concentration ($\sim 10^{-6}$ mol/l). The effect of re-absorption can clearly be observed at short time scale in curves (b) and (c).*

Three other effects may explain the increase of the decay rate with frequency: Förster energy transfer, re-absorption and emission related to defect states. However, all three effects were carefully ruled out. The concentration of nanocrystals was intentionally kept very low ($< 10^{-7}$ mol/l) to prevent Förster energy transfer and re-absorption. Besides, no hint of these two effects was observed in our luminescence decay curves. Figure 4.7 shows results for a suspension where re-absorption plays a role. A clear effect of re-absorption is observed observed at short time-scale; the intensity first increases, after which it decreases. In contrast, a monotonous decrease is observed for suspensions with a low concentration.

Förster energy transfer could be expected to play an important role in nanocrystal suspensions. CdSe and CdTe have a large dielectric constant and therefore the Van der Waals forces between the crystals can be large. A larger Van der Waals force can increase the probability of energy transfer considerably. For this reason the results for sterically stabilised CdTe nanocrystals were compared with charge-stabilised nanocrystals, which strongly repel each other at short distances. No difference was observed and it was therefore concluded that Förster energy transfer is not important in our suspensions.

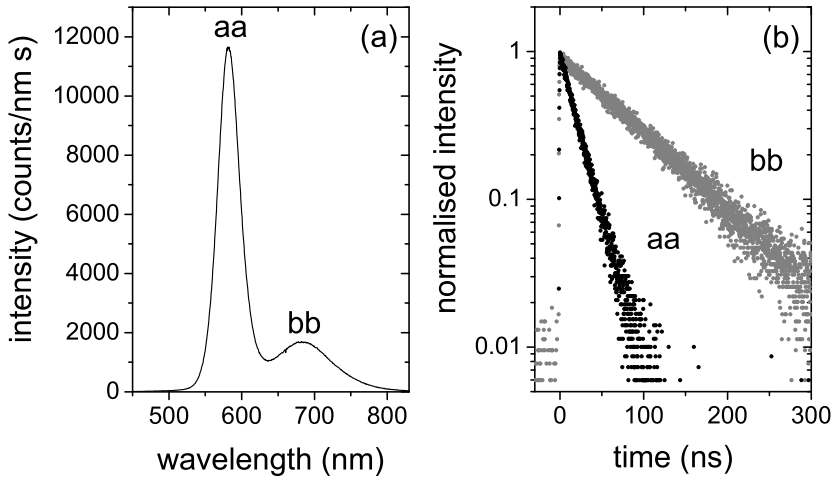

Figure 4.8: *Emission spectrum from a CdTe suspension with exciton ($\lambda \approx 600$ nm, aa) and defect ($\lambda \approx 700$ nm, bb) related emission (a) and decay curves (b) of exciton (aa) and defect (bb) related emission.*

Emission related to defects normally has an energy lower than exciton related emission, as shown in figure 4.8 (a). Besides this, transitions related to defects have a lower oscillator strength than exciton-related emission. Figure 4.8 (b) clearly demonstrates the lower oscillator strength: defect-related emission was spectrally selected and has longer lifetime than exciton-related emission, typically 0.1 μs. Defect-related emission also leads to an increase of the decay rate with frequency. For this reason, only suspensions were used in the present study with did not show any defect-related emission.

4.5 Conclusion

We have shown for the first time how the spontaneous emission rate of semiconductor nanocrystals depends on the frequency of the emitted light. Three other effects which can give rise to a decay rate increase with increasing frequency were ruled out. We presented a simple analytical theory and tight-binding calculations of the radiative decay rate. Comparison with theory shows that spontaneous emission is considerably attenuated due

to occupation of dark excitonic states. These results may lead to a better understanding of a number of dynamic effects, such as exciton dephasing and Förster energy transfer [12, 40] that are currently being studied in nanocrystals and nanocrystal assemblies. Knowledge of exciton dynamics is important for the develpoment of LEDs [16], low-threshold lasers [17], light-harvesting materials [12] and photon up-convertors.

References

[1] A. L. Efros and A. L. Efros, *Interband light absorption in a semiconductor sphere*, Fizika i Tekhnika Poluprovodnikov (Sankt-Peterburg) **16**, 1209 (1982).

[2] L. E. Brus, *Electron-electron and electron-hole interactions in small semiconductor crystallites: the size dependence of the lowest excited electronic state*, Journal of Chemical Physics **80**, 4403 (1984).

[3] A. L. Efros, M. Rosen, M. Kuno, M. Nirmal, D. J. Norris, and M. G. Bawendi, *Band-edge exciton in quantum dots of semiconductors with a degenerate valence band: Dark and bright exciton states*, Physical Review B **54**, 4843 (1996).

[4] D. V. Talapin, S. Haubold, A. L. Rogach, A. Kornowski, M. Haase, and H. Weller, *A novel organometallic synthesis of highly luminescent CdTe nanocrystals*, Journal of Physical Chemistry B **105**, 2260 (2001).

[5] D. V. Talapin, A. L. Rogach, A. Kornowski, M. Haase, and H. Weller, *Highly luminescent monodisperse CdSe and CdSe/ZnS nanocrystals synthesized in a hexadecylamine-trioctylphosphine oxide- trioctylphospine mixture*, Nano Letters **1**, 207 (2001).

[6] P. Reiss, J. Bleuse, and A. Pron, *Highly luminescent CdSe/ZnSe core/shell nanocrystals of low size dispersion*, Nano Letters **2**, 781 (2002).

[7] C. de Mello Donegá, S. G. Hickey, S. F. Wuister, D. Vanmaekelbergh, and A. Meijerink, *Single-step synthesis to control the photoluminescence quantum yield and size dispersion of CdSe nanocrystals*, Journal of Physical Chemistry B **107**, 489 (2003).

[8] S. F. Wuister, F. van Driel, and A. Meijerink, *Luminescence and growth of CdTe quantum dots and clusters*, Physical Chemistry Chemical Physics **5**, 1253 (2003).

[9] S. F. Wuister, I. Swart, F. van Driel, S. G. Hickey, and C. de Mello Donegá, *Highly luminescent water-soluble CdTe quantum dots*, Nano Letters **3**, 503 (2003).

[10] C. Delerue and M. Lannoo, *Nanostructures: Theory and Modeling*, international ed. (Springer Verlag, Berlin Heidelberg New York, 2004).

[11] R. Loudon, *The Quantum Theory of Light*, 3rd ed. (Oxford University Press Inc., New York, 2001).

[12] S. A. Crooker, J. A. Hollingsworth, S. Tretiak, and V. I. Klimov, *Spectrally resolved dynamics of energy transfer in quantum-dot assemblies: Towards engineered energy flows in artificial materials*, Physical Review Letters **89**, 186802 (2002).

[13] W. C. W. Chan and S. Nie, *Quantum dot bioconjugates for ultrasensitive nonisotopic detection*, Science **281**, 2016 (1998).

[14] M. Bruchez, M. Moronne, P. Gin, S. Weiss, and A. P. Alivisatos, *Semiconductor nanocrystals as fluorescent biological labels*, Science **281**, 2013 (1998).

[15] P. Michler, A. Kiraz, C. Becher, W. V. Schoenfeld, P. M. Petroff, L. D. Zhang, E. Hu, and A. Imamoglu, *A quantum dot single-photon turnstile device*, Science **290**, 2282 (2000).

[16] S. Coe, W. K. Woo, M. G. Bawendi, and V. Bulovic, *Electroluminescence from single monolayers of nanocrystals in molecular organic devices*, Nature **420**, 800 (2002).

[17] C. J. Wang, B. L. Wehrenberg, C. Y. Woo, and P. Guyot-Sionnest, *Light emission and amplification in charged CdSe quantum dots*, Journal of Physical Chemistry B **108**, 9027 (2004).

[18] P. Lodahl, A. F. van Driel, I. S. Nikolaev, A. Irman, K. Overgaag, D. Vanmaekelbergh, and W. L. Vos, *Controlling the dynamics of spontaneous emission from quantum dots by photonic crystals*, Nature **430**, 654 (2004).

[19] T. Rajh, O. I. Micic, and A. J. Nozik, *Synthesis and characterization of surface-modified colloidal CdTe quantum dots*, Journal of Physical Chemistry **97**, 11999 (1993).

[20] T. Vossmeyer, L. Katsikas, M. Giersig, I. G. Popovic, K. Diesner, A. Chemseddine, A. Eychmuller, and H. Weller, *CdS nanoclusters - Synthesis, characterization, size-dependent oscillator strength, temperature shift of the excitonic-transition energy, and reversible absorbency shift*, Journal of Physical Chemistry **98**, 7665 (1994).

[21] C. A. Leatherdale, W. K. Woo, F. V. Mikulec, and M. G. Bawendi, *On the absorption cross section of CdSe nanocrystal quantum dots*, Journal of Physical Chemistry B **106**, 7619 (2002).

[22] A. Striolo, J. Ward, J. M. Prausnitz, W. J. Parak, D. Zanchet, D. Gerion, D. Milliron, and A. P. Alivisatos, *Molecular weight, osmotic second virial coefficient, and extinction coefficient of colloidal CdSe nanocrystals*, Journal of Physical Chemistry B **106**, 5500 (2002).

[23] W. W. Yu, L. H. Qu, W. Z. Guo, and X. G. Peng, *Experimental determination of the extinction coefficient of CdTe, CdSe, and CdS nanocrystals*, Chemistry of Materials **15**, 2854 (2003).

[24] S. A. Crooker, T. Barrick, J. A. Hollingsworth, and V. I. Klimov, *Multiple temperature regimes of radiative decay in CdSe nanocrystal quantum dots: Intrinsic limits to the dark-exciton lifetime*, Applied Physics Letters **82**, 2793 (2003).

[25] B. R. Fisher, H. J. Eisler, N. E. Stott, and M. G. Bawendi, *Emission intensity dependence and single-exponential behavior in single colloidal quantum dot fluorescence lifetimes*, Journal of Physical Chemistry B **108**, 143 (2004).

[26] W. G. J. H. M. van Sark, P. L. T. M. Frederix, A. A. Bol, H. C. Gerritsen, and A. Meijerink, *Blueing, bleaching, and blinking of single CdSe/ZnS quantum dots*, ChemPhysChem **3**, 871 (2002).

[27] F. Koberling, U. Kolb, G. Philipp, I. Potapova, T. Basche, and A. Mews, *Fluorescence anisotropy and crystal structure of individual semiconductor nanocrystals*, Journal of Physical Chemistry B **107**, 7463 (2003).

[28] T. Takagahara, *Excitonic optical nonlinearity and exciton dynamics in semiconductor quantum dots*, Physical Review B **36**, 9293 (1987).

[29] Y. Kayanuma, *Quantum-size effects of interacting electrons and holes in semiconductor microcrystals with spherical shape*, Physical Review B **38**, 9797 (1988).

[30] Y. Wang and N. Herron, *Nanometer-sized semiconductor clusters - Materials synthesis, quantum size effects, and photophysical properties*, Journal of Physical Chemistry **95**, 525 (1991).

[31] C. Kittel, *Introduction to Solid State Physics*, 7th ed. (John Wiley & Sons, Inc., New York, 2004).

[32] G. Allan, Y. M. Niquet, and C. Delerue, *Quantum confinement energies in zinc-blende III-V and group IV semiconductors*, Applied Physics Letters **77**, 639 (2000).

[33] X. Gonze, J. M. Beuken, R. Caracas, F. Detraux, M. Fuchs, G. M. Rignanese, L. Sindic, M. Verstraete, G. Zerah, F. Jollet, M. Torrent, A. Roy, M. Mikami, P. Ghosez, J. Y. Raty, and D. C. Allan, *First-principles computation of material properties: the ABINIT software project*, Computational Materials Science **25**, 478 (2002).

[34] T. Richard, P. Lefebvre, H. Mathieu, and J. Allegre, *Effects of finite spin-orbit splitting on optical properties of spherical semiconductor quantum dots*, Physical Review B **53**, 7287 (1996).

[35] S. J. Prado, C. Trallero-Giner, A. M. Alcalde, V. Lopez-Richard, and G. E. Marques, *Optical transitions in a single CdTe spherical quantum dot*, Physical Review B **68**, 235327 (2003).

[36] L. W. Wang and J. B. Li, *First-principles thousand-atom quantum dot calculations*, Physical Review B **69**, 153302 (2004).

[37] A. L. Efros and M. Rosen, *Comment on "Comparison of the $k \cdot p$ and the direct diagonalization approaches for describing the electron structure of quantum dots"*, Applied Physics Letters **73**, 1155 (1998).

[38] H. X. Fu, L. W. Wang, and A. Zunger, *Comment on "Comparison of the $k \cdot p$ and the direct diagonalization approaches for describing the electron structure of quantum dots" - Response*, Applied Physics Letters **73**, 1157 (1998).

[39] Y. Ebenstein, T. Mokari, and U. Banin, *Fluorescence quantum yield of CdSe/ZnS nanocrystals investigated by correlated atomic-force and single-particle fluorescence microscopy*, Applied Physics Letters **80**, 4033 (2002).

[40] C. R. Kagan, C. B. Murray, M. Nirmal, and M. G. Bawendi, *Electronic energy transfer in CdSe quantum dot solids*, Physical Review Letters **76**, 1517 (1996).

Chapter 5

Controlling the dynamics of spontaneous emission from semiconductor nanocrystals by photonic crystals

abstract

Experiments are reported to determine the influence of a photonic crystal environment on spontaneous emission of embedded atom-like light sources. Titania inverse opal photonic crystals with various lattice parameters were doped with ZnSe-capped CdSe nanocrystals. It is shown that both the spectral distribution and the time-dependent response are controlled by the photonic crystal host. The multi-exponential decay curves were successfully modelled with a decay rate distribution model. At a fixed emission frequency, the radiative rate varies by a factor three, in agreement with the theoretical photonic density of states. A variation of a factor-of-six in the width of the decay rate distribution was observed. The width is identified with the spatial variation of the local density of optical modes probed by the nanocrystals at various positions in the unit-cell.

5.1 Introduction

The periodic crystal structure of an electronic insulator causes Bragg diffraction of the electrons [1]. As a consequence, there are frequency windows that are forbidden in a certain propagation direction. A so-called bandgap will open in the case in which all propagation modes, i.e., all directions, are forbidden in a certain frequency-window. The propagation of light in photonic crystals bears similarities to the propagation of electrons in insulators [2–4]. In photonic crystals certain propagation modes are forbidden and, as a consequence, stop gaps open. The stop gap can be probed with an external light source in reflectance or transmittance measurements [5]. A second way to observe stop gaps is to embed light sources in the photonic crystal. The influence of the stop gaps on the emission of the light sources is observed in angle-dependent spectral measurements [6, 7].

Photonic crystals can also control the time-response of the spontaneous emission of embedded light sources. Due to the combined Bragg diffraction in many directions the density of optical modes at the location of the light source, i.e., the local density of states (LDOS), is modified. According to Fermi's 'golden rule' the rate of spontaneous emission, or the radiative decay rate, is proportional to the LDOS. An important research goal is the achievement of a material with a photonic bandgap, i.e., a material with a frequency window in which no modes exist and in which, as a consequence, spontaneous emission of light is completely inhibited. Several authors claimed a material with a complete photonic bandgap [8–10]. However, no definite proof of a complete photonic bandgap in these materials was presented. Photonic crystals which strongly interact with light are known. In these materials most directions of propagation are excluded. A modification of the LDOS and, as a consequence, the rate of spontaneous emission, can be anticipated. However, no convincing experimental data of the control of the lifetime of an light source embedded in photonic crystals has been reported.

It has been predicted [11] that an incomplete bandgap might be sufficient to obtain complete suppression of the LDOS and consequently complete inhibition of spontaneous emission at a particular location. This is a much weaker condition for complete inhibition than full suppression of the unit-cell integrated LDOS. Since the total number of modes must be

conserved, the LDOS might be expected to increase strongly at some frequencies outside the pseudo-gap. Photonic crystals may therefore radically change the radiative emission rates between complete inhibition and strong enhancement even in the absence of a complete photonic bandgap. In order to study emission in three-dimensional photonic crystals, knowledge on the spatial distribution and control of the distribution of the emitters is required.

To the best of our knowledge, all experimental work on emission in photonic crystals is concerned with the frequency dependence of the LDOS. The position dependence of the LDOS in front of a planar mirror was investigated for the first time by K. H. Drexhage [12]; he studied the effect of the position and orientation of the transition dipole moment of an emitter on the radiative decay rate. He observed that, depending on the distance to the mirror, the radiative decay rate of europium ions is periodically inhibited and enhanced. After the pioneering experiments of Drexhage, numerous experiments on manipulation of the DOS with cavities have been reported [13]. In this Chapter an alternative approach to study the position dependence of the LDOS is presented. An ensemble of emitters is distributed over a well-defined subset of positions in the unit-cell of a titania inverse opal photonic crystal and the frequency dependence of the distribution of the emission rates is studied.

In this Chapter experiments are reported on the influence of a photonic crystal environment on spontaneous emission of embedded atom-like light sources. Titania inverse opal photonic crystals were doped with ZnSe-capped CdSe nanocrystals. First, the influence of the photonic crystal on the emission spectra of the nanocrystals was determined. Angle-dependent measurements confirmed that the spectra are strongly influenced by the photonic crystal environment, and thus that the nanocrystals are affected by the photonic crystal. Second, the influence of the photonic crystal on the time-dependent response of the exciton-related emission from nanocrystals was studied. The multi-exponential decay curves were analyzed by two methods: a single-exponential model and a model based on a log-normal distribution of decay rates. Both inhibited and enhanced decay rates were observed, depending on the emission frequency and the photonic crystals' lattice parameter. Therefore, it was concluded that the decay rates are con-

trolled by the photonic crystals. These observations are in surprisingly good agreement with DOS-calculations. The distribution of decay rates is strongly influenced by the photonic crystal; the width shows a six-fold variation while the variation in the rate is about three-fold. The width of the distribution was identified with the spatial variation of the LDOS that is probed by nanocrystals at various positions at the unit-cell.

5.2 Experimental

5.2.1 Sample preparation

The experiments were performed with titania inverse opals that consisted of a face-centered cubic (fcc) structure of air spheres in a titania backbone. The inverse opals were fabricated by inverting template assisted self-assembled structures [14][1]. Typical dimensions of the samples were $2 \times 2 \times 0.3$ mm^3. The high quality of the crystals is shown by the long scattering mean free path of light propagation of 15-20 μm [15]. In total, seven different samples were studied with lattice parameters ranging from a=240 nm to 650 nm. The photonic crystals were infiltrated for 24 hours with a mixture of 50% chloroform and 50% butanol containing 10^{-7} mol/litre ZnSe-coated CdSe colloidal nanocrystals. Experimental details on the synthesis and characterisation of these nanocrystals can be found in Chapter 2. The samples were subsequently rinsed for one minute in chloroform and dried. The nanocrystals had a size dispersity of 5% [16] around an average diameter of 4.5 nm. The infiltration led to a distribution of nanocrystals on the surfaces of the air spheres inside the inverse opal with a density of less than 10 nanocrystals per air sphere. This is sufficiently low to avoid energy transfer between nanocrystals [17]. The ensemble of nanocrystals in the solution had a lifetime of around 20 ns and a quantum efficiency of 50%$\pm$5%; the latter was measured by comparing absorption and emission with respect to a Rhodamine 101 dye standard [18]. To minimize oxidation and contamination, all sample preparation and handling was carried out in a nitrogen-purged glove box, and the optical measurements were performed in a sealed chamber under 1.7 mbar nitrogen.

[1] The photonic crystals were fabricated by L. A. Woldering and L. Bechger from the group Complex Photonic Systems at the University of Twente

5.2.2 Characterisation

A Fourier transform spectrometer (Biorad FTS-6000) was used to measure the reflectivity. Extensive details on reflectivety measurements are reported in Ref. [19]. Tungsten halogen and xenon lamps were used, in combination with a silicon photodiode detector, to measure reflection spectra in a range from 9000 cm^{-1} to 24000 cm^{-1}. A silver mirror with a constant reflectivity of more than 95 % in this spectral range was used as a reference. Reflectivity measurements were used to determine the lattice parameter a of our photonic crystals. This was preferred to scanning electron microscopy (SEM), since a reflectivity measurement probes the same area of the photonic crystal as in the lifetime measurements. According to Bragg's law the lattice parameter a and the position of the reflection maximum are related:

$$a = \frac{\sqrt{}3\, m\, \lambda_{max}}{2\cos(\alpha)\, n_{av}} \tag{5.1}$$

where m is the order of the reflection, λ_{max} the spectral position of the maximal reflectance, n_{av} the average refractive index and α the angle relative to the surface normal, which corresponds to the $[111]$-direction. We assume an average refractive index of 1.17 [20]. The spot size was 0.2 mm and the spectral resolution was 16 cm^{-1}. Optical excitation of the nanocrystals was performed with either a continuous-wave argon laser (λ_{ex}=488 nm) or a Pico Quant picosecond laser (λ_{ex}= 440 nm). A Hamamatsu photomultiplier tube was used for detection. The continues-wave argon laser was used for the spectral measurements and the picosecond laser for time-resolved experiments. The excitation beam was coupled through a single-mode fibre and illuminated the photonic crystal. The fibre and the sample were mounted on the same rotational stage, which allowed the detection angle to be changed while the excitation volume was kept constant. The spontaneously emitted light was detected from the surface facing away from the excitation beam at an angle α relative to the $[111]$-direction of the fcc lattice. The light was collected in a cone of $\sim 8^{\circ}$ around the detection angle, dispersed with a spectrometer (2 nm resolution), and measured with a fast photomultiplier. Time-correlated single-photon counting was implemented to measure the arrival time of the emitted photons. Careful measurements on reference samples ruled out the presence of energy trans-

fer [17], reabsorption and other non-photonic effects on the lifetime. The decay curves were obtained by binning the arrival times of the single photons detected with the photomultiplier. Contributions from dark counts in the photomultiplier were measured and subtracted from the data.

5.2.3 Data analysis

The decay curves were analysed with two methods. The raw, background corrected, decay curves which contained contributions from both titania and the nanocrystals were modelled with a single exponential decay from which the lifetime was extracted. Whereas strong lifetime effects were observed on the efficient luminescence from the nanocrystals, no systematic change of the lifetime from the low quantum efficiency titania luminescence was observed. To exclude contributions from the titania backbone, fitting was performed in the time-window from 5 ns to $\sim$ 20 ns. The signal at times longer than 5 ns was unaffected by titania luminescence. Analysis of the luminescence decay curves showed that the initial 20 ns can be approximated effectively by a single-exponential while this model fails at longer time scales. Therefore, a second procedure was applied. The titania contribution to the decay curves was carefully removed. In order to do this, the titania contribution was determined from additional measurements on undoped inverse opals and subtracted from the raw decay curves. The resulting decay curve, which is strongly non-single-exponential, was modelled between 0 ns and 80 ns with a decay-rate distribution model:

$$f(t) = \int_0^\infty \sigma(\Gamma) \exp(-\Gamma_{tot} t) d\Gamma \tag{5.2}$$

where t is the time, Γ is the decay rate and σ is the distribution function, which describes the radiative rate weighted distribution of the total decay rate (see Chapter 3). We used a log-Gaussian distribution to model our decay curves:

$$\sigma(\Gamma) = A \exp\left[-(\frac{\ln\Gamma - \ln\Gamma_{mf}}{\gamma})^2\right] \tag{5.3}$$

where A is the normalisation constant, Γ_{mf} is the most frequent rate constant. γ is related to the distribution width:

$$\Delta\Gamma = 2\Gamma_{mf}\sinh(\gamma) \tag{5.4}$$

where $\Delta\Gamma$ is equal to the width of the distribution at $\frac{1}{e}$. The most frequent rate constant and γ where set as adjustable parameters. In Chapter 3 it is shown that $\sigma(\Gamma)$ is given by

$$\sigma(\Gamma) = \rho(\Gamma_{tot})\int_0^{\Gamma_{tot}} \rho(\Gamma_{rad})\Gamma_{rad}d\Gamma_{rad} \tag{5.5}$$

where Γ_{rad} is the radiative decay rate, Γ_{tot} the total decay rate, i.e., the sum of the radiative and non-radiative rates, and $\rho(\Gamma_{tot})$ expresses the distribution of the various components over the rates. Thus, the width of the distribution is determined by both radiative and non-radiative decay rates.

5.3 Results

5.3.1 Reflectivity measurements

In this study air-sphere photonic crystals with seven different lattice parameters were used. The samples were characterised with scanning electron microscopy (SEM) and by reflectivity measurements. The lattice parameter was determined from the position of the reflectance maximum (see eq. 5.1) and varied between 240 nm and 650 nm. No reflection measurements were performed for the sample with a=240 nm since the reflectivity peak is outside the frequency region for which the light could be detected. The lattice parameter was therefore extracted from SEM images.

In figure 5.1 the reflection spectrum of four different titania inverse opals are shown. The first-order reflectance varies between $\sim 15\%$ and $\sim 50\%$. The reflectivity does not reach 100%, probably due to defects and small crystal domains. The focus of the beam is considerably larger than the size of the single-crystal domains (0.2 mm versus 0.05 mm). Crystal imperfections will give rise to an off-specular reflection, resulting in a decrease of the reflectance. Despite the fact that the reflectance is not 100%, a first-order Bragg reflection can clearly be observed and the quality of the

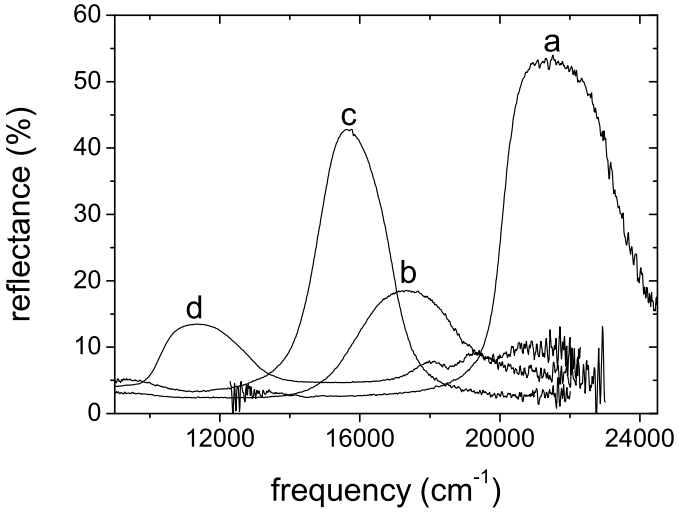

Figure 5.1: *Reflection spectra of titania inverse opals with lattice parameter 340 nm (a), 420 nm (b), 460 nm (c) and 650 nm (d). The reflection peaks result from first order (m=1) Bragg reflection.*

crystals is sufficient for the study of the modification of the LDOS.

5.3.2 Angle-resolved measurements

To confirm the influence of Bragg diffraction on the emission from the embedded nanocrystals, angle-resolved measurements of the emission spectra of light sources embedded in titania inverse opals were performed. As light sources, we use colloidal ZnSe-capped CdSe nanocrystals that are highly efficient, narrow linewidth, size-dependent emitters that effectively resemble two-level systems (see Chapter 4). Figure 5.2 shows the emission spectra for a sample with lattice parameter $a = 420$ nm for different detection angles α relative to the (111)-planes. An unusual angular dependence is observed: the emitted intensity is strongly attenuated at α=0°, increases at α=20° and α=50°, and decreases again at α=60°. This behavior is caused by a photonic stop gap centred at α=0° that is conveniently recognised when the emission spectra are referenced with respect to spectra measured at α=60°. The latter is a suitable reference because here the stop gaps are shifted far outside the emission spectrum of the nanocrys-

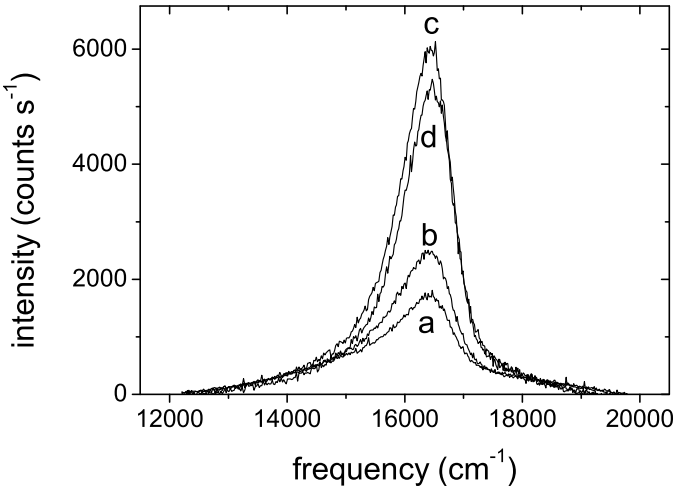

Figure 5.2: *Emission spectra of ZnSe-capped CdSe nanocrystals embedded in an inverse opal at an angle α of 0° (a), 20° (b), 50° (c) and 60° (d). α is defined as the angle relative to the surface normal. The lattice parameter of the crystal was 420 nm.*

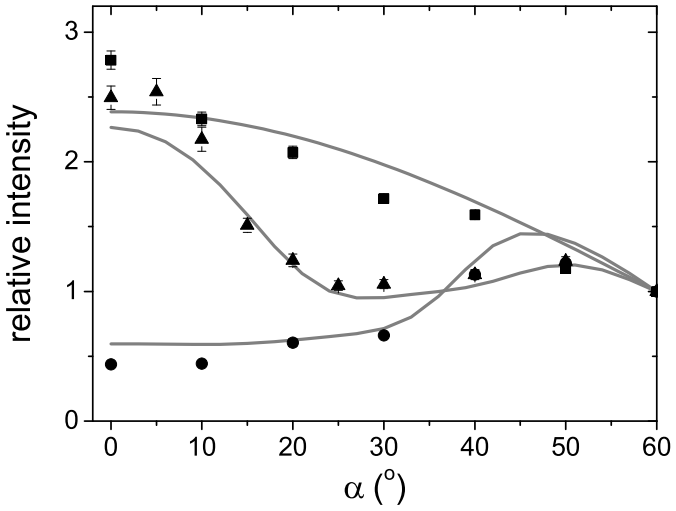

Figure 5.3: *Measured (points) and calculated (curves) angle-dependent intensities at a fixed frequency (ω=15870 cm^{-1}) for three crystals with lattice parameters a of 370 nm (squares), 420 nm (dots), and 500 nm (triangles).*

tals. Figure 5.3 displays the angular dependence of the relative intensity for samples with three different lattice parameters. For a reference sample with a small lattice parameter (a=370 nm), the stop gaps appear at frequencies higher than the emission spectrum of the nanocrystals and the intensity decays monotonously with increasing angle, known as Lambertian behavior; this is observed when the escape distribution is determined only by internal diffusion of light [21–23]. In contrast, the a=420 nm and a=500 nm samples show pronounced photonic effects with strongly reduced emission in a broad stop band centred at α=0° and α=25°, respectively. The measured angle-dependent intensities were compared to intensities calculated from a recently developed theory that describes propagation of light in real photonic crystals [7, 24]. The theory takes Bragg diffraction combined with diffusion by ubiquitous disorder into account. The curves in figure 5.3 were predicted with no adjustable parameters, and using only the measured reflectivity peaks and calculated band structure as input. Clearly, agreement between experiment and theory is excellent, confirming that the emission of the embedded nanocrystals is strongly affected by the photonic crystal.

5.3.3 Time-resolved measurements: short time-scale analysis

The decay rate of the excited state of the nanocrystals in the photonic crystal was measured by exciting with a short optical pulse and recording the spontaneous emission as a function of time. In photonic crystals, the LDOS and, as a result, the decay rate ideally disappears over a frequency range known as the photonic bandgap. In real crystals with finite dimensions, the LDOS is never zero, but strongly modulated pseudogaps are anticipated [11, 25]. In such gaps, vacuum fluctuations are expelled from the crystal, and the spontaneous decay of an excited emitter is inhibited. Away from a gap, the LDOS is increased and spontaneous emission will be enhanced.

Figure 5.4 shows decay curves measured for three different photonic crystals at selected optical frequencies. Two main contributions are present in the data: a fast decay ($\sim$1 ns) and a slow decay ($>$10 ns). The fast decay is caused by defect-related luminescence of the titania backbone, as confirmed from measurements on bare titania samples (figure 5.4, curve d). The slow decay is due to the nanocrystals, and is easily distinguished from

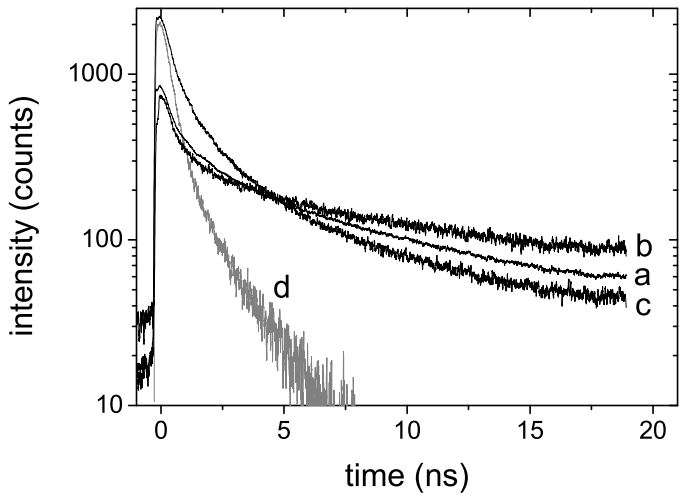

Figure 5.4: *Luminescence decay curve of exciton-related emission of CdSe nanocrystals embedded in three different photonic crystals (black curves a, b, and c). The data were recorded at ω=15670 cm^{-1} (curve a, a=370 nm), ω=15100 cm^{-1} (curve b, a=500 nm; curve c, a=420 nm). The curves have been made to coincide at t=5 ns. The first part of the decay curve is influenced by emission of titania (grey curve d, recorded at 15400 cm^{-1}) and after 5 ns this contribution is negligible.*

the titania emission owing to its markedly different decay time. Visual inspection of the decay curves in figure 5.4 reveals both accelerated and inhibited decay rates of the nanocrystals as compared to that measured in the non-photonic sample (a=370 nm). The lifetimes were 9.6$\pm$0.1 ns (a=420 nm) and 19.3$\pm$0.2 ns (a=500 nm), and for the reference sample the lifetime was 12.4$\pm$0.1 ns (a=370 nm).

In a first method to deduce a lifetime from our multi-exponential decay curves, we consider only photonic effects on the averaged lifetime that is obtained by investigating the quantum-dot decay curve up to $\sim$20 ns, which is least sensitive to background counts and can be approximated by a single exponential. The robustness of this method and the sensitivity to variations in the radiative decay rate were carefully checked by comparing results to those of a fit of the decay curve over a longer time-scale based on the distribution of lifetimes (see below). The observed lifetimes in the inverse opals are all systematically shorter than the lifetime of nanocrystals in

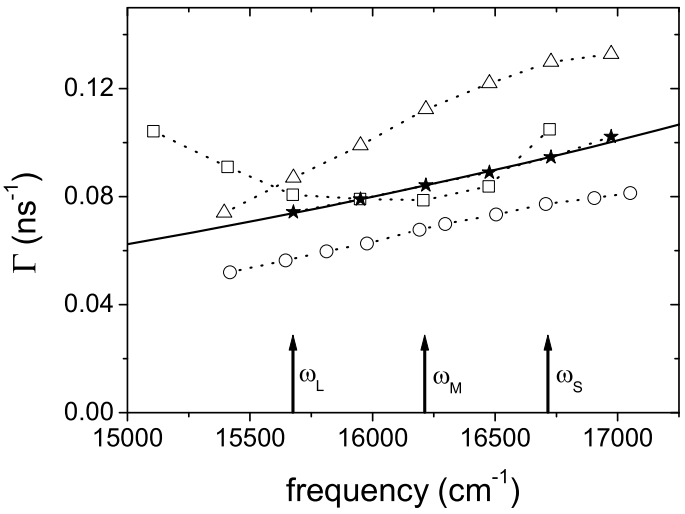

Figure 5.5: *Measured lifetimes of the excited states of CdSe nanocrystals in photonic crystals with different lattice parameters of a=370 nm (stars), a=420 nm (squares), a=460 nm (dots) and a=580 nm (triangles). The dotted curves connecting the measurement points are to guide the eye. The solid curve is the calculated lifetime for a homogeneous medium, based on a phenomenological fit of decay rates measured for suspensions of CdSe nanocrystals (see Chapter 4). Three fixed emission frequencies are specified in the figure, corresponding to large (ω_L), medium (ω_M) and small (ω_S) nanocrystals.*

solution, possibly related to the reduced quantum efficiency. The reduction in quantum efficiency limits the degree of enhancement and inhibition observed. Nonetheless, the data in figure 5.4 demonstrate a strong variation in the lifetime by a factor of two for photonic crystals with different lattice parameters. These measurements are the first experimental demonstration of the use of photonic crystals to control the radiative lifetime of emitters.

A detailed study of the frequency dependence of the total decay rate has been carried out for crystals with many different lattice parameters, four of which are shown in figure 5.5. The total decay rate is the sum of the radiative and non-radiative decay rates. For each sample, we observe a variation of the total decay rate with emission frequency of more than 50%, which indicates that the radiative decay strongly depends on the emission frequency (see Chapter 4). For comparison, the solid curve in figure 5.5

shows the frequency-dependent decay rate for the nanocrystals in a homogeneous medium (γ_h), i.e., in solution. This curve was obtained by fitting the experimental data of figure 4.5 (c) with a phenomenological expression ($\Gamma = b \cdot \omega^n$), which yields n=3.8. The parameter b was adjusted to fit to the data on the reference sample with a lattice parameter a=370 nm. A surprisingly good agreement on the frequency increase in both media is observed, indicating that the quantum efficiency of the nanocrystals in the photonic crystal is high. A more sophisticated model for the emission of an ensemble of nanocrystals would require knowledge of the non-radiative contributions to the decay rate. Importantly, the non-radiative contributions are identical for each of the samples, as nanocrystals from the same preparation batch were used and all photonic crystals were fabricated under identical conditions. Therefore, variations between samples with different lattice parameters are due to changes in the radiative lifetime. We observe changes in the lifetime by up to a factor of two at a fixed frequency. For the photonic crystal with a=460 nm, a pronounced inhibition of the emission rate of 30% is observed in a wide bandwidth exceeding 10%. On the sample with a=420 nm, a strongly enhanced emission is measured, extending the decay rate by more than 40% relative to the reference value. The decay rates for the a=580 nm sample are all enhanced over a broad frequency range. These measurements demonstrate that photonic crystals offer an effective way of controlling the radiative lifetime through the lattice parameter a.

To compare experimental data on different samples mutually as well with theory, it is instructive to scale the emission frequency (ω) with the lattice parameter (a) and the speed of light in vacuum (c) according to $\widetilde{\omega} = \omega a/2\pi c (= a/\lambda)$. At fixed emission frequency ω, we compare nanocrystals of the same size and hence with identical emission properties. Figure 5.6 displays the measured total decay rate as a function of scaled frequency for three emission frequencies corresponding to large (ω_L), medium (ω_M) and small (ω_S) nanocrystals, as indicated in figure 5.5. The experimental data are compared to the calculated density of states (DOS). The DOS is the unit-cell averaged LDOS weighted by all Bloch mode functions, and approximates the LDOS well in the weak photonic limit $\widetilde{\omega} \ll 1$, where the DOS scales with ω^2 and where spatial variations are less pronounced. The data are compared to the DOS because it can readily be calculated, whereas

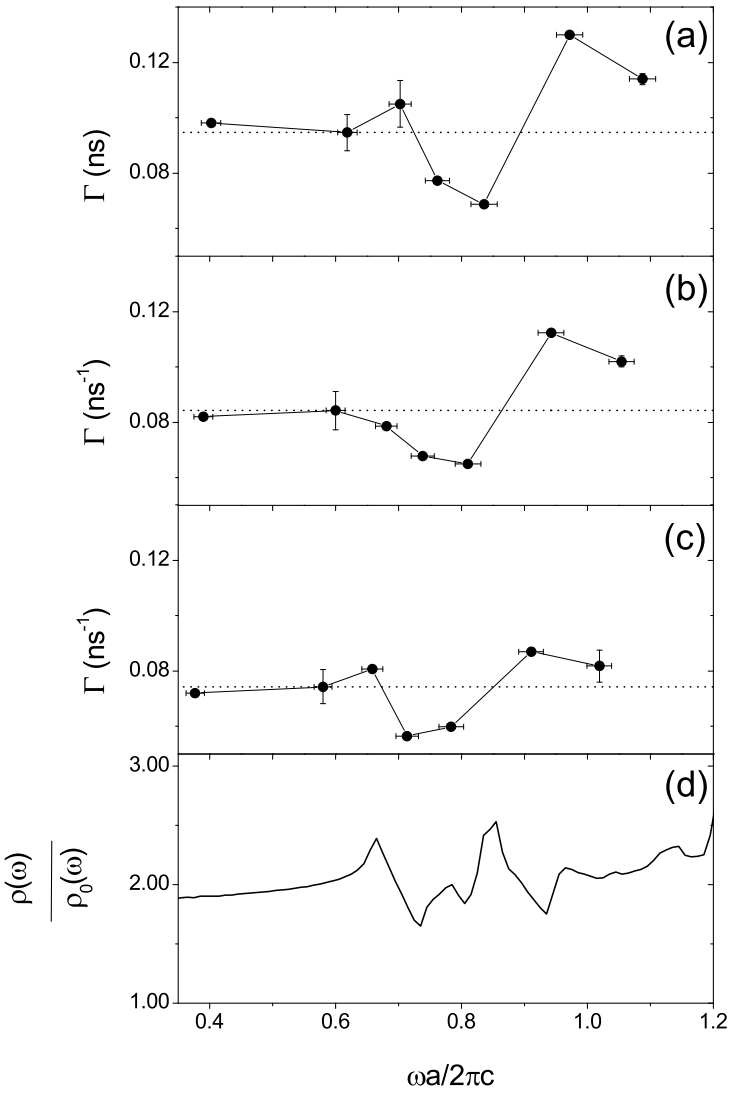

Figure 5.6: *Measured lifetimes of the excited states of CdSe nanocrystals in photonic crystals with different lattice parameters, corresponding to (a) large (ω_L), (b) medium (ω_M) and (c) small (ω_S) nanocrystals. The curve (d) is the calculated DOS for a titania inverse opal ($\rho(\omega)$) divided by the DOS for a homogeneous medium ($\rho_0(\omega)$). The horizontal dotted lines give the decay rate in a homogeneous medium (γ_h), corresponding to the solid curve in figure 5.5, and indicate the decay rate of emission in a reference crystal.*

an LDOS calculation is a formidable computational task [25] and existing calculations are currently under debate [26]. At low scaled frequencies ($\widetilde{\omega} < 0.65$), the photonic crystal is effectively a homogeneous medium, and we measure a non-photonic reference decay rate γ_h. As a is increased, the decay rate is reduced for all nanocrystal-sizes, and a broad band of inhibited emission is observed in agreement with previous continuous-wave measurements [27]. The inhibition is found in the pseudogap region where the DOS is strongly altered. The rapid drop in the measured decay rate is qualitatively described by the DOS. At even higher frequencies ($\widetilde{\omega} > 0.85$), the decay rates are strongly enhanced compared to the reference decay rate over a wide frequency range. In this range, the calculated DOS also reveals enhancements, but this is the strongly photonic regime where the DOS no longer provides an adequate description, and local variations described by the LDOS are crucial.

5.3.4 Time-resolved measurements: long time-scale analysis

The decay curves recorded on a longer time scale ($\sim$ 80 ns) are not single-exponential. However, in Chapter 4 it was shown that a suspended ensemble of nanocrystals, prepared by the same method as the nanocrystals used in this study, have a nearly single-exponential decay curve. Recently it was concluded that fluctuations in the environment surrounding the nanocrystals induce a broad distribution of non-radiative decay channels, explaining the absence of single exponential decay and effectively reducing the quantum efficiency [28]. It might be expected that this, if applicable to our samples, is the same in all samples; nanocrystals from the same synthesis batch were used and all photonic crystals were fabricated under identical conditions, resulting in identical chemical conditions in all our samples. Variations in the multi-exponential character of the decay curve of various samples therefore cannot be explained by a difference in chemical conditions.

The nanocrystals are distributed in the photonic crystal and will experience different LDOS. As a consequence of the different LDOS the nanocrystals will emit with a distribution of decay rates. We conclude that variation in the multi-exponential character of the decay curves is caused by variations in the LDOS.

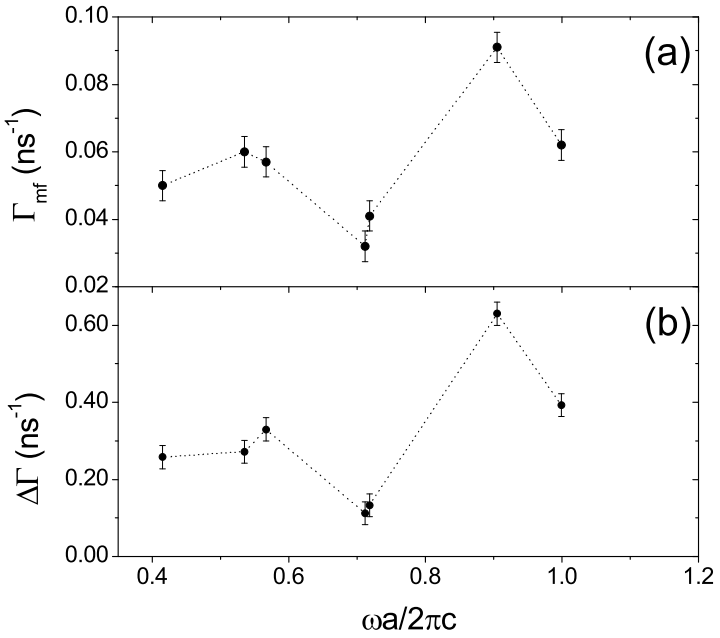

Figure 5.7: *Most frequent rate (Γ_{mf}) (a) and width of the decay rate distribution ($\Delta\Gamma$) (b) deduced from decay curves of CdSe nanocrystals in photonic crystals with different lattice parameters. A log-normal distribution of the rates was used, and Γ_{mf} and $\Delta\Gamma$ are defined by eqs. 5.3 and 5.4.*

Our multi-exponential decay curves were modelled with a distribution model (eqns. 5.2 and 5.3). In figure 3.4 (b) a luminescence decay curve of nanocrystals in a photonic crystal with a lattice parameter of a=340 nm is shown and the decay curve is modelled with a log-normal distribution of decay rates. Clearly, the log-normal model is in excellent agreement with our experimental decay curves. The most-frequent decay rate (Γ_{mf}) and the width of the distribution ($\Delta\Gamma$) were set as adjustable parameters. Eq. 5.5 shows that the width of the distribution is determined by the distribution of Γ_{rad} *and* by the distribution of Γ_{nrad}. In figure 5.7 Γ_{mf} and $\Delta\Gamma$ are plotted for photonic samples with various lattice parameters. The most frequent decay rate of the distribution can be compared with the decay rate deduced by single-exponential fitting of the initial part of the decay curves (figure 5.6 (a)-(c)). Clearly, both results show a good agreement. The procedures used to obtain the rates plotted in figures 5.6 and 5.7 are very different. To obtain the rates of figure 5.6 the first 20 ns of the multi-exponential decay curves were approximated by a single-exponential and for the rates plotted in figure 5.7 a multi-exponential function was used to model the decay curves over 80 ns. Despite the strong differences, good agreement in the results of the two procedures can be observed.

We observed strong variations in the width of the distribution. $\Delta\Gamma$ and Γ_{mf} show a similar trend with frequency, but the width shows a factor-of-six variation while the variation in the rate is about a factor of three. These variations are not related to chemical differences between the samples, and therefore we argue that this is caused by the variation in the LDOS. At frequencies around the L-gap ($\widetilde{\omega} \sim 0.8$) a suppression of the total DOS explains the observed minimum of $\Delta\Gamma$; the LDOS is also inhibited in most places of the unit-cell which are occupied by the nanocrystals, i.e., the internal surface of the air-sphere crystal. The width of 0.11 ns^{-1} is therefore identified with the distribution of non-radiative decay channels and is probably related to fluctuations in the vicinity of the individual nanocrystals [28]. The large width of 0.63 ns^{-1} at $\widetilde{\omega}$= 0.9 is thus largely determined by the distribution of radiative rates and is related to the broad spatial distribution of the LDOS at this frequency.

5.4 Conclusions

The optical properties of ZnSe-capped CdSe nanocrystals in titania inverse opal photonic crystals have been studied. With angle-dependent measurements it was shown that the spectral distribution is determined by the photonic crystal, confirming that emission of nanocrystals from the bulk of the photonic crystals was probed. Time-dependent measurement were successfully modelled with a log-normal distribution of the decay rate and showed for the first time that the radiative decay rate is controlled by the photonic crystal environment. Both enhanced and inhibited decay rates were observed, in agreement with density of states calculations. Furthermore, a six-fold variation of the decay rate distribution was observed and identified with the spatial variation of the local density of optical modes probed by the nanocrystals at various positions in the unit-cell. These results show that photonic crystals strongly modify the vacuum field, even in the absence of a photonic bandgap.

References

[1] C. Kittel, *Introduction to Solid State Physics*, 7th ed. (John Wiley & Sons, Inc., New York, 2004).

[2] V. P. Bykov, *Spontaneous emission from a medium with a band spectrum*, Soviet Journal of Quantum Electronics **4**, 861 (1975).

[3] E. Yablonovitch, *Inhibited spontaneous emission in solid-state physics and electronics*, Physical Review Letters **58**, 2059 (1987).

[4] C. M. Soukoulis, *Photonic Bandgap Materials* (Kluwer, Dordrecht, 1996).

[5] A. F. Koenderink, *Emission and Transport of Light in Photonic Crystals* (Ph.D. thesis, University of Amsterdam, Amsterdam, 2003).

[6] H. P. Schriemer, H. M. van Driel, A. F. Koenderink, and W. L. Vos, *Modified spontaneous emission spectra of laser dye in inverse opal photonic crystals*, Physical Review A **A63**, 011801 (2001).

[7] I. S. Nikolaev, P. Lodahl, and W. L. Vos, *Quantitative analysis of directional spontaneous emission spectra from light sources in photonic crystals*, Physical Review A **71**, 053813 (2005).

[8] S. Noda, K. Tomoda, N. Yamamoto, and A. Chutinan, *Full three-dimensional photonic bandgap crystals at near-infrared wavelengths*, Science **289**, 604 (2000).

[9] A. Blanco, E. Chomski, S. Grabtchak, M. Ibisate, S. John, S. W. Leonard, C. Lopez, F. Meseguer, H. Miguez, J. P. Mondia, G. A. Ozin, O. Toader, and H. M. van Driel, *Large-scale synthesis of a silicon photonic crystal with a complete three-dimensional bandgap near 1.5 micrometres*, Nature **405**, 437 (2000).

[10] Y. A. Vlasov, X. Z. Bo, J. C. Sturm, and D. J. Norris, *On-chip natural assembly of silicon photonic bandgap crystals*, Nature **414**, 289 (2001).

[11] R. Sprik, B. A. van Tiggelen, and A. Lagendijk, *Optical emission in periodic dielectrics*, Europhysics Letters **35**, 265 (1996).

[12] K. H. Drexhage, *Influence of a dielectric interface on fluorescence decay time*, Journal of Luminescence **1,2**, 693 (1970).

[13] S. Haroche, *Cavity quantum electrodynamics, Chapter 13 of Fundamental Systems in Quantum Optics* (Elsevier, North-Holland, Amsterdam, 1992).

[14] J. E. G. J. Wijnhoven and W. L. Vos, *Preparation of photonic crystals made of air spheres in titania*, Science **281**, 802 (1998).

[15] A. F. Koenderink, M. Megens, G. van Soest, W. L. Vos, and A. Lagendijk, *Enhanced backscattering from photonic crystals*, Physics Letters A **268**, 104 (2000).

[16] S. L. Cumberland, K. M. Hanif, A. Javier, G. A. Khitrov, G. F. Strouse, S. M. Woessner, and C. S. Yun, *Inorganic clusters as single-source precursors for preparation of CdSe, ZnSe, and CdSe/ZnS nanomaterials*, Chemistry of Materials **14**, 1576 (2002).

[17] S. A. Crooker, J. A. Hollingsworth, S. Tretiak, and V. I. Klimov, *Spectrally resolved dynamics of energy transfer in quantum-dot assemblies: Towards engineered energy flows in artificial materials*, Physical Review Letters **89**, 186802 (2002).

[18] S. Fery-Forgues and D. Lavabre, *Are fluorescence quantum yields so tricky to measure? A demonstration using familiar stationery products*, Journal of Chemical Education **76**, 1260 (1999).

[19] M. S. Thijssen, R. Sprik, J. E. G. J. Wijnhoven, M. Megens, T. Narayanan, A. Lagendijk, and W. L. Vos, *Inhibited light propagation and broadband reflection in photonic air-sphere crystals*, Physical Review Letters **83**, 2730 (1999).

[20] J. E. G. J. Wijnhoven, S. J. M. Zevenhuizen, M. A. Hendriks, D. Vanmaekelbergh, J. J. Kelly, and W. L. Vos, *Electrochemical assembly of ordered macropores in gold*, Advanced Materials **12**, 888 (2000).

[21] A. Lagendijk, R. Vreeker, and P. de Vries, *Influence of internal-reflection on diffusive transport in strongly scattering media*, Physics Letters A **136**, 81 (1989).

[22] J. X. Zhu, D. J. Pine, and D. A. Weitz, *Internal-reflection of diffusive light in random-media*, Physical Review A **44**, 3948 (1991).

[23] D. J. Durian, *Influence of boundary reflection and refraction on diffusive photon transport*, Physical Review E **50**, 857 (1994).

[24] A. F. Koenderink and W. L. Vos, *Light exiting from real photonic band gap crystals is diffuse and strongly directional*, Physical Review Letters **91**, 213902 (2003).

[25] K. Busch and S. John, *Photonic band gap formation in certain self-organizing systems*, Physical Review E **58**, 3896 (1998).

[26] R. Z. Wang, X. H. Wang, B. Y. Gu, and G. Z. Yang, *Local density of states in three-dimensional photonic crystals: Calculation and enhancement effects*, Physical Review B **67**, 155114 (2003).

[27] A. F. Koenderink, L. Bechger, H. P. Schriemer, A. Lagendijk, and W. L. Vos, *Broadband fivefold reduction of vacuum fluctuations probed by dyes in photonic crystals*, Physical Review Letters **88**, 143903 (2002).

[28] B. R. Fisher, H. J. Eisler, N. E. Stott, and M. G. Bawendi, *Emission intensity dependence and single-exponential behavior in single colloidal quantum dot fluorescence lifetimes*, Journal of Physical Chemistry B **108**, 143 (2004).

Chapter 6

Hot carrier luminescence during porous etching of GaP under high electric field conditions

abstract

Electroluminescence is observed during porous etching of n-type GaP single crystals at strongly positive potential. The emission spectra, which include a supra-band gap contribution, are markedly different from the spectra observed under optical excitation or minority carrier injection. The current density and electroluminescence intensity show a strong potential dependence and a similar hysteresis. The spectral characteristics of the luminescence suggest that both thermalised and hot charge carriers, generated by impact ionisation, are involved in light emission.

6.1 Introduction

Porous semiconductors with a high refractive index variation scatter light strongly. Various n-type III-V semiconductors, including InP, GaAs, GaP and GaN, can be made porous by electrochemical etching [1–7]. These materials have a large refractive index and a bandgap ranging from the near infrared to the ultra-violet [8]. Because of the large variations of the refractive index in porous III-V semiconductors light is strongly scattered and due to the large bandgap light is not absorbed. For example, figure 6.1 shows the absorption length (ℓ_a) and the refractive index (n) as a function of wavelength for bulk GaP. The first (indirect) bandgap of GaP is at 550 nm, where the refractive index is as high as 3.3 [9], much higher than that of liquids and solids like glass and NaCl which have a refractive index less than 2. Optimisation of the etching process of GaP has yielded the strongest random-scattering medium for visible light known to date [10]; a transport mean free path, which is defined as the ensemble averaged distance required to randomise the direction of propagation, as small as 0.17 μm was reported. There is evidence for Anderson localisation of light in this system [11] and anisotropic diffusion of light has been observed [12].

Besides refractive index variations, the size of the pores determines the strength of scattering. Rayleigh scattering occurs when the pore dimensions are much smaller than the wavelength of the scattered light. When the wavelength and the size of the scatterer are in the same range, one speaks of Mie scattering. Generally, Mie scattering is stronger than Rayleigh scattering. III-V semiconductors with pore dimensions in the 100-500 nm range, i.e. the Mie scattering regime, are therefore very promising materials for photonic applications.

It has been demonstrated that anodic etching can produce a two-dimensional array of ordered pores in InP [3]; this material, showing birefringence at wavelengths required for optical communication, can be easily integrated into opto-electronic systems. In contrast to the ordered pores in InP, anodic etching of n-type GaP gives random porous networks [2].

In view of the very interesting optical [3, 7, 10, 11, 13] and opto-electrical properties [13, 14] the mechanism of porous etching and the influence of the etching parameters on the morphology are important. Etching is generally carried out at strongly positive potentials corresponding to deep deple-

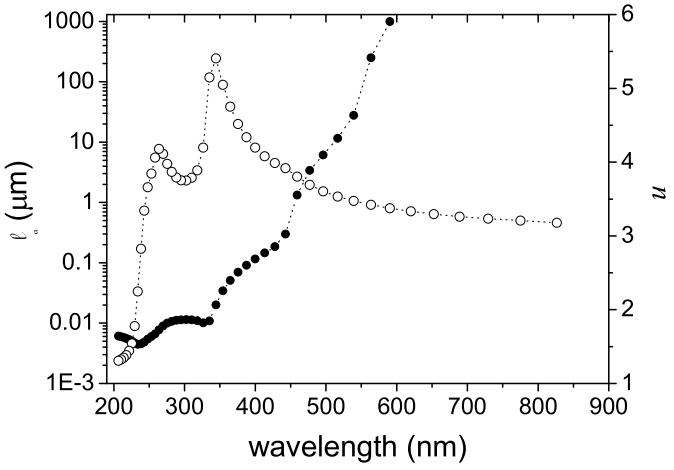

Figure 6.1: *Absorption length (filled dots, left axis) and refractive index (open dots, right axis) of bulk GaP as a function of the wavelength of light. Data were taken from Ref. [9].*

tion [2]. Various authors [15–19] have suggested that electrical breakdown leading to current flow is governed by the electric field of the space charge layer. This mechanism is similar to that proposed for electric breakdown in p-n junctions [20]. Tunnelling of electrons and avalanche multiplication are well known for strongly reverse-biased p-n junctions. In tunnelling-breakdown, an electron tunnels resonantly from the valence band to the conduction band. This process leaves a hole at the surface, which will lead to the dissolution of the semiconductor crystal. The electric field required for avalanche multiplication is usually not reached in high-doped ($>10^{17}$ cm^{-3}) semiconductors. As for low-doped p-n junctions, avalanche multiplication can occur in low-doped semiconductors, leading to strongly localised etch pits. Therefore, tunnelling is likely the most important mechanism for porous etching of n-type semiconductors.

In the present work we have investigated the relationship between the current density and potential for n-type GaP under strong depletion and passivating conditions in aqueous sulfiric acid (H_2SO_4) solution. We show that the dissolution current is due to field-dependent inter-band tunnelling. We have observed for the first time very characteristic light emission dur-

ing the etching process. Electroluminescence in GaP has been reported to occur both in forward- and reverse-biased p-n junctions [21–24], reverse-biased p-type electrodes [25] and n-type electrodes in the presence of a hole-injecting species, i.e., a strong oxidising agent [26]. Since GaP is an indirect bandgap semiconductor band-band emission is, except for isoelectronically doped material, very inefficient. At room temperature one generally observes only sub-bandgap emission due to electron-hole recombination via defect states, e.g., donor-acceptor pairs [26]. A similar emission spectrum, consisting of a broad band with a maximum at around 800 nm (1.55 eV) is also observed in room-temperature photoluminescence [26] and cathodoluminescence [27]. In our experiments with anodically etching GaP we find, surprisingly, not only the sub-bandgap luminescence but also relatively strong emission at higher energies; we observe a broad band extending well above the indirect bandgap. In the present Chapter we describe the influence of the parameters potential, current density and the porous layer thickness on the intensity, current efficiency and the spectral distribution of the luminescence. We show that this striking electroluminescence originates from the area of active etching and we speculate on the mechanism.

6.2 Experimental

For the experiments 300 μm thick n-GaP wafers, supplied by Groupe Arnaud Electronics and Grimet Ltd., with a (100) surface orientation and a dopant density of 7×10^{17}cm^{-3} or 10-20$\times10^{17}$cm^{-3}, respectively, were used. Pieces of approximately 6×6 mm were cut and glued on a copper plate with a conductive adhesive paste. A circular area of 0.13 cm^2 was exposed to the electrolyte by means of a Teflon sticker. Experiments were performed with the n-GaP working electrode (WE) in a three-electrode set-up, with a platinum counter electrode (CE) and a saturated calomel electrode (SCE) as reference (Ref) (figure 6.2). All experiments were performed in the dark, at room temperature in an aqueous 0.5 mol/l H_2SO_4 solution. The potential of the GaP working electrode was controlled by an EG&G PAR 273A potentiostat, which was programmed by a computer with home-made software. Luminescence spectra were recorded with a Princeton Instruments CCD

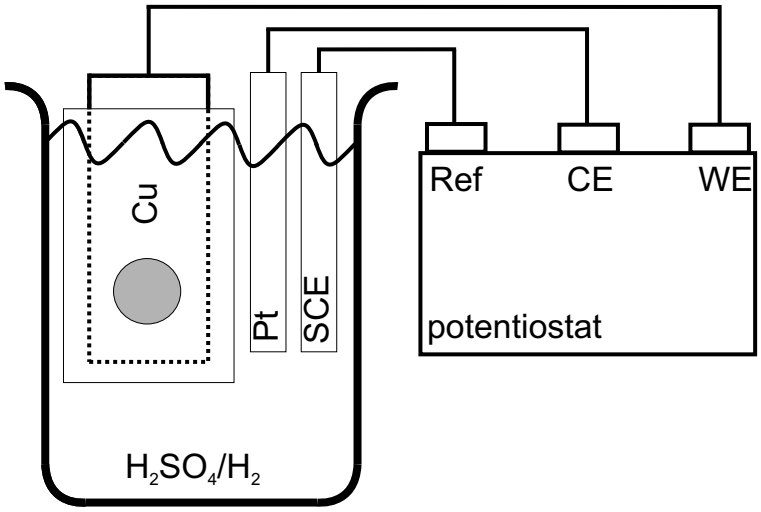

Figure 6.2: *Set-up for electrochemical experiments with a platimum counter electrode (CE), a saturated calomel reference electrode (SCE) and a working electrode (WE). In the unmasked (grey coloured) area of the copper GaP is exposed to the electrolyte solution.*

camera (liquid-nitrogen cooled, 1024×256 pixels) in combination with an Acton Pro monochromator (150 lines/mm, blazed at 500 nm).

6.3 Results

When a strong positive potential is applied to an n-GaP working electrode, a current starts to flow. Figure 6.3 shows a current density-time plot for the high-doped sample (10-20$\times 10^{17}$cm^{-3}) during the first 1000 s of porous etching at a potential of 7 V. Etching of the GaP crystal starts at t=0 s. In the initial stage the current rises rapidly; it reaches a constant value of about 13 mA/cm^2 after approximately 200 s. Previous studies have shown that dissolution starts at defect sites on the surface and that the pores have a diameter of around 100 nm [2, 28]. Here primary pores are formed from which multiple branching occurs, resulting in an increased active etching area and, consequently, in an increased current density. Figure 6.4 (a) shows a SEM picture of the branched structure which forms a hemispherical domain and grows isotropically (t$<$200 s, figure 6.3).

After some time the domains meet; this stabilises the active etching

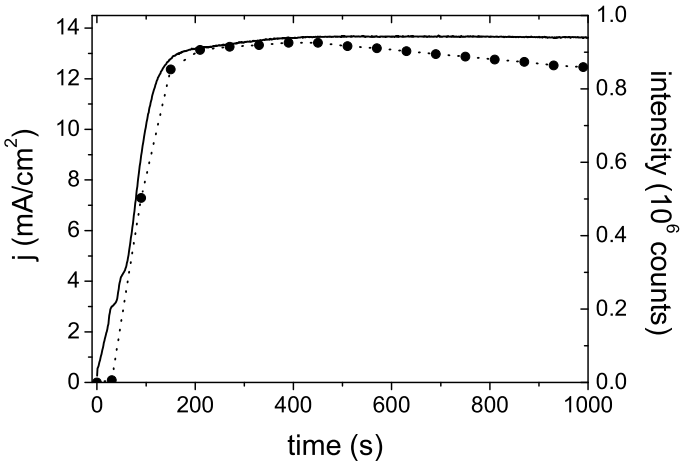

Figure 6.3: *Current density (solid line, left axis) and integrated luminescence intensity (filled dots, right axis) as a function of time for n-type GaP (dopant density 10-20×10^{17} cm^{-3}) during first 1000 s of porous etching at 7 V in aqueous 0.5 mol/l H_2SO_4 solution.*

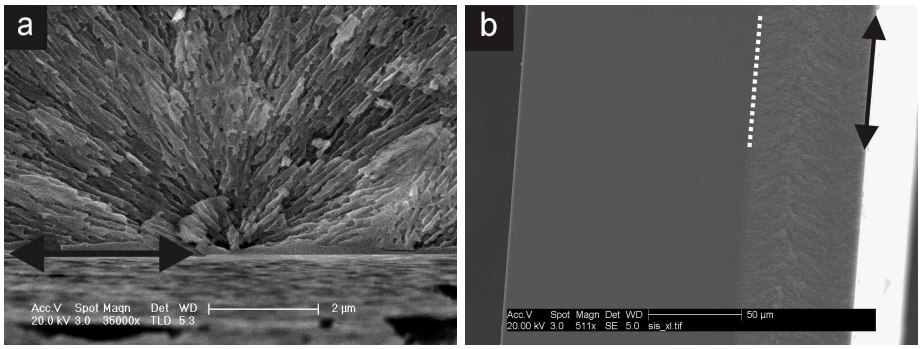

Figure 6.4: *Scanning electron microscopy (SEM) picture of a cros-sectioned GaP wafer after etching at 13.5 V (dopant density 7×10^{17} cm^{-3}). (a) Etching starts at the electrolyte|GaP interface (black arrows) where porous hemispheres are formed. (b) After the hemispherical domains meet, the porous|non-porous interface (white dotted line) moves in a direction perpendicular to the surface.*

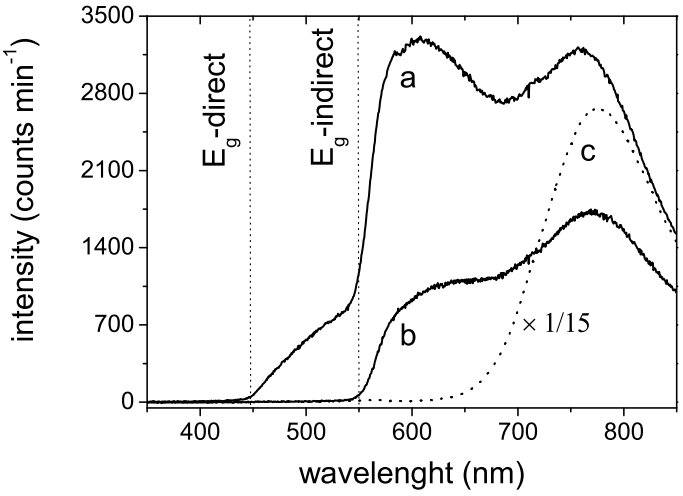

Figure 6.5: *Luminescence spectra of n-type GaP (dopant density 10-20×10^{17} cm^{-3}) after 450 s (a) and 10230 s (b) of porous etching at 7 V in aqueous 0.5 mol/l H_2SO_4 solution. A luminescence spectrum (c) of n-type GaP (dopant density 10-20×10^{17} cm^{-3}) at negative potential in aqueous 20 mmol/l $(NH_4)S_2O_8$-0.5 mol/lH_2SO_4 solution is shown for comparison.*

front and the anodic current becomes constant. From this moment the porous layer, having a uniform thickness, grows at a constant rate in a direction perpendicular to the surface (see figure 6.4 (b)). Surprisingly, light emission was observed during porous etching when the potential was sufficiently positive. A faint and uniform emission of light was visible to the naked eye. Luminescence spectra were recorded every 60 s using an exposure time of 60 s. In figure 6.3, the integrated luminescence intensity in the range between 350 and 880 nm is plotted together with the current density as a function of time. Clearly, the luminescence is correlated with the anodic current; both increase in a similar way. From this and results shown below we conclude that the luminescence arises from the active etching area, i.e., the pore fronts. After 450 s the recorded luminescence intensity gradually starts to decrease, while the anodic current density remains constant. This is due to the growth of the porous layer, located between the light emitting area and the detector; light is scattered and/or absorbed by the porous layer.

Figure 6.5, curve (a) shows a spectrum which was recorded after 450 s while the current was constant but the porous layer was too thin to scatter light significantly. Quite remarkably, a large fraction of the emitted light has an energy close to and larger than the indirect bandgap, indicated by a dotted line in figure 6.5.

The spectral distribution in figure 6.5, curve (a) is quite different from that measured during other luminescence measurements. In a conventional photoluminescence experiment at ambient temperature only sub-bandgap emission was observed [26, 29]. A spectrum similar to the reported photoluminescence spectra was observed during electroluminescence with an aqueous solution of peroxydisulfate ($(NH_4)S_2O_8$), in which holes are injected into the valence band of GaP at negative potential, as shown in figure 6.5, spectrum (c). This process is about 15 times more efficient than emission observed during porous etching. The broad peak at around 800 nm, also observed in cathodoluminescence [27], is attributed to radiative recombination via a donor-acceptor pair in the bandgap [26, 27]. However, between 450 nm and 700 nm a very striking additional supra-bandgap contribution to the spectrum is observed during porous etching.

Supra-bandgap emission is also observed in microporous silicon and is related to quantum confinement effects [30]. The broad supra-bandgap emission in the visible range can be excited either by light (photoluminescence) [30] or electrochemically [31]. The observation of only low-energy defect related emission from our porous GaP in both photoluminescence [26] and hole-injection experiments shows that nanostructures, i.e., quantum confinement effects, cannot be responsible for the short-wavelength emission seen in figure 6.5 (a).

The sharp decrease of the intensity with increasing energy near 550 nm (2.25 eV) seen in spectrum (a) of figure 6.5 is related to the indirect bandgap of GaP at this energy. The absorption length of light in this range decreases strongly from 250 μm at 2.2 eV (564 nm) to 0.3 μm at 2.8 eV (443 nm) [9]. Therefore, light with an energy above the bandgap will be strongly absorbed, giving rise to a abrupt decrease of the luminescence intensity. Furthermore, light with a small absorption length can be observed only when it is emitted in the direction of the detector. Light with a very large absorption length can eventually reach the detector after being internally

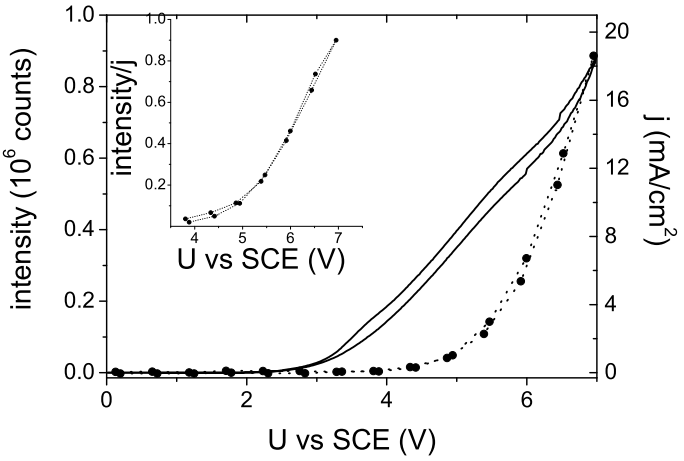

Figure 6.6: *Current density (solid line, right axis) and integrated luminescence intensity (filled dots, left axis) as a function of potential for porous n-type GaP (dopant density 10-20×10^{17} cm^{-3}). The measurement was done after 10^4 s of porous etching at 7 V in aqueous 0.5 mol/l H_2SO_4 solution. The potential was scanned at a rate of 25 mV/s. Inset: Normalised ratio of the integrated luminescence intensity and the current density as a function of the potential.*

reflected inside the crystal or at the backside of the crystal. These two effects explain the 'step' observed at around 550 nm in figure 6.5, spectrum (a). It is furthermore clear that, after prolonged etching, the detected intensity decreases (figure 6.5, spectrum (b)) while the anodic current density remains constant. The supra-bandgap contribution is no longer recorded. This is due to scattering and absorption of the emitted light by the porous GaP layer. Light with energy above the bandgap is strongly scattered and, eventually, absorbed. Light with an energy below the bandgap is only scattered. Absorption and scattering of light in the porous layer can therefore partly explain the spectral distribution and the change of the spectrum with time, i.e., with porous layer thickness.

To obtain a better understanding of the origin of the luminescence, spectra were recorded while the potential of n-type GaP electrodes was scanned in the range in which porous etching occurs. We used GaP electrodes on which a thick porous layer (L $>$ 80 μm) had been grown. This ensures that the relative increase in the thickness of the porous layer during the scan

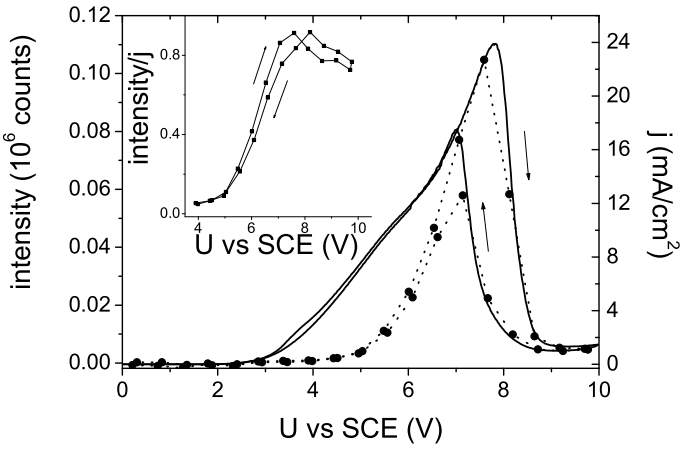

Figure 6.7: *Current density (solid line, right axis) and integrated luminescence intensity (filled dots, left axis) as a function of potential for porous n-type GaP (dopant density 10-20$\times 10^{17}$ cm^{-3}). The measurement was done after 10^4 s of porous etching at 7 V in aqueous 0.5 mol/l H_2SO_4 solution. The potential was scanned at a rate of 25 mV/s. Inset: Normalised ratio of the integrated luminescence intensity and the current density as a function of the potential.*

of the potential, and thus additional absorption/scattering, can be disregarded. A scan rate of 25 mV/s was used and a spectrum was recorded every 20 s (with an exposure time of 20 s). We remark that the recorded spectra are similar to spectrum (b) of figure 6.5 and that the supra-bandgap contribution is absorbed. Under these conditions the spectral distribution did not depend on the applied potential. Experiments with a GaP electrode with a very thin porous layer on the top showed that the ratio of the supra-bandgap and the sub-bandgap luminescence intensity did not depend on the applied potential. In figure 6.6 the current density (right axis) and the integrated luminescence intensity, between 550 and 880 nm (left axis), are plotted as a function of the applied potential. There is only a slight hysteresis in the current density when the potential is scanned to 7 V. The luminescence sets on at a potential 2 V more positive than the current density. The luminescence intensity increases rapidly with the applied potential.

It is known that at more positive potentials n-type GaP passivates in H_2SO_4 solution. The influence of passivation is illustrated in figure 6.7.

The current density in the forward scan shows a maximum at 7.8 V and decreases steeply above this potential as a result of passivation of the pore fronts by an oxide layer [28]. In the return scan, the current recovers slowly due to chemical dissolution of the oxide. This slow dissolution is responsible for the considerable hysteresis in the current density. The onset of the luminescence is at a higher potential than that of the current. A considerable hysteresis is also observed in the intensity-potential curve. This again shows that the process of light emission is generated by current flow at the pore fronts. A measure for the relative efficiency of the luminescence can be obtained by dividing the integrated intensity by the current density (insets of figures 6.6 and 6.7). Below $\sim$4 V the current density is close to zero and the efficiency cannot be estimated with a sufficient accuracy. Above 4 V the luminescence efficiency increases rapidly with increasing potential. The inset of figure 6.7 shows that the efficiency decreases slightly when a passivating oxide layer is formed (U $>$ 8 V). The luminescence efficiency does not depend on the scan direction. This confirms that, with a thick porous layer, further growth of the layer during a scan of the potential does not significantly affect the recorded luminescence. Thus, figures 6.6 and 6.7 give a reliable representation of the potential dependence of the luminescence intensity.

6.4 Discussion

The electroluminescence observed during porous etching of n-type GaP at strongly positive potentials is clearly related to the anodic current originating from the pore fronts. Current flow in the reverse-biased junction must be due to breakdown of the depletion layer. This should depend on the electric field within the space-charge layer of the semiconductor. Impedance measurements by Erné et al. [2] on both porous and non-porous n-type GaP in H_2SO_4 solution showed that the depletion layer capacitance obeys the Mott-Schottky relation for potentials up to 9 V. This means that, in this range, a change in the applied potential results *only* in a change in the potential drop within the semiconductor. Since the flat-band potential is known for the system (-1.2 V versus SCE [2, 32]) the band bending can be determined for any value of the applied potential. At strong band bending

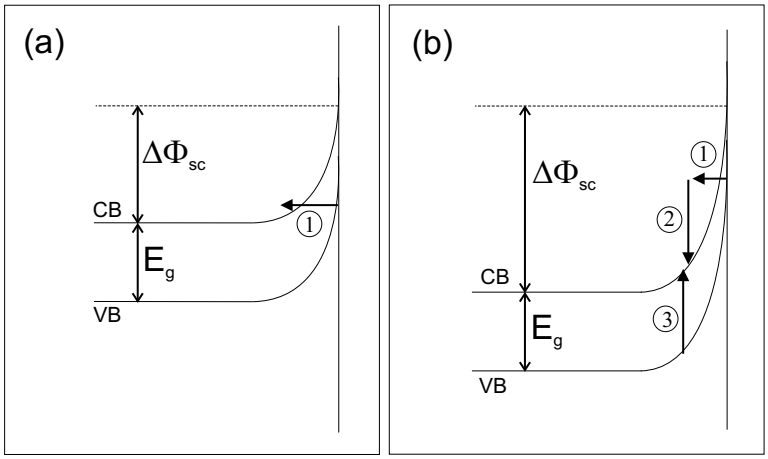

Figure 6.8: *Model for interband tunnelling (step 1) and impact ionisation (steps 2 and 3) for two different values of the potential drop ($\Delta\Phi_{sc}$) over the semiconductor. $\Delta\Phi_{sc}$ is larger in case of figure b.*

empty states in the conduction band 'overlap' with filled states at the top of the valence band at the surface. As a result, electrons can tunnel from the valence band to the conduction band (step 1, figure 6.8). The electrons are detected as current in the external circuit. The holes generated in the valence band serve to oxidise the semiconductor, thus causing porous etching [2]. The onset of the current, shown in a semi-logarithmic plot in figures 6.9 (a) and (b), corresponds to a band bending of about 3 and 3.5 eV for the high- and low-doped electrodes, respectively. A relation between the current density due to inter-band tunnelling and the electric field, which was first proposed by Zener [33] and extended for large bandgap semiconductors by McAfee et al. [34], is given by:

$$j \propto E \exp(\alpha - \frac{\beta}{E}) \tag{6.1}$$

where α is a parameter related to the semiconductor and is not relevant here, and E is, in our case, the electric field at the surface of the GaP electrode. The electric field was deduced by using an equation which relates the dopant density, the applied potential and the radius of the pores tip, as reported in Ref. [35]. The value of parameter β is given by the following

equation:

$$\beta = \frac{\pi^2}{eh}(2m^*)^{1/2}E_g^{3/2} = 1.2 \times 10^{10}\, V/m \tag{6.2}$$

where h is Planck's constant, e the electron charge, m^* is the effective electron mass [36] and E_g the bandgap. If it is assumed that the pore fronts are hemispherical, then the electric field at the surface of the pore fronts can be calculated [17, 35]. In figure 6.10 the logarithm of the current is plotted versus the inverse of the electric field at the tip of the pores and according to eq. 6.1 this should yield a straigth line. By modelling the field dependence of the measured current with eq. 6.1, β-values of 5×10^9 and 3×10^9 V/m are found for the high- and the low-doped wafers, respectively. The reasonable agreement between the values of β calculated on the basis of a hemispherical pore front and the value predicted by theory (eq. 6.2) support a Zener-type mechanism for current and pore formation.

Tunnelling of electrons from the valence band to the conduction band alone cannot explain light emission during anodic etching. While the hole concentration at the surface may be high, the electron concentration is extremely low due to the very high electric field. Furthermore, the onset of luminescence is at a potential of about 2 V more positive than the onset of the current (figure 6.9).

Electroluminescence has been observed in reverse-biased p-n junctions based on GaP [22–24, 37] and the GaAsP [21] ternary system. The mechanism proposed for light emission in this case is impact ionisation [38]. A similar process is very likely also responsible for luminescence in our reverse-biased n-type electrodes. Electrons injected into the conduction band are accelerated toward the bulk by the high electric field of the depletion layer. If the electron can gain more energy than that of the bandgap before it loses energy via excitation of optical phonons, it can excite a valence band electron over the bandgap (steps 2 and 3 in figure 6.8). The electron which is created by impact ionisation can in turn pick up energy from the field. This can give rise to an avalanche process with current multiplication [20]. Since the band bending in our case is rather low compared to that reported for p-n junctions [23], an avalanche process is unlikely. The threshold electric field for impact ionisation is, to a first approximation,

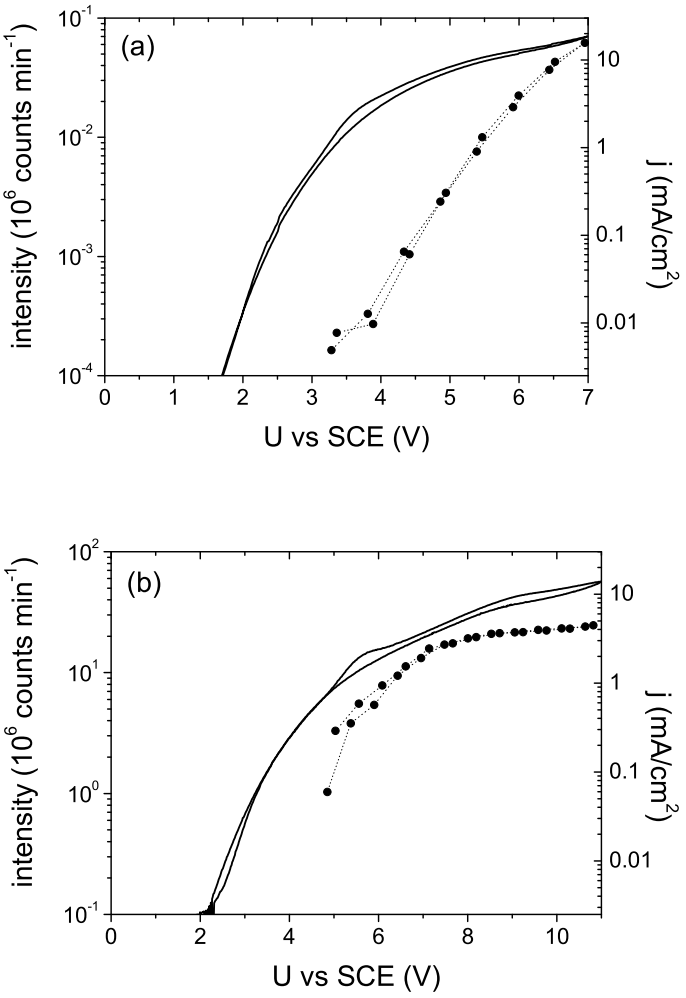

Figure 6.9: *Current density (solid line, right axis) and integrated luminescence intensity (filled dots, left axis) as a function of potential for porous n-type GaP with dopant density 10-20×10^{17} cm^{-3} (a) and 7×10^{17} cm^{-3} (b). The measurement was done after 10^4 s of porous etching at 7 (a) and 11 V (b) in aqueous 0.5 mol/l H_2SO_4 solution. The potential was scanned at a rate of 25 mV/s. (Figure 6.9 (a): data from figure 6.6 in a semi-logarithmic plot).*

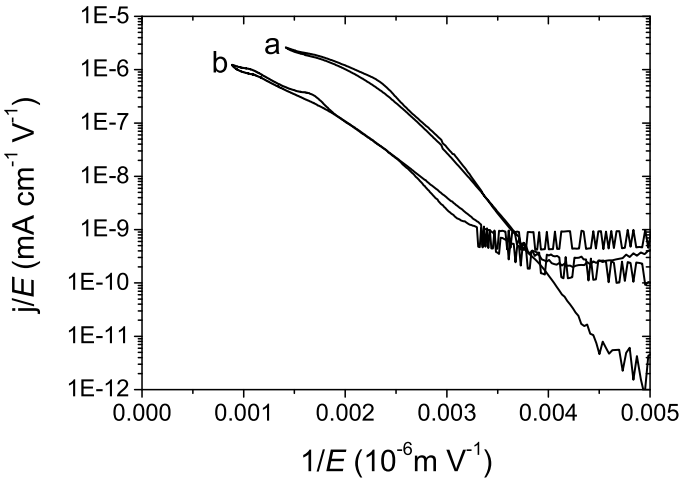

Figure 6.10: *Current density divided by the electric field (j/E) as a function of the inverse of the electric field ($1/E$) for high-doped wafer (10-20$\times 10^{17}$ cm^{-3}, curve a) and low-doped wafer (7$\times 10^{17}$ cm^{-3}, curve b). Results are plotted according to eq. 6.1.*

given by

$$E_{th} = \frac{3E_g}{2\lambda} \tag{6.3}$$

where E_{th} is the threshold field, λ is the optical phonon mean free path [39]; for GaP, λ is 3.0 nm [39] and thus the threshold field is 1×10^9 V/m. The electric field at the surface of a hemispherical pore is of this order of magnitude and impact ionisation can therefore be expected in our system. The probability of impact ionisation increases rapidly with increasing electric field at the surface [39]. This explains the increase in luminescence efficiency as the potential is raised (inset of figure 6.6). The electric field at the surface of the pore fronts decreases when passivation occurs; a part of the applied potential drops over the oxide layer. This reduces the efficiency of the luminescence, as is observed in the inset of figure 6.7.

Hole injection from an oxidising agent under forward-bias (figure 6.5, spectrum (c)) and optical excitation at room temperature [26] give a broad emission band that is similar to the band at about 770 nm observed at strongly positive potentials in this work (figure 6.5). This emission can be attributed to radiative recombination of thermalised electrons and holes

via defect states [26]; in this case the charge carriers are in quasi equilibrium. In contrast, the high-energy contribution of the observed spectrum with a significant supra-bandgap shoulder (450 nm $< \lambda <$ 550 nm) must be related to the relaxation of hot charge carriers formed at severe band bending (U $>$ 4V). Similar features have been observed in strongly reverse-biased GaP [22–24, 37] and ternary GaAsP [21] p-n junctions and reverse-biased p-GaP electrodes [25]. Very localised emission spots, occurring at imperfections in the junction, were observed when breakdown was due to avalanche multiplication. A uniform and faint light emission was observed in junctions where the current was caused by impact ionisation [40]. In the present work emission is triggered at the pore fronts where the electric field is greatly enhanced; as a result, luminescence is observed at considerably more modest bias than that required for a good-quality p-n junction. The emission sets on at the direct bandgap of GaP (figure 6.5, spectrum (a)), as observed for GaAsP in reference [21] and for GaP in Refs. [23, 25]. The supra bandgap emission can be due to recombination of holes with electrons in the conduction band minimum corresponding to the first direct bandgap, i.e., the Γ-point [41]. We conjecture that this conduction band minimum can be populated under high field conditions [20]. Radiative recombination between the conduction band minimum at the X-point and the maximum of the valence band at the Γ-point is indirect and therefore is less efficient [21]. Besides radiative recombination between electrons and holes which are separated by the direct bandgap, the onset of the luminescence intensity at the direct bandgap can also be related to absorption of light. The absorption length strongly decreases with wavelength in this spectral region (figure 6.1). Therefore, it is possible that emitted light with an energy even higher than the direct bandgap cannot be recorded because of absorption in GaP. It is not clear how the two possible origins of the onset of the luminescence at the direct bandgap, i.e., absorption and recombination between carriers which are separated by the direct bandgap, can be distinguished experimentally.

6.5 Conclusion

It is clear from the above results and discussion that generation of minority carriers, which is essential for light emission, is made possible by the very strong electric field of the depletion layer at the pore fronts. During porous etching of n-type GaP at strongly positive potentials a light source, consisting of a collection of emitting sites, is created at the interface between porous and non-porous GaP. We propose that recombination of charge carriers, generated by impact ionisation, is responsible for the observed luminescence. The light source, which has a broad spectrum ranging from violet to near-infrared, moves with the interface as the porous layer thickens; it can therefore be used to study light scattering in this strongly scattering porous medium, as will be shown Chapter 7.

References

[1] J. J. Kelly and D. Vanmaekelbergh, *Porous etched semiconductors; formation and characterization, Chapter 4 of The Electrochemistry of Nanomaterials* (Wiley-VCH, Weinheim (Germany), 2001).

[2] B. H. Erné, D. Vanmaekelbergh, and J. J. Kelly, *Morphology and strongly enhanced photoresponse of GaP electrodes made porous by anodic etching*, Journal of the Electrochemical Society **143**, 305 (1996).

[3] T. Takizawa, S. Arai, and M. Nakahara, *Fabrication of vertical and uniform-size porous InP structure by electrochemical anodization*, Japanese Journal of Applied Physics Part 2-Letters **33**, L643 (1994).

[4] S. Langa, I. M. Tiginyanu, J. Carstensen, M. Christophersen, and H. Foll, *Formation of porous layers with different morphologies during anodic etching of n-InP*, Electrochemical and Solid State Letters **3**, 514 (2000).

[5] P. Schmuki, J. Fraser, C. M. Vitus, M. J. Graham, and H. S. Isaacs, *Initiation and formation of porous GaAs*, Journal of the Electrochemical Society **143**, 3316 (1996).

[6] G. Oskam, A. Natarajan, P. C. Searson, and F. M. Ross, *The formation of porous GaAs in HF solutions*, Applied Surface Science **119**, 160 (1997).

[7] X. L. Li, Y. W. Kim, P. W. Bohn, and I. Adesida, *In-plane bandgap control in porous GaN through electroless wet chemical etching*, Applied Physics Letters **80**, 980 (2002).

[8] F. Schuurmans, *Light in Complex Dielectrics* (University of Amsterdam, Amsterdam, 1999).

[9] D. E. Aspnes and A. A. Studna, *Dielectric functions and optical parameters of silicon, germanium, gallium phosphide, gallium arsenide, gallium antimonide, indium phosphide, indium arsenide, and indium antimonide from 1.5 to 6.0 eV*, Physical Review B **27**, 985 (1983).

[10] F. J. P. Schuurmans, M. Megens, D. Vanmaekelbergh, and A. Lagendijk, *Light scattering near the localization transition in macroporous GaP networks*, Physical Review Letters **83**, 2183 (1999).

[11] F. J. P. Schuurmans, D. Vanmaekelbergh, J. van de Lagemaat, and A. Lagendijk, *Strongly photonic macroporous gallium phosphide networks*, Science **284**, 141 (1999).

[12] P. M. Johnson, B. P. J. Bret, J. Gómez Rivas, J. J. Kelly, and A. Lagendijk, *Anisotropic diffusion of light in a strongly scattering material*, Physical Review Letters **89**, 243901 (2002).

[13] E. Kikuno, M. Amiotti, T. Takizawa, and S. Arai, *Anisotropic refractive-index of porous InP fabricated by anodization of (111)a surface*, Japanese Journal of Applied Physics Part 1-Regular Papers Short Notes & Review Papers **34**, 177 (1995).

[14] B. H. Erné, D. Vanmaekelbergh, and J. J. Kelly, *Porous etching - A means to enhance the photoresponse of indirect semiconductors*, Advanced Materials **7**, 739 (1995).

[15] M. Theunissen, *Etch channel formation during anodic dissolution of n-type silicon in acqueos hydrofluoric acid*, Journal of the Electrochemical Society **119**, 351 (1972).

[16] M. I. J. Beale, J. D. Benjamin, M. J. Uren, N. G. Chew, and A. G. Cullis, *An experimental and theoretical study of the formation and microstructure of porous silicon*, J. Cryst. Growth **73**, 622 (1985).

[17] X. G. Zhang, *Mechanism of pore formation on n-type silicon*, Journal of the Electrochemical Society **138**, 3750 (1991).

[18] P. C. Searson, J. M. Macaulay, and F. M. Ross, *Pore morphology and the mechanism of pore formation in n-type silicon*, Journal of Applied Physics **72**, 253 (1992).

[19] V. Lehmann, R. Stengl, and A. Luigart, *On the morphology and the electrochemical formation mechanism of mesoporous silicon*, Materials Science and Engineering B-Solid State Materials for Advanced Technology **69**, 11 (2000).

[20] S. M. Sze, *Physics of Semiconductor Devices*, 2nd ed. (Wiley-Interscience, Murray Hill, 1981).

[21] M. Pilkuhn and H. Rupprecht, *Electroluminescence and lasing action in GaAsxP1-x*, J. Appl. Phys. **36**, 684 (1965).

[22] H. C. Gorton, J. M. Swartz, and C. S. Peet, *Radiative recombination in gallium phosphide point-contact diodes*, Nature **188**, 303 (1960).

[23] M. Gershenzon and R. M. Mikulyak, *Electroluminescence at p-n junctions in gallium phosphide*, J. Appl. Phys. **32**, 1338 (1961).

[24] F. G. Ullman, *Electroluminescence of gallium phosphide crystals*, Nature **190**, 161 (1961).

[25] M. A. Butler and D. S. Ginley, *Electrochemical light-emitting diodes*, Applied Physics Letters **36**, 845 (1980).

[26] B. Smandek and H. Gerischer, *Spectral dependence of photo- and electroluminescence on minority carrier concentration in the n-type gallium phosphide/electrolyte system*, Electrochim. Acta **30**, 1101 (1985).

[27] M. A. Stevens-Kalceff, I. M. Tiginyanu, S. Langa, H. Foll, and H. L. Hartnagel, *Correlation between morphology and cathodoluminescence in porous GaP*, Journal of Applied Physics **89**, 2560 (2001).

[28] R. W. Tjerkstra, J. Gómez Rivas, D. Vanmaekelbergh, and J. J. Kelly, *Porous GaP multilayers formed by electrochemical etching*, Electrochemical and Solid State Letters **5**, G32 (2002).

[29] A. Meijerink, A. A. Bol, and J. J. Kelly, *The origin of blue and ultraviolet emission from porous GaP*, Applied Physics Letters **69**, 2801 (1996).

[30] A. G. Cullis, L. T. Canham, and P. D. J. Calcott, *The structural and luminescence properties of porous silicon*, Journal of Applied Physics **82**, 909 (1997).

[31] E. S. Kooij, A. R. Rama, and J. J. Kelly, *Infrared induced visible emission from porous silicon: The mechanism of anodic oxidation*, Surface Science **370**, 125 (1997).

[32] F. Cardon and W. P. Gomes, *On the determination of the flat-band potential of a semiconductor in contact with a metal or an electrolyte from the Mott-Schottky plot*, Journal of Physics D-Applied Physics **11**, L63 (1978).

[33] C. Zener, *Theory of the electrical break-down of solid dielectrics*, Proceedings of the Royal Society of London **A145**, 523 (1934).

[34] K. B. McAfee, E. J. Ryder, W. Shockley, and M. Sparks, *Observations of Zener current in germanium p-n junctions*, Physical Review **83**, 650 (1951).

[35] X. G. Zhang, *Morphology and formation mechanisms of porous silicon*, Journal of the Electrochemical Society **151**, C69 (2004).

[36] G. Burns, *Solid State Physics*, international ed. (Academic Press, Orlando, Florida, 1985).

[37] G. A. Wolff, R. A. Hebert, and J. D. Broder, *Electroluminescence of gallium phosphide*, Phys. Rev. **100**, 1144 (1955).

[38] J. I. Pankove, *Optical Processes in Semiconductors* (Dover Publications, Inc., New York, 1975).

[39] Y. Okuto and C. R. Crowell, *Energy-conservation considerations in the characterization of impact ionization in semiconductors*, Phys. Rev. B **6**, 3076 (1972).

[40] S. Mahadevan, S. M. Hardas, and G. Suryan, *Electrical breakdown in semiconductors*, Phys. Status Solidi A **8**, 335 (1971).

[41] J. R. Chelikowsky and M. L. Cohen, *Nonlocal pseudopotential calculations for the electronic structure of eleven diamond and zinc blende semiconductors*, Phys. Rev. B **14**, 556 (1976).

Chapter 7

Electroluminescence as light source for an *in-situ* optical characterisation of macroporous GaP

abstract

During porous etching of GaP, electroluminescence ranging from the ultraviolet to the near-infrared is generated at the interface of the porous and the non-porous layer. This is used to measure the wavelength-dependent transmission of light through growing porous layers in a wide thickness range. Two types of porous structures, characterised by different pore sizes, were studied. The transmission of the emitted light gives valuable information about wavelength-dependent diffusion of light through porous GaP. The transport mean free path is deduced for the complete wavelength range.

7.1 Introduction

InP [1], GaAs [2] and GaP [3] can be made porous via electrochemical etching. Depending on the semiconductor and the etching conditions, the structure of the porous layer can be tuned. GaP etched in aqueous sulfuric acid solutions has a random interconnected structure. Porous multilayers in GaP, with alternating porosity, can be formed by etching with alternating potential [4]. It was furthermore shown that the structure of porous GaP is determined by the dopant density of the crystal [5].

Porous GaP is the strongest scattering material for visible light reported to date [6]. The scattering-strength can be further increased by increasing the diameter of the pores. Larger pores can be grown using GaP with a lower dopant density [5] and by applying a (photo)chemical dissolution process after electrochemical growth of the pores [6]. The increase of the pore size with decreasing dopant density can be understood on the basis of the breakdown model developed by Beale et al. [7]. Passivation of GaP crystals with a low dopant density occurs at a higher potential. Therefore, porosification of a low-doped crystal can be carried out at a higher potential. At higher potential larger pores are formed and, as a consequence, in low-doped crystals the pores have a larger diameter than in high-doped materials. Therefore, porous GaP grown from low-doped crystals scatters light more strongly.

The transmission of light through porous GaP layers has been studied extensively [6]. In the experiments reported in Ref. [6] several porous layers were etched separately. The transmission of the porous layers was subsequently measured as a function of thickness, to obtain the transport mean free path (ℓ). A values of 0.47 μm was measured for the porous GaP. Subsequent photo-chemical etching of the porous layer resulted in a decrease of the transport mean free path to 0.17 μm. Deducing the transport mean free path in this way requires several separately etched porous GaP layers. In this Chapter we propose a simple alternative method, in which the optical properties of the porous layer are measured *in-situ*, i.e., during etching, in a single experiment and over a wide thickness range.

In the Chapter 6 it was shown that during etching of GaP under strongly anodic conditions hot carrier luminescence is generated at the interface between the porous and the non-porous material [8]. A broad spectrum, in-

cluding a supra-bandgap contribution, was observed. The luminescence was attributed to recombination of electron-hole pairs generated by impact ionisation. This light source moves with the porous|non-porous interface as the porous layer thickens. This means that the transmission of the emitted light through a porous layer can be measured as a function of the thickness of the porous layer. This offers a unique possibility to study the transport of light through the growing random porous GaP layer.

In this Chapter we first consider the electrochemical results and the luminescence spectra. The intensity of the emission at various wavelengths is shown as a function of the porous layer thickness. We deduce the wavelength dependent transport mean free path over the complete visible range in a single experiment. This approach provides a very interesting and new method to characterise porous GaP.

7.2 Experimental

For the experiments 300 μm thick n-GaP wafers, supplied by Groupe Arnaud Electronics and Hewlett Packard, with a (100) surface orientation and a dopant density of 10-20$\times 10^{17}$ cm^{-3} and 7$\times 10^{17}$ cm^{-3}, respectively, were used. Pieces of approximately 6$\times$6 mm were cut and glued on a copper plate with a conductive adhesive paste. A circular area of 0.13 cm^2 was exposed to the electrolyte by means of a Teflon sticker. Experiments were performed with the n-GaP working electrode (WE) in a three-electrode set-up, with a platinum counter electrode and a saturated calomel electrode (SCE) as reference (figure 7.1 and 6.2). All experiments were performed in the dark, at room temperature in an aqueous 0.5 mol/l H_2SO_4 solution. The potential of the GaP working electrode was controlled by an EG&G PAR 273A potentiostat, which was programmed by a computer with home-made software.

Emission from the GaP surface that was exposed to the electrolyte solution was collected in a cone with an angle of $\sim 20^\circ$ around the central detection angle and focussed with a lens on the circular entrance of a CCD camera with an area of 8×10^{-3} cm^2. Luminescence spectra were recorded with a Princeton Instruments CCD camera (liquid-nitrogen cooled, 1024$\times$256 pixels) in combination with an Acton Pro monochromator (150 lines/mm,

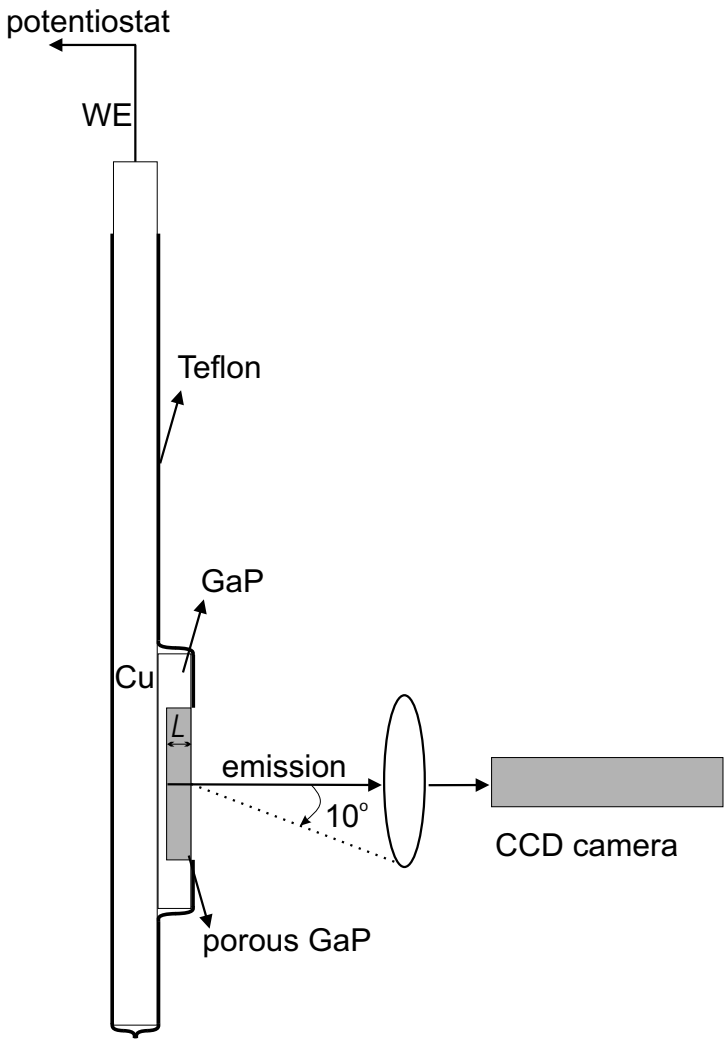

Figure 7.1: *Working electrode (WE) for electrochemical experiments. In the unmasked area of the GaP crystal a porous layer develops (gray coloured). During porous layer growth, luminescence spectra were recorded as a function of the porous layer thickness L.*

blazed at 500 nm). Spectra were recorded as a function of porous layer thickness L (see figure 7.1). At the end of electrochemical etching, the porous layer was selectively removed from the wafer-substrate and an Alpha-Step 500 Surface Profiler was used to measure the thickness of the porous layer and its uniformity. The form of the remaining well, which is directly related to the form of the porous layer, was measured by scanning it with the needle of the profiler. Scanning electron microscopy (SEM, Philips XL30SFEG) pictures were taken to measure the pore radius of the porous materials.

7.3 Results

GaP crystals with a dopant density of 10-20$\times 10^{17}$ cm^{-3} were etched at 6 V. The porosity ϕ, defined as the ratio of the volume of dissolved GaP to the total volume of the porous layer, was 44%. GaP with a dopant density of 7×10^{17} cm^{-3}, etched at 13.5 V, had a porosity of 33%. Previous studies showed that etching starts at defect sites at the surface [3, 4]. The current density increased initially and became constant (see figure 6.3) [4]. The total charge was calculated by integration of the current, and is, in the case of a prous layer with a uniform structure, linearly proportional to the thickness the porous layer L. The uniformity of the structure was confirmed by electron microscopy pictures. Figure 7.2 shows the thickness of the porous layer during the first 10 minutes of etching at 6 V. In the first stage (t $<$ 1 min), pore initiation occurs. When the current becomes constant after $\sim$2 min, the porous layer had a thickness of $\sim$0.5 μm. Subsequently, there is a linear increase of the thickness with time as demonstrated by the straight line in figure 7.2 for t$>$2 min. The etch rate is defined as the slope of the curve in figure 7.2 (for t$>$2 min) and was 0.47 μm/min for the high-doped crystal. For the low-doped crystal an etch rate of 0.62 μm/min was deduced. At the end of the experiment the porous layer had a uniform thickness of $\sim$80 μm. Figure 7.3 shows SEM pictures of the surface of porous layers grown at 6 V (a) and 13.5 V (b). The pore sizes are 51 $\pm$ 11 nm (a) and 103 $\pm$ 21 nm (b) for the high- and low-doped crystals, respectively.

During etching an electroluminescence spectrum was recorded every minute, i.e., every 0.47 μm for the high-doped crystal and 0.62 μm for the

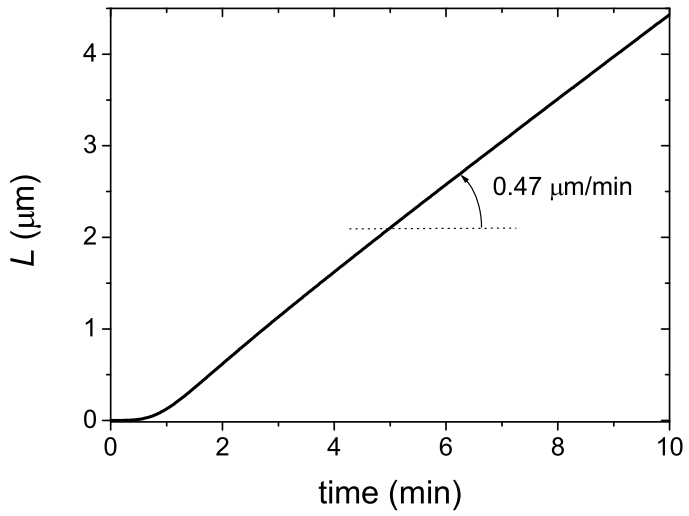

Figure 7.2: *Porous layer thickness (L) as a function of time for n-type GaP (dopant density 10-20×10^{17} cm^{-3}) during the first 10 minutes of etching at 6 V in aqueous 0.5 mol/l H_2SO_4 solution.*

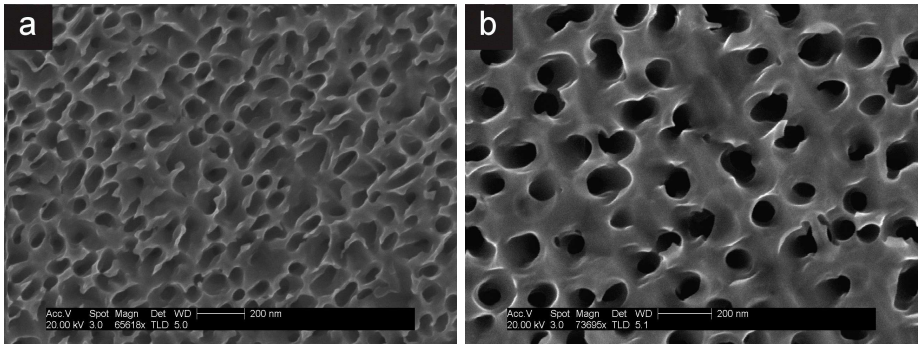

Figure 7.3: *Scanning electron microscopy (SEM) picture of a porous GaP layer etched at (a) 6 V (dopant density 10-20×10^{17} cm^{-3}) and at (b) 13.5 V (dopant density 7×10^{17} cm^{-3}).*

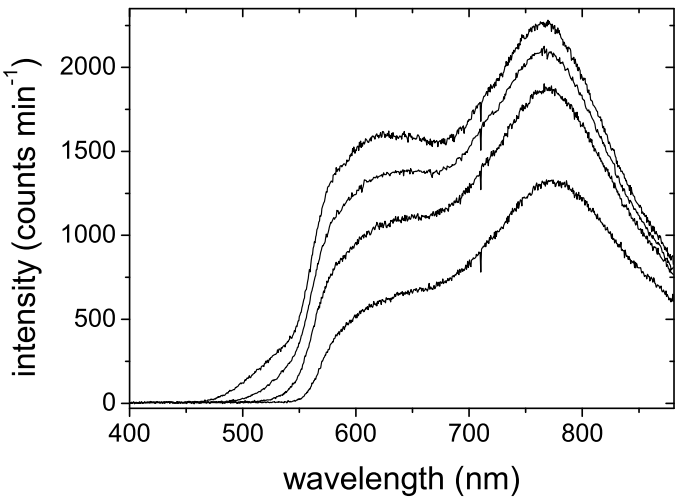

Figure 7.4: *Luminescence spectra of n-type GaP (dopant density 10-20×10^{17} cm^{-3}) etched at 6 V in aqueous 0.5 mol/l H_2SO_4 solution. Spectra were recorded after growing a porous layer of 4 (upper spectrum), 10, 25 and 75 μm (lower spectrum).*

low-doped crystal. Figure 7.4 shows the spectra of the high-doped crystal at a thickness of 4, 10, 25 and 75 μm. Since the electrochemical conditions remain constant during etching it is assumed that changes in the electroluminescence spectra are the result only of changes in the porous layer thickness. It is clear that on going from 4 to 10 μm the intensity of supra-bandgap light is considerably decreased, while for sub-bandgap light the decrease is much smaller. Above 800 nm almost no change in the intensity is observed when the porous layer grows to 10 μm while the intensity at 500 nm is strongly reduced.

A transmission spectrum of the porous layer with a given thickness can be obtained by combining the data of figure 7.2 and figure 7.4; the luminescence intensity at a certain thickness L should be divided by a reference intensity. A proper reference spectrum was recorded at the initial stage of porous etching, before the current density reached its maximum value. At this stage the porous top-layer is very thin and does not influence the spectral distribution of the luminescence; this spectrum can therefore serve as a reference spectrum. Since the current density at this stage was not at its

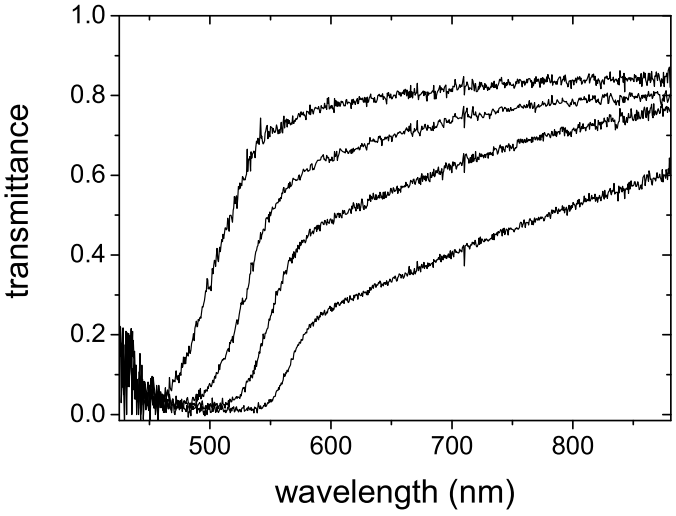

Figure 7.5: *Transmission spectra of n-type GaP (dopant density 10-20×10^{17} cm^{-3}) etched at 6 V in aqueous 0.5 mol/l H_2SO_4 solution. Spectra were recorded after growing a porous layer of 4 (upper spectrum), 10, 25 and 75 μm (lower spectrum).*

maximum, the spectrum should be corrected to apply it as a reference for spectra recorded when the current was maximal. Therefore, this spectrum was multiplied by a constant value and this constant value was calculated by normalising to the long-wavelength side of the spectrum. Values of 1.1 and 1.7 were used for the high- and low-doped crystals, respectively. Transmission spectra for porous layers with a thickness of 4, 10, 25 and 75 μm are shown for the high-doped and low-doped crystal material in figures 7.5 and 7.6, respectively. Below 550 nm the transmission is very low. Above 550 nm the transmission increases with increasing wavelength. Furthermore, it is clear that the transmission above 550 nm is lower for porous layer etched at 13.5 V than the porous layer grown at 6 V. Interestingly, the transmission between 590 nm and 650 nm of a 75 μm layer (figure 7.6) is almost independent on the wavelength.

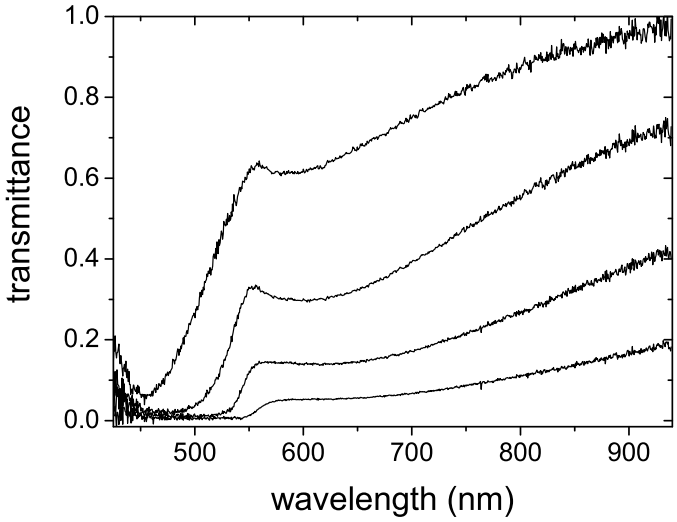

Figure 7.6: *Transmission spectra of n-type GaP (dopant density 7×10^{17} cm^{-3}) etched at 13.5 V in aqueous 0.5 mol/l H_2SO_4 solution. Spectra were recorded after growing a porous layer of 4 (upper spectrum), 10, 25 and 75 μm (lower spectrum).*

7.4 Discussion

Figure 7.1 shows schematically the geometry of our experimental set-up. Light is emitted at the interface between the porous and the non-porous layers [8]. In general two different pathways for transport of light to the detector are possible. Light is emitted in the direction of the detector; it is detected directly or after scattering in the porous layer. Alternatively, light is emitted in the opposite direction and is detected after internal reflection at the backside of the GaP crystal. In this case the path through the (bulk) GaP substrate layer, where no scattering occurs, is at least 440 μm. Light with a wavelength shorter than 545 nm has an absorption length of less than than 40 μm [9] and is thus completely absorbed in the substrate. For $\lambda < 545$ nm the thickness of the substrate is therefore not relevant since at the beginning of etching, when the minimal path length in the substrate layer is 600 μm, and at the end, when the minimal path length is 440 μm, all the light is absorbed in this layer. The substrate layer is completely transparent for light with a wavelength longer than 590 nm. Therefore, in

this case the thickness of the substrate layer is also not relevant. In figure 7.5 and figure 7.6 these wavelength regions can be clearly discriminated. For thick porous layers, the intensity below 545 nm is almost zero. Between 545 nm and 590 nm there is a transition region and above 590 nm the intensity is relatively high.

Clearly, for the two spectral ranges, $\lambda < 545$ nm and $\lambda > 590$ nm, the only relevant parameter that changes during etching is the thickness of the porous layer. Therefore the optical properties of the porous layer (in these spectral regions) can be studied by recording luminescence spectra as a function of porous layer thickness. For $\lambda < 545$ nm both scattering and absorption of light in the porous layer are important. Consequently, a mono-exponential dependence of the transmitted intensity on the thickness of the porous layer L is expected [10]

$$T_d = A \exp \frac{-L}{L_a} \tag{7.1}$$

with

$$L_a = \sqrt{\frac{\ell \cdot \ell_a}{3}} \tag{7.2}$$

where T_d is the diffusive transmission, A the pre-exponential factor, L the thickness of the porous layer, L_a the diffusive absorption length and ℓ_a the absorption length. Here it is assumed that the light source, i.e., the electroluminescence at the interface of the porous and the non-porous layer, is diffuse. Experimental data for the transmittance in the sub-bandgap region justify this assumption (see below). The transport mean free path ℓ, is defined as the length over which the direction of light propagation is randomised.

To deduce the transport mean free path, the absorption length in porous GaP should be known. The absorption length in bulk GaP is well documented (see figure 6.1) [9]. The absorption length in porous GaP can be calculated only when the distance travelled between two scattering events in water is $(\ell \times \phi)$ and in GaP is $\ell \times (1 - \phi)$, where ϕ is the porosity of the porous layer. In our case the typical size of the pores is much smaller than the scattering length. Thus the absorption length in porous GaP can be estimated by dividing the absorption length in bulk GaP by $(1 - \phi)$.

If the absorption length is much smaller than the transport mean free

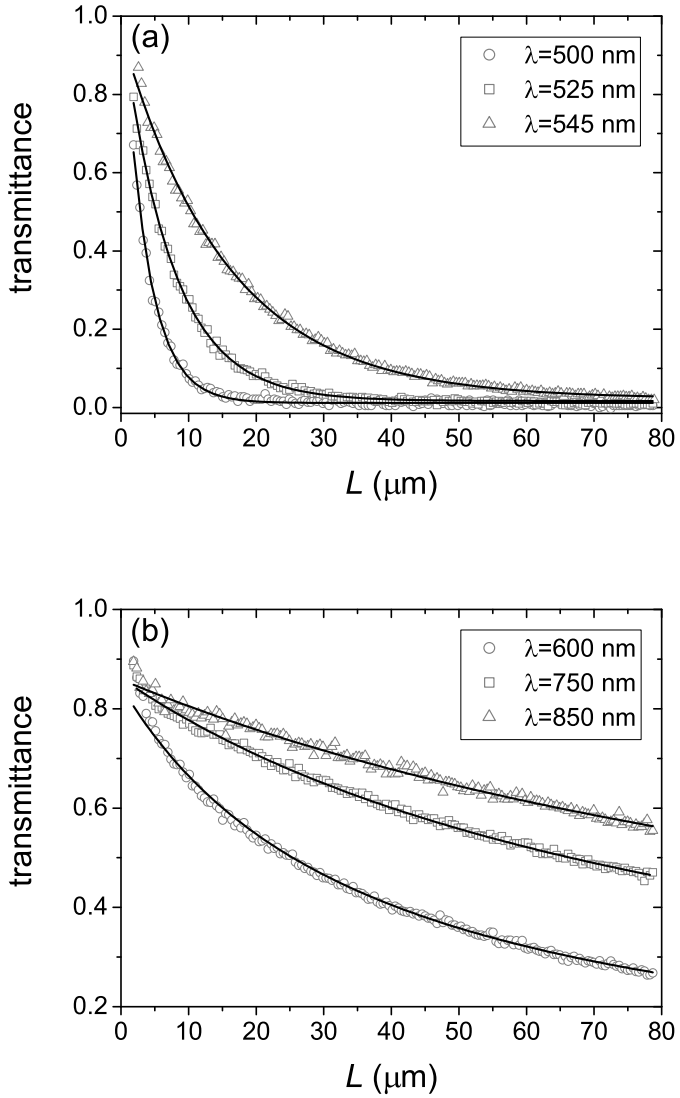

Figure 7.7: *Transmittance as a function of thickness of the porous layer for n-type GaP (dopant density 10-20×10^{17} cm^{-3}) etched at 6 V in aqueous 0.5 mol/l H_2SO_4 solution. The transmission is plotted for supra-bandgap light (a) at wavelengths 500 nm (dots), 525 nm (squares) and 545 nm (triangles) and for sub-bandgap light (b) at wavelengths 600 nm (dots), 750 nm (squares) and 850 nm (triangles). Fits of eqs. 7.1 and 7.3 are also plotted (solid curves).*

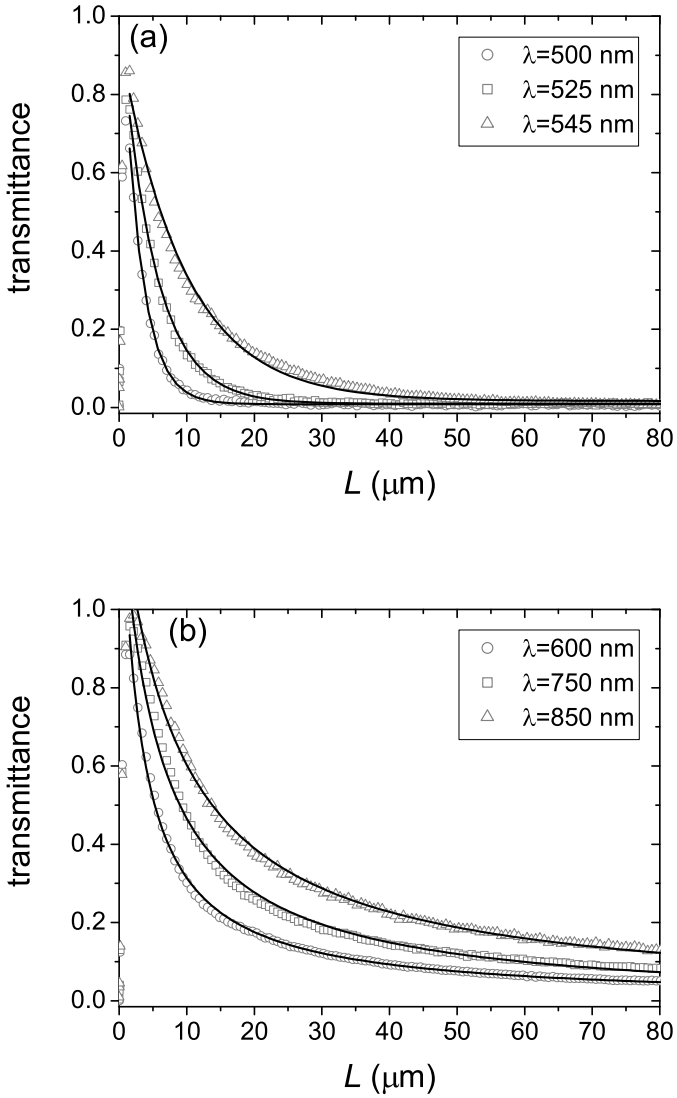

Figure 7.8: *Transmittance as a function of thickness of the porous layer for n-type GaP (dopant density 7×10^{17} cm^{-3}) etched at 13.5 V in aqueous 0.5 mol/l H_2SO_4 solution. The transmission is plotted for supra-bandgap light (a) at wavelengths 500 nm (dots), 525 nm (squares) and 545 nm (triangles) and for sub-bandgap light (b) at wavelengths 600 nm (dots), 750 nm (squares) and 850 nm (triangles). Fits of eqs. 7.1 and 7.3 are also plotted (solid curves).*

path ($\lambda > 590$ nm), the diffuse transmission is given by [11–13]

$$T_d = \frac{1 + z_{e1}}{(L/\ell) + 2z_{e2}} \tag{7.3}$$

where z_{e1} and z_{e2} account for the reflectivity of the porous GaP|electrolyte and porous GaP|bulk GaP interfaces.

Figures 7.7 and 7.8 show the transmission versus thickness of the porous layer at various wavelengths. Fits of eqs. 7.1 and 7.3, with the pre-exponential factor A, ℓ and z_e as adjustable parameters, are also plotted (solid curves). Clearly, modelling our experimental data with eqs. 7.1 and 7.3 reveals an excellent agreement and thus the intensity of supra-bandgap light decreases mono-exponentially with thickness and the intensity of sub-bandgap light decreases with reciprocal thickness. From the agreement between experiment and theory, three can be concluded. First, it can be concluded that luminescence is generated at the interface of the porous and the non-porous layer, and that the porous layer has a uniform structure. Second, it is clear that light in the sub-bandgap region is scattered in the porous layer without being absorbed. Third, the transmittance decreases with the inverse of the thickness in the sub-bandgap region, even in the thickness range similar to or smaller than the transport mean free path, i.e., $\ell/L \geq 1$. The agreement in the small thickness-range confirms that the light source is diffusive and not coherent. In the case of a coherent light source, the coherent transmission decreases mono-exponentially with thickness [14]. It should be noted that, on occasion, a deviation from the decrease as described by eqs. 7.1 and 7.3 was observed under constant current conditions; this is attributed to a non-uniform structure of the porous layer.

The transport mean free path for supra-bandgap light can now be determined from the fit parameters of eq. 7.1. In order to deduce the transport mean free path in the sub-bandgap region, z_{e1} should be known. However, as will be shown below, this parameter can be neglected and therefore in this case the slope of $1/T_d$ versus L is equal to $1/\ell$. In figure 7.9 the transport mean free is plotted for two porous layers grown under different conditions. Supra-bandgap and sub-bandgap data are plotted. A good agreement, i.e., a clear connection, between these two spectral regions can be observed.

In the sub-bandgap region scattering is weaker than in the supra-band-

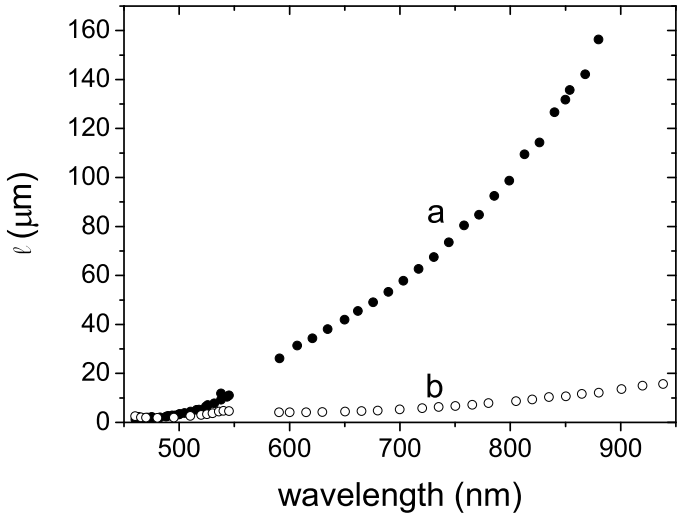

Figure 7.9: *Transport mean free path (ℓ) as a function of wavelength for GaP etched at 6 V (a) and GaP etched at 13.5 V (b).*

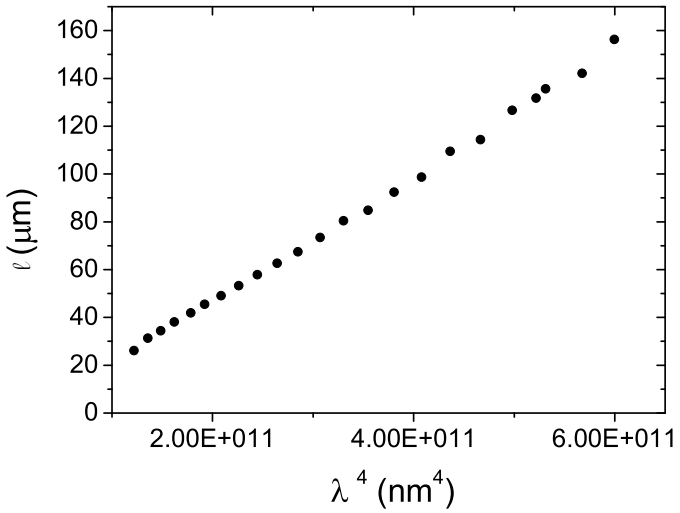

Figure 7.10: *Transport mean free path (ℓ) as a function of λ^4 for Gap etched at 6 V. Note that only data from the sub-bandgap region is plotted.*

gap region. A larger refractive index [9] and a larger size-parameter [15] cause this difference; the scattering cross-section increases with refractive index contrast. Furthermore, for smaller wavelength the size-parameter is larger and therefore light is scattered more strongly. The porous layer grown at 13.5 V has larger pores and therefore scatters light more strongly (figure 7.3). Furthermore, it is clear that the size of the pores grown at 6 V is considerably smaller than the wavelength of the emitted light. This is the regime of Rayleigh scattering in which the transport mean free path is proportional to λ^4 [15], as shown in figure 7.10. The λ^4-dependence is clearly observed which confirms that the influence z_{e1} (eq. 7.3) is indeed small and that the method applied to deduce ℓ is correct. During the measurements the pores contained water. The results shown in figure 7.9 cannot be explained by the wavelength dependence of the refractive index of water, which shows a change of less than 1 % on going from 450 nm to 900 nm [16]. Enhanced backscattering (EBS) measurements on these samples, which were preformed in air, showed that the transport mean free paths are in the micron regime and that sample etched at 13.5 V scatters light more strongly than sample etched at 6 V. This is in agreement with results obtained here. That the values found with EBS are in agreement with those found here, is further confirmation that the influence z_{e1} must be slight.

7.5 Conclusion

Two GaP crystals with a different dopant density were etched, to give porous layers with two different pore sizes. Electroluminescence spectra, recorded during etching, were used as a tool to characterise the porous layers. Transmission spectra were deduced for porous layers in a wide thickness range. From the transmittance the transport mean free path over a wide spectral range, from the ultra-violet to the near-infrared, could be determined. Instead of measuring the transmittance as function of thickness is many separate experiments with several porous layers, we were able to measure the transmittance for many thicknesses in a single experiment. With this approach we showed that the electroluminescence can readily be used for an *in-situ* optical characterisation of growing porous GaP layers.

References

[1] S. Langa, I. M. Tiginyanu, J. Carstensen, M. Christophersen, and H. Foll, *Formation of porous layers with different morphologies during anodic etching of n-InP*, Electrochemical and Solid State Letters **3**, 514 (2000).

[2] G. Oskam, A. Natarajan, P. C. Searson, and F. M. Ross, *The formation of porous GaAs in HF solutions*, Applied Surface Science **119**, 160 (1997).

[3] B. H. Erné, D. Vanmaekelbergh, and J. J. Kelly, *Morphology and strongly enhanced photoresponse of GaP electrodes made porous by anodic etching*, Journal of the Electrochemical Society **143**, 305 (1996).

[4] R. W. Tjerkstra, J. Gómez Rivas, D. Vanmaekelbergh, and J. J. Kelly, *Porous GaP multilayers formed by electrochemical etching*, Electrochemical and Solid State Letters **5**, G32 (2002).

[5] J. Gómez Rivas, A. Lagendijk, R. W. Tjerkstra, D. Vanmaekelbergh, and J. J. Kelly, *Tunable photonic strength in porous GaP*, Applied Physics Letters **80**, 4498 (2002).

[6] F. J. P. Schuurmans, D. Vanmaekelbergh, J. van de Lagemaat, and A. Lagendijk, *Strongly photonic macroporous gallium phosphide networks*, Science **284**, 141 (1999).

[7] M. I. J. Beale, J. D. Benjamin, M. J. Uren, N. G. Chew, and A. G. Cullis, *An experimental and theoretical study of the formation and microstructure of porous silicon*, J. Cryst. Growth **73**, 622 (1985).

[8] A. F. van Driel, B. P. J. Bret, D. Vanmaekelbergh, and J. J. Kelly, *Hot carrier luminescence during porous etching of GaP under high electric field conditions*, Surface Science **529**, 197 (2003).

[9] D. E. Aspnes and A. A. Studna, *Dielectric functions and optical parameters of silicon, germanium, gallium phosphide, gallium arsenide, gallium antimonide, indium phosphide, indium arsenide, and indium antimonide from 1.5 to 6.0 eV*, Physical Review B **27**, 985 (1983).

[10] J. Gómez Rivas, R. Sprik, C. M. Soukoulis, K. Busch, and A. Lagendijk, *Optical transmission through strong scattering and highly polydisperse media*, Europhysics Letters **48**, 22 (1999).

[11] D. J. Durian, *Influence of boundary reflection and refraction on diffusive photon transport*, Physical Review E **50**, 857 (1994).

[12] J. H. Li, A. A. Lisyansky, T. D. Cheung, D. Livdan, and A. Z. Genack, *Transmission and surface intensity profiles in random-media*, Europhysics Letters **22**, 675 (1993).

[13] A. Z. Genack, *Optical transmission in disordered media*, Physical Review Letters **58**, 2043 (1987).

[14] J. Gómez Rivas, *Light in Strongly Scattering Semiconductors* (Ph.D. thesis, University of Amsterdam, Amsterdam, 2002).

[15] H. C. van de Hulst, *Light Scattering by Small Particles* (Dover Publications Inc, New York, 1981).

[16] P. Schiebener, J. Straub, J. M. H. L. Sengers, and J. S. Gallagher, *Refractive-index of water and steam as function of wavelength, temperature and density*, Journal of Physical and Chemical Reference Data **19**, 677 (1990).

Samenvatting in het Nederlands

Licht speelt een essentiële rol voor allerlei toepassingen die we dagelijks gebruiken zoals tl-buizen, televisie schermen, lasers, zonnecellen en lichtgevende diodes. Controle over het uitzenden van licht is daarom erg belangrijk en zal de efficientië van bovengenoemde toepassingen verhogen. Wanneer bijvoorbeeld het licht van de zon op een efficiëntere manier 'gevangen' kan worden, zal het rendement van zonnecellen toenemen. Daarnaast is het maken van materialen die het transport en het uitzenden van licht kunnen beheersen een grote wetenschappelijke uitdaging.

Het hart van de toepassingen waarin licht een essentiële rol speelt zijn de zogenaamde lichtbronnen. Als lichtbronnen worden halfgeleiders, organische kleurstoffen, overgangs-metaal ionen en zeldzame-aard ionen gebruikt. De lichtbronnen kunnen worden aangeslagen, dit betekent dat ze in een hogere energietoestand zijn, en kunnen weer terugvallen naar de grondtoestand. Het terugvallen naar de grondtoestand gaat gepaard met het uitzenden van licht. In tl-buizen bijvoorbeeld worden drie verschillende zeldzame-aard ionen gebruikt die groen, blauw en rood licht uitzenden. Deze drie kleuren geven samen wit licht. Nanokristallijne halfgeleider deeltjes zijn kristallijne deeltjes van ongeveer een nanometer[1] groot en worden ook 'kwantum dots' genoemd. Deze nanodeeltjes zijn een unieke en relatief nieuwe klasse van lichtbronnen. Veel van de experimenten beschreven in dit proefschrift zijn gedaan met nanokristallijne halfgeleider deeltjes. Deze nanodeeltjes hebben unieke eigenschappen ten opzichte van andere lichtbronnen. De meest in het oog springende van deze unieke eigenschap-

[1] 1 nm is een miljardste van een meter, 1×10^{-9} m

pen is de kleur licht die de nanodeeltjes uitzenden; de kleur wordt bepaald door de grootte van de deeltjes. Bijvoorbeeld, bolvormige nanodeeltjes van de halfgeleider cadmium selenide (CdSe) van ongeveer 3 nm groot zenden, nadat ze zijn aangslagen, blauw licht uit terwijl grotere deeltjes (6 nm) van hetzelfde materiaal rood licht uitzenden. Met chemische synthese technieken kunnen suspensies, dit zijn vloeistoffen waarin de nanodeeltjes vrij rondzweven, gemaakt worden. Onze nanodeetjes zenden licht uit met een hoog kwantum rendement. Dit betekent dat een groot percentage van het licht dat geabsorbeerd wordt tijdens het aanslaan van de deeltjes ook weer uitgezonden wordt. Naast het hoge kwantum rendement hebben nanodeeltjes andere eigenschappen die ze zeer geschikt maken als lichtbronnen in optische studies zoals in dit proefschrift beschreven worden. Eén van die eigenschappen is het uitzenden van licht in een smal frequentiebereik. In wetenschappelijk taalgebruik wordt dan gezegd dat de deeltjes een smalle homogene lijnbreedte hebben. Verder is het lichtgevende deel van de nanodeeltjes goed beschermd van de buitenwereld, waardoor ze weinig chemische interactie vertonen met de omgeving en extra stabiel zijn. De stabiliteit maakt het makkelijker de fysische effecten waar we naar op zoek zijn waar te nemen.

Materialen die het uitzenden en het transport van licht kunnen beheersen worden 'fotonische materialen' genoemd. In dergelijke materialen varieert de brekingsindex op een lengteschaal vergelijkbaar met de golflengte van licht, oftewel op een lengteschaal van ongeveer 500 nm. Materialen met een hoge brekingsindex hebben een sterke interactie met licht. Fotonische materialen zijn opgebouwd uit een materiaal met een hoge brekingsindex en een materiaal met een lage brekingsindex. Door deze combinatie van materialen kunnen fotonische materialen het licht even vangen of vast houden. Materialen die het licht kunnen vangen zijn er nog niet. Er zijn al wel materialen waarvan verondersteld wordt dat ze het licht even kunnen vasthouden, maar dit effect in nog nooit experimenteel aangetoond. Licht en geluk lijken in dit opzicht op elkaar; je kunt het soms even vasthouden maar als je denkt dat je het beet hebt ben je het al weer kwijt. In dit proefschrift worden experimenten met twee typen fotonische materialen beschreven: kristallen van titania (TiO_2) en poreus gallium fosfide (GaP). De kristallen van titania die we gebruikt hebben

worden fotonische kristallen genoemd. Ze zijn opgebouwd uit regelmatig geordende luchtbollen in een matrix van titania. De luchtbollen hebben een diameter van ongeveer 300 nm. In 1987 is het theoretische voorspeld dat fotonische kristallen de snelheid van het uitzenden van licht kunnen beïnvloeden. Echter, dit is nog nooit experimenteel aangetoond. Om dit vast te stellen hebben wij lichtgevende CdSe nanodeeltjes in fotonische kristallen van titania gebracht en gekeken of het uitzenden van licht door de nanokristallen beïnvloed wordt door de fotonische omgeving. Maar alvorens dit te kunnen bestuderen waren er een aantal noodzakelijke stappen die eerst genomen moesten worden.

Eerst moeten de nanodeeltjes gesynthetiseerd worden. In hoofdstuk 2 is uitgebreid beschreven hoe cadmium telluride (CdTe) en CdSe nanodeeltjes, die zichtbaar licht uitzenden met een hoog rendement, kunnen worden gemaakt. Vervolgens is bekeken hoe de nanokristallen licht geven als ze vrij in de oplossing zijn. De snelheid van het uitzenden is gemeten voor de verschillende kleuren licht die de nanokristallen kunnen uitzenden. Dit is beschreven in hoofdstuk 4. De snelheids metingen worden 'luminiscentie-vervals-metingen' genoemd en de meetresultaten 'vervalskurven'. Uit deze vervals-kurven kan de vervalssnelheid -de snelheid van het uitzenden van licht- bepaald worden. Hoe de snelheid uit de experimentele vervalskurven bepaald kan worden is beschreven in hoofdstuk 3. Er is een wiskundige analyse van de vervals-kurven gemaakt. Deze analyse maakte het voor ons mogelijk handzame informatie uit complexe kurven te halen. Zo konden we aantonen dat alle deeltjes die het licht van een bepaalde kleur uitzenden dat allemaal met ongeveer dezelfde snelheid doen. De nanodeetjes die blauw licht uitzenden doen dat met een snelheid van 60 miljoen keer per seconde, oftewel gemiddeld één keer per 17 nanoseconden, en de deeltjes die rood licht uitzenden doen dat drie keer langzamer. De gemeten snelheid bleek in overeenstemming te zijn met de snelheid bepaald op basis van kwantummechanische berekeningen.

Na deze metingen hebben we nanodeeltjes van hetzelfde halfgeleidermateriaal (CdSe) in de fotonische kristallen gebracht. Vervolgens hebben we wederom bepaald hoe snel de verscillende kleuren worden uitgezonden en of deze snelheid bepaald wordt door de fotonische omgeving. De resultaten laten zien dat dit inderdaad het geval is. Afhankelijk van de

grootte van de repeterende eenheid van de fotonische kristallen, oftewel de grootte van de luchtbollen, bleek de snelheid met een factor drie te variëren. Hiermee waren wij de eerste onderzoekers die dit effect experimenteel konden aantonen.

In de laatste twee hoofdtukken van dit proefschrift (hoofdstukken 6 en 7) worden experimenten met poreus GaP beschreven. Poreus GaP is een interessant materiaal omdat GaP een uitzonderlijk hoge brekingsindex heeft. De variaties in de brekingsindex in poreus GaP zijn daardoor groot. Door de sterke variatie heeft poreus GaP een enorm sterke interactie met licht.

GaP kan poreus gemaakt worden door middel van 'elektrochemische etsen'. Tijdens elektrochemisch etsen wordt een hoge spanning op een GaP kristal aangelegd met een batterij. Door de hoge spanning groeien er op een wanordelijke manier porieën in het GaP en wordt het poreus. De diameter van de porieën is ongeveer 100 nm. Deze methode wordt al lang gebruikt en dient in een donkere kast uitgevoerd te worden. Wat wij echter voor het eerst waargenomen hebben is dat gedurende het etsen licht uitgezonden wordt. Op de plaats waar het etsen plaatsvindt, in het uiteinde van de groeiende porieën, wordt zichtbaar licht gegenereerd. Het mechanisme dat verantwoordelijk is voor het uitzenden van licht hebben we kunnen achterhalen en is in hoofdstuk 6 beschreven. Gedurende poreus etsen groeien de porieën met ongeveer 0.5 micrometer (μm)[2] per minuut. We hebben de intensiteit van het licht dat uitgezonden wordt om de minuut gemeten. Deze intensiteit neemt geleidelijk af doordat de porieën elke minuut steeds dieper worden. Door de intensiteit als functie van de diepte van de porieën te meten, konden de fotonische eigenschappen van de groeiende poreuze GaP structuur bepalen.

[2] 1 μm is een miljoenste van een meter, 1×10^{-6} m

List of publications

The results presented in this thesis have been reported in the following publications:

- Chapter 2
  S. F. Wuister, F. van Driel and A. Meijerink, *Luminescence and growth of CdTe quantum dots and clusters*, Physical Chemisty Chemical Physics, **5**, 1253 (2003).

  S. F. Wuister, I. Swart, F. van Driel, S. G. Hickey, and C. de Mello Donegá, *Highly luminescent water-soluble CdTe quantum dots*, Nano Letters, **3**, 503 (2003).

- Chapter 3
  A. F. van Driel, I. S. Nikolaev, P. Vergeer, P. Lodahl, D. Vanmaekelbergh and W. L. Vos, *Statistical analysis and modelling of time-resolved emission from semiconductor quantum dots: interpretation of exponential decays*, in preparation for Physical Review B.

- Chapter 4
  A. F. van Driel, G. Allan, C. Delerue, P. Lodahl, W. L. Vos and D. Vanmaekelbergh, *Frequency-dependent spontaneous emission rate from CdSe and CdTe nanocrystals: Influence of dark states*, Physical Review Letters, **95**, 236804 (2005).

- Chapter 5
  P. Lodahl, A. F. van Driel, I. S. Nikolaev, A. Irman, K. Overgaag, D. Vanmaekelbergh and W. L. Vos, *Controlling the dynamics of spontaneous emission from quantum dots by photonic crystals*, Nature, **430**, 654 (2004).

- Chapter 6
  A. F. van Driel, B. P. J. Bret, D. Vanmaekelbergh and J. J. Kelly, *Hot carrier luminescence during porous etching of GaP under high electric field conditions*, Surface Science, **529**, 197 (2003).

- Chapter 7
  A. F. van Driel, D. Vanmaekelbergh and J. J. Kelly, *Electroluminescence as internal light source for measurement of the photonic strength of random porous GaP*, Applied Physics Letters, **84**, 3852 (2004).

Other publications:

- F. van Driel, F. Decker, F. Simone and A. Pennisi, *Charge and colour diffusivity from PITT in electrochromic Li_xWO_3 sputtered films*, Journal of Electroanalytical Chemistry, **537**, 125 (2002).

- L. K. van Vugt, A. F. van Driel, R. W. Tjerkstra, L. Bechger, W. L. Vos, D. Vanmaekelbergh and J. J. Kelly, *Macroporous germanium by electrochemical deposition*, Chemical Communications, **18**, 2054 (2002).

- J. J. Kelly and A. F. van Driel, *The electrochemistry of porous semiconductors*, Chapter 3 in *Electrochemistry at the Nanoscale*, Kluwer series: Nanostructure Science and Technology, to be published

- A. F. van Driel, D. Vanmaekelbergh and J. J. Kelly, *Random lasing of Rhodamine dye in photonic macroporous GaP*, submitted to Applied Physics Letters.

Dankwoord

Zoals vele proefschriften is dit proefschrift het product van langdurige en intensieve samenwerking. Graag wil ik op deze plaats de mensen danken die een bijdrage aan de samenwerking en dit proefschrift geleverd hebben.

Allereerst wil ik op deze plaats mijn drie promoteren danken. Ik heb de afgelopen jaren intensief samengewerkt met drie hoogleraren: Daniël Vanmaekelbergh, John Kelly en Willem Vos. Ik beschouw het als een eer jullie als mijn promotoren te hebben. Ik wil jullie alle drie bedanken voor de inzet en inspiratie om wetenschappelijke en niet-wetenschappelijke zaken te benaderen. Altijd waren jullie geinteresseerd in mijn werkzaamheden, wat ik als een luxe beschouw. Jullie hanteren alledrie een andere aanpak in het bedrijvan van wetenschap, wat het soms lastig maakte jullie gedrieen tevreden te stellen. Ondanks of mischien dankzij die verschillende benaderingen heb ik van jullie alledrie veel geleerd!

Het samenwerken met collega's in gezamelijke experimenten begon met Sander Wuister. Sander, ik heb het als fijn ervaren samen met jou onze eerste goed lumiscerende dotjes te maken. Soms escaleerde het volledig uit de hand, maar we hebben toch mooie dingen gemaakt! Daarna heb ik samengewerkt met Boris Bret. Eigenlijk hebben onze gezamelijke experimenten maar twee dagen geduurd. Uiteindelijk zijn er voor mij toch twee hoofdstukken uit voort gekomen. Dat noem ik nog eens een efficiente samenwerking! Vervolgens ben ik met een langdurige en intensieve samenwerking begonnen met de cops van COPS (Complex Photonic Systems, Universiteit Twente). Het was een hele bijzondere ervaring met de COPS samen te werken. Ik vond het niet altijd gemakkelijk in meerdere groepen tegelijkertijd te functioneren, vooral als die groep zo verschillend zijn.

Maar uiteindelijk hebben we onze gezamelijke doelen toch gerealiseerd! Bij COPS heb ik direct samengewerkt met Arie Irman, Peter Lodhal, Lydia Bechger, Léon Woldering, Karin Overgaag en Ivan Nikolaev. Wat mij betreft was het een vruchtbare en leerzame samenwerking. Dank daarvoor! Gedurende de afgelopen jaren heb ik Bachelor- en Master-studentes begeleid: Ming Yuan, Lia Verhoeff en Linda Aarts. Ik wil jullie op deze plaats danken voor jullie inzet en bijdrage. Graag wil ik nog speciaal Peter Liljeroth, Wouter Wassing en Mark Kooijman danken. Het schrijven van een proefschrift zou een stuk lastiger geweest zijn als er geen LaTeX en geen mensen in de buurt waren die schijnbaar elke vraag met betrekking tot LaTeX kunnen beantwoorden. Verder wil ik mijn paranimfen Didi Derks en Arjan Houtepen bedanken.

I would like to thank Guy Allan and Christophe Delerue (IEMN, Département ISEN, Lille, France) for preforming the tight-binding calculations, and developing a simple and elegant theory, as presented in Chapter 4. This collaboration increased my insight in nanocrystal-physics a lot. Thank you this and thanks for the nice collaboration!

Een derde groep mensen die, naast begleiders en directe collega's, wat meer op de achtergrond aan dit proefschrift heeft bijgedragen is het zogenaamde ondersteunend personeel. In de groep CMI (Condensed Matter and Interfaces, Universiteit Utrecht) zijn dit Hans Ligthart, Jessica Heilbrunn en Stephan Zevenhuizen. De ondersteuning, in meerdere opzichten, had ik niet kunnen missen. Stephan, dank voor de SEM-foto's en de hulp met mijn computer. Hans en Jessica, dank voor jullie cappucino's en thee, en voor het luisterende oor.

Naast de 'officiele' samenwerkingsverbanden was er ook nog een samenwerking die zo'n beetje overal doorheen liep maar nergens met zoveel woorden genoemd wordt, namelijk de samenwerking met mijn collega en kamergenoot Peter Vergeer. Als er een (wetenschappelijk) probleem was begon dit vaak van mijn kant met de woorden 'he Vergeer'. Jij was bijna altijd geinteresseerd en ook bijna altijd kwamen we er wel uit. Dank daarvoor! Als ik m'n wetenschappelijke rederneringen aan jouw kon verkopen dan was het meestal ook wel in orde. Daarnaast waren onze fietstochten en uitstapjes naar De Vooghel natuurlijk onmisbaar.

Ook wil ik op deze plaats mijn directe collega's noemen. Paul, Mar-

cel, Freek Aarnoud, Celso, Steve, Jan, Sven, Alexander, Francois, Stephen, Zeger, Harold, Bert, Andries, Cees, Jan, Thijs, Rene, Arjan, Aneliya, Rianne, Shuai, Rolf, Dennis, Karin, Peter: dank voor de fijne sfeer de afgelopen jaren! Voor de nodige ontspanning buiten de wetenschap wil ik mijn familie en vrienden danken. Het fietsen, vogelskijken, de yoga uurtjes, film avondjes en etentjes, en de hardloop en badminton activiteiten waren onmisbaar!

Dan is het nu bijna af, na jaren hard werken binnen en, soms nog veel intensiever, buiten de wetenschap. Als ik terug denk aan het moment waarop ik het promotieonderzoek begon merk ik pas hoeveel er veranderd is de afgelopen jaren. De belangrijkste dingen die ik de afgelopen jaren geleerd heb staan niet in dit proefschrift en zijn me veel waard. De vraag is dan nu hoe dit proefschrift op een fatsoenlijke manier af te ronden. Dit proefschrift is begonnen met de wijze woorden van iemand anders. Ook wil ik met een citaat eindigen:

”The Dude abides. I don’t know about you but I take comfort in that. It’s good knowin’ he’s out there. The Dude. Takin’ ’er easy for all us sinners.”

Curriculum vitae

The author of this thesis was born on Februari 28th in Werkendam, The Netherlands. In May 1996 he obtained his VWO diploma at the 'Christelijke Scholengemeenschap "Oude Hoven"' in Gorinchem. Subsequently, he started in September 1996 his study in chemistry at Utrecht University. He received his propaedeutic diploma (*cum laude*) in August 1997 and his Master of Science (MSc) degree in August 2001 (*cum laude*). His MSc-project was performed at the Condensed Matter group under supervision of dr. E. P. A. M. Bakkers and Prof. dr. D. Vanmaekelbergh at Utrecht Universiy. In 2001 he conducted a six-months Erasmus project at the 'Univesitá degli studi di Roma "La Sapienza"'. The Erasmus project was performed under supervision of Prof. dr. F. Decker and results of the project were presented at the 15th conference on Electrochemical Impedance Spectroscoy (EIS2001, Marilleva, Italy).

From Oktober 1st 2001 he was employed as PhD-student in the group Condensed Matter and Interfaces at Utrecht Univesity, under supervision of Prof. dr. J. J. Kelly and Prof. dr. D. Vanmaekelbergh. The project was supported by Chemische Wetenschappen (CW) with financial aid from the Nederlandse Organisatie voor Wetenschappelijk Onderzoek (NWO). A large part of the project was performed in collaboration with Prof. dr. W. L. Vos from the University of Twente. The results of his PhD-project are described in this thesis and published in scientific journals. Oral presentations of the results were given at the 203rd conference of the Electrochemical Society (ECS2003, Paris France), the 9th conference on Optics of Excitons on Confined Systems (OECS2005, Southampton, Great Britain) and the 5th conference on Porous Semiconductors-Science and Technology (PSST2006, Sitges, Spain).

Besides his research activities, he supervised Bachelor and Master students, assisted an analytical chemistry course of first year students, 'keuze praticum' for second year students, and high school students with their 'profiel werkstuk'.